Universidad Autónoma de Madrid
Facultad de Ciencias
Departamento de Física Aplicada

Theory, characterization and optomechanical effects of ultrathin nanomechanical resonators

Memoria de tesis para optar al grado de Doctor en Físicas presentada por:

Valerio Pini

Dirigida por los doctores:

Francisco Javier Tamayo de Miguel y

Montserrat Calleja Gómez,

Y bajo la tutela del doctor:

Miguel Manso Silvan

CSIC
Consejo Superior de Investigaciones Científicas
IMM
Instituto de Microelectrónica de Madrid
(Centro Nacional de Microelectrónica)

UAM
Universidad Autonoma de Madrid

To my daughter Sofia,

To my wife Gianna,

To my family

Agradecimientos

Ante todo quiero agradecer en especial a mis directores de tesis Javi y Montse, que han sido fundamentales para conseguir este trabajo doctoral. Sus enseñanzas, sus grandes competencias profesionales y calidades humanas me han transmitido pasión y me han guiado en el difícil trabajo de la investigación. La oportunidad de trabajar a su lado ha sido una ocasión única para mi crecimiento tanto a nivel personal como profesional.

Quiero expresar toda mi gratitud también a mis compañeros de laboratorio para su fundamental apoyo técnico y moral en muchos momentos de mi tesis. Entre todos hemos creado un entrañable ambiente de trabajo, condición ideal para sacar el máximo provecho creativo de cada uno de nosotros. Un sincero agradecimiento a Pris, constante punto de referencia y siempre disponible en cualquier circunstancia. Su apoyo incondicional ha sido decisivo en muchas ocasiones. Un agradecimiento especial también a Jose, compañero fiel de infinitas batallas. Juntos hemos aprendido mucho y sin duda muchos retos no habrían sido posibles sin tu ayuda. Gracias a Edu para su fundamental apoyo en mis primeros años de tesis, a Dani por sus buenos consejos, a Oscar por sus resolutivas soluciones en cualquier momento, a Mario por su apoyo y disponibilidad y, también gracias a Carmen, Alicia, Álvaro, Charis, Johann, Diana, Guillermo, Iker, Mercedes, Sheila, Rubens y Roseli.

Debo un especial reconocimiento también a todos los compañeros de Mecwins: el estimulante intercambio de conocimientos y su continuo apoyo técnico ha sido muy importante para el logro de muchos importantes resultados.

Quiero agradecer también a los colaboradores en la fabricación de dispositivos: Alberto y Zachary por la fabricación de las membranas y Cees y Hien por la fabricación de las palancas.Tambíen me complace agradecer a mi tutor de tesis Miguel, siempre disponible ante cualquier duda.

Infinitamente gracias también a todos los amigos que me han acompañados en estos años: David, Gabriele, Enrique, Renato, verdaderos amigos siempre dispuestos a echarme una mano en cualquier ocasión, a escucharme y hacerme reír cuando más hacía falta.

Mi profunda gratitud a mi familia y a mis padres, referencias y guías constante en mi vida. Estoy profundamente agradecido por todos los valores que me han transmitido, por su cercanía frente a cualquier dificultad, por su confianza en mis capacidades y por haber siempre aceptado mis decisiones. Gracias Babbo, eres el ejemplo que quiero seguir siempre. Tu cercanía, confianza y apoyo me han dado siempre mucha fuerza. Gracias Mamma. Aunque ya no estas con nosotros, siento siempre tu presencia. Siempre has confiado en mis capacidades, y como una verdadera luchadora cual eras, me has enseñado siempre a perseverar incasablemente por mis metas y por mis sueños. Estoy convencido de que estarías muy orgullosa de todo eso.

Todo esto nunca hubiera sido posible sin el apoyo de Gianna, autentica columna portante de mi vida. Has estado siempre a mi lado en cualquier circunstancia, has sabido siempre darme sabios consejos en los momentos más tensos, has soportado y aceptado todos mis esfuerzos y muchas veces te has hecho cargo, tú sola, de las necesidades de Sofi, puro concentrado de energía y alegría. Gracias, gracias, gracias. Estoy orgulloso de tener a lado una persona como tú.

Contents

Resumen

Las nano-estructuras mecánicas que oscilan a altas frecuencias representan la base de una multitud de fascinantes aplicaciones en nanotecnología como el procesado de señales[1-8], sensores químicos[9-12] y biológicos[13-21], y la observación de efectos cuánticos en sistemas mecánicos[22-25]. Estos dispositivos, conocidos en la literatura como resonadores nanomecánicos pueden tener forma de palancas[26-28], puentes[4-7] y membranas[29-32] o incluso pueden tener canales integrados para micro y nano-fluidica[14,33-35].

El metódo más utilizado para mejorar el rendimiento de un resonador nanomecánico consiste en la miniaturización del dispositivo. La pequeña masa y las altas frecuencias de resonancia de estos dispositivos permiten alcanzar una sensibilidad en masa sin precedentes llegando hasta el yocto-gramo[36,37]. Sin embargo, esta drástica miniaturización no es posible en una gran variedad de aplicaciones sensoras basadas en resonadores nanomecánicos, ya que, en muchos casos la sensibilidad no es la única cantidad que hay que maximizar. En aplicaciones que requieren medir pequeñas cantidades de analito ultra-diluido[27,38,39], hay que tener en cuenta también otro límite de detección determinado por el límite difusivo que escala con el área del sensor[8]. Por lo tanto, en muchas aplicaciones el dispositivo ideal necesita tener una alta sensibilidad y, al mismo tiempo una gran área de captura; esta necesidad explica por qué hay tanto interés en el desarrollo de estructuras mecánicas ultra-delgadas[29,40-44]. Los resonadores nanomecánicos ultra-delgados representan el mejor compromiso para medir concentraciones ultra-bajas de analito con alta sensibilidad. Aunque estos dispositivos poseen un enorme potencial para el desarrollo de futuros sensores[45], hay varias cuestiones abiertas que hay que resolver. En esta tesis voy a profundizar en algunos aspectos relevantes que surgen a la hora de utilizar los resonadores nanomecánicos ultra-delgados.

La primera cuestión importante a la hora de utilizar resonadores ultra-delgados es la necesidad de caracterizar el espesor con una buena precisión[46-49]. A pesar de los grandes avances de la litografía en la fabricación de micro y nano-estructuras, el espesor sigue siendo un parámetro muy difícil de controlar durante el proceso de fabricación[46]. Como las propiedades mecánicas de un resonador mecánico dependen en gran medida de su espesor[50], en el caso de estructuras ultra-delgadas la incertidumbre en el espesor constituye el factor más importante en la variabilidad mecánica de estos dispositivos. La caracterización experimental del espesor de dispositivos nanomecánicos con precisión nanométrica es una tarea muy compleja, ya que además de una buena precisión en la medida del espesor, es necesario cumplir al mismo tiempos los siguientes requisitos: *i*) lograr una resolución lateral micrométrica capaz de detectar cada resonador nanomecánico, *ii*) detección de áreas muy extensas y bajos tiempos de medida para una inspección rápida de muchos dispositivos, *iii*) robustez y facilidad de uso y mantenimiento. Como las técnicas experimentales desarrolladas hasta ahora no cumplen simultáneamente todos estos requisitos[51,52], existe la necesidad de desarrollar una técnica experimental capaz de medir rápidamente el espesor en áreas extensas y con buena resolución lateral. Esta necesidad representó mi primera motivación para el desarrollo de una técnica experimental, llamada micro-espectrofotometría multiplexada espacialmente (SMMS), capaz de llevar a cabo la compleja tarea previamente descrita; esta técnica permite la rápida detección de superficies muy extensas de una muestra debido a que el análisis espacial se realiza en paralelo.

Otro aspecto fundamental que hay que considerar a la hora de tratar con resonadores ultra-delgados es el mecanismo de transducción que permite convertir la vibración de una estructura mecánica en una señal eléctrica[53-57]. Durante los últimos 30 años se han desarrollado muchas técnicas experimentales para la detección ultra-sensible de resonadores nanomecánicos, como por ejemplo técnicas ópticas[53,58-60], piezo-resistivas[11,57,61,62], piezo-eléctricas[11,56,63] o magnéticas[64]. En el caso de resonadores ultra-delgados, es muy importante comprender el mecanismo de transducción por dos razones. En primer lugar,

como estos dispositivos poseen una masa muy pequeña, van a oscilar a frecuencias muy altas con pequeñas amplitudes de oscilación. Por este motivo, la medida de estos resonadores requiere una optimización cuidadosa del mecanismo de transducción. Hoy en día, la interferometría óptica representa una de las mejores opciones para el alcance de ultra-alta sensibilidad al desplazamiento[32,54,58,65-67], demostrándose capaz de medir pequeñas fluctuaciones térmicas en estructuras mecánicas alrededor de $\simeq$ fm/Hz$^{1/2}$. A pesar de su enorme potencial, la interferometría óptica va a depender de manera significativa de las características físicas de la fuente de luz utilizada. Por esta razón, en esta parte de mi tesis he estudiado los parámetros físicos más influyentes en la medición interferométrica y cuál es la mejor estrategia para lograr la sensibilidad más alta.

Otro aspecto muy importante relacionado con el mecanismo de transducción es estudiar cómo influye el proceso mismo de detección en las propiedades mecánicas de un resonador[23,68-71]. Este efecto es generalmente despreciable para los resonadores mecánicos normalmente utilizados. Sin embargo, cuando se utilizan resonadores nanomecánicos ultra-delgados, se requiere una cuidadosa minimización del "efecto observador", porque el mismo proceso de detección puede alterar significativamente el estado mecánico de estos dispositivos y por lo tanto disminuir los límites de detección previstos teóricamente. Con el fin de aclarar esta cuestión, en esta parte de la tesis he estudiado la influencia de la detección óptica en palancas ultra-delgadas.

Sorprendentemente, el estudio de este efecto desveló un nuevo mecanismo físico poco estudiado en la literatura, que es el papel de la curvatura en el cambio de las propiedades mecánicas de palancas ultra-delgadas. Este problema es muy importante ya que se encuentra en muchos elementos de la naturaleza, como hojas de plantas[72], alas de insectos[73] o membranas celulares[74], y además tiene un gran potencial en la nanotecnología para el desarrollo de estructuras mecánicas con rigidez reconfigurable[63,69,75,76]. El análisis de este mecanismo físico será estudiado en la última parte de mi tesis, a través de un riguroso estudio teórico y validado luego experimentalmente.

Los principales objetivos de la tesis son los siguientes:

• Desarrollo de una técnica óptica para el análisis espectral de áreas muy extensas de una muestra con resolución lateral micrométrica.

• Análisis de los principales parámetros físicos que afectan a la sensibilidad de un sistema interferométrico y estudio de la mejor estrategia para el alcance de la máxima sensibilidad.

• Estudio de la influencia del proceso de detección en palancas ultra-delgadas inducido por un haz de luz.

• Estudio del efecto de la curvatura en las propiedades mecánicas de palancas ultra-delgadas.

1. Introduction

1.1 Motivation and Objectives

Light mechanical structures that oscillate at high frequencies with a very pure tone have become the basis of a variety of fascinating applications in nanotechnology that includes signal processing[1-8], force sensing[67,77-80], biological[13-21,81,82] and chemical sensing[9-12,83,84], and observation of quantum effects in mechanical systems[22-25]. These structures referred to as nanomechanical resonators can be shaped as cantilevers[26-28], bridges[4-7], membranes[29-32] and can even integrate micro- and nanofluidic channels[14,33-35].

A general trend to improve the performance of a nanomechanical resonator is achieved by the device miniaturization up to the scale of a small nanotube[36] because the tiny mass and the high-frequency resonances of these devices allow the attainment of unprecedented mass sensitivity up to the yoctogram resolution[37]. However, this drastic size reduction is not practical in a large variety of NEMS-based sensing applications as in this case the sensitivity is not the only quantity to be maximized. In sensing applications the need to measure ultra-diluted analytes[27,38,39] sets a detection limit given by the diffusion limit that scales up with the sensor area[8]. Therefore the ideal device would be highly sensitive and with a large capture area; for this reason there is much interest on the development of mechanical structures with ultrathin thickness[29,40-44]. These ultrathin devices represent the best compromise to

measure ultralow analyte concentrations with high-sensitivity. Although ultrathin structures possess a tremendous potential for future sensing applications[45], there are several open issues that need to be addressed. In this thesis I will deepen into some relevant topics related to the use of ultrathin nanomechanical resonators.

The first issue concerning the use of ultrathin structures is that a detailed characterization of their thickness properties is a must[46-49]. Despite the tremendous advances of the lithographic techniques in the fabrication of nanomechanical structures[85], the thickness is very difficult to control during the nanofabrication process[46]. Since the mechanical properties of a resonator highly depend on its thickness[50], in the case of ultrathin structures the thickness uncertainty given by the nanofabrication process represents the most undefined factor in the mechanical variability of these devices. Thickness characterization of nanomechanical devices is a very demanding task, because in addition to thickness vertical resolution, the following requirements are needed as well: *i*) micrometrical lateral resolution due to the small size of each single mechanical device, *ii*) high throughput able to perform rapidly large volume inspections, *iii*) robustness and easy use and maintenance. Since the experimental techniques developed so far do not simultaneously fulfil all these requirements[51,52], there is a need for an experimental technique that allows fast and accurate thickness mapping of millimeter size samples in a cost-effective, simple and robust way. Thereby I developed a new optical technique called Spatially Multiplexed Micro-Spectrophotometry (SMMS) that matches all the cited requirements as the spatial analysis of large sample areas is performed in a parallel way.

A second key element to be addressed when ultra-thin devices are considered concerns the analysis of the displacement transduction mechanism that translates the vibration of the nanomechanical resonator into a measurable electric signal. During the last 30 years many experimental techniques have been implemented for the detection of a vibrating mechanical structure, such as

optical[53,58-60], piezoresistive[11,57,61,62], piezoelectric[11,56,63], magnetic[64] and so on[86]. In the case of the ultrathin resonators, the full understanding of the transduction mechanism is fundamental for twofold reasons. Firstly, as these ultrathin devices possess small active masses, they will oscillate at very high frequencies with small oscillation amplitudes. Therefore, in order to measure this kind of devices, a careful optimization of the displacement transduction mechanism is necessary. Currently, optical interferometry is one of the best choices to achieve ultra-high detection sensitivity[32,54,58,65-67] and it has demonstrated the capability to measure small thermal fluctuations of mechanical structures with sensitivity on the verge of few $fm/Hz^{1/2}$. Despite its huge potential, characterization by optical interferometry is significantly influenced by the physical properties of the detection light source used. For these reasons I studied the physical parameters that can influence the interferometric measurements in order to find the best strategy to achieve the highest sensitivity.

A second important aspect related to the displacement transduction mechanism is the analysis of the influence of the detection process itself on the resonator's mechanical properties[23,68-71]. This effect, known in literature as detection back-action effect, is usually negligible for commonly used mechanical resonators. However, when ultra-thin mechanical structures are used, a careful minimization of the "observer effect" is required because the physical probe used for measuring the resonator displacement can significantly alter the mechanical state of these thin devices and thus diminish the extraordinary fundamental detection limits predicted for such tiny mechanical structures. In order to elucidate this issue, I studied the light-induced back-action effect in ultrathin bimetallic cantilevers.

Surprisingly, the study of detection back-action effect shed light onto a new physical mechanism almost disregarded in literature which is the role of the bending curvature on the stiffness of a singly-clamped cantilever plate. I was motivated to study this intriguing problem because the bending effect can be

ubiquitously found in several natural processes, such as in plant leaves[72], insect wings[73], cell's membrane[74], and moreover, it has a great potential also in nanotechnology to engineer mechanical structures with reconfigurable stiffness[63,69,75,76]. This ancient mechanism found in nature and in man-made structures will be solved theoretically and validated experimentally, shedding light into thin sheet mechanics and bringing new and useful ideas to a wide variety of fields such as natural science, mechanical engineering and micro/nanotechnology[69,76,87-89].

The main objectives of the thesis are the following:

- To develop an optical technique for the fast spectral analysis of large sample surfaces with micrometrical lateral spatial resolution.
- To analyze the main physical parameters that influence the displacement transduction mechanism in an interferometric setup and to find the best strategy for the achievement of the highest sensitivity.
- To examine the detection back-action effect in ultrathin nanomechanical resonators.
- To study the effect of the bending deformation on the stiffness and resonance frequencies of cantilever plates.

All these objectives were addressed experimentally and with the support of analytical theory and/or numerical simulations.

1.2 Thesis Structure

The thesis consists of six chapters that are briefly summarized below:

Chapter 2. A new optical technique, referred to as Spatially Multiplexed Micro-Spectrophotometry (SMMS) technique is presented. The multiplexed capability of the SMMS technique allows the fast polarization-resolved spectral analysis of large sample areas with sub-micrometrical spatial

resolution. The potential of the technique is demonstrated through the dark-field spectral analysis of hundreds of single and dimer gold nanoparticles.

Chapter 3. The capability of the SMMS technique is demonstrated in bright-field mode by performing the spectral analysis of an array of commercial silicon cantilevers in only few minutes. The optical characterization of cantilever surfaces allows the mapping of cantilever thickness with nanometrical vertical accuracy and micrometrical lateral resolution.

Chapter 4. The transduction mechanism of an interferometric setup is studied both theoretically and experimentally by analyzing the main physical parameters that influence the sensitivity of an interferometric setup. The proper optimization of an interferometric setup was demonstrated by the high-sensitivity measurement of several thermal vibration modes in the MHz frequency range of suspended ultra-thin silicon-nitride membranes.

Chapter 5. The detection back-action effect is studied in ultrathin nanomechanical resonators by characterizing the influence of a laser beam on the mechanical properties of ultrathin bilayer cantilevers. This study demonstrated that the light back-action effect has a nonlinear dependence with the power intensity of the laser and it can reduce some resonant frequencies up to a half with laser power absorption of few hundreds of μW.

Chapter 6. The effect of biaxial bending on the stiffness of ultrathin cantilever plates is studied. The huge bending-induced tunability of the stiffness in thin plates is demonstrated in the framework of the linear elasticity both analytically and numerically. The universal scalability of bending effect is later validated by an experiment performed with a macroscopic aluminum plate.

Finally, in **Chapter 7** the most relevant results obtained from this work are summarized.

2. Development of an Experimental Technique for the Optical Characterization of Micro and Nano-Structures

Spectral analysis of samples is routinely performed in a large variety of scientific fields[90-95] such as physics, material science, chemistry, biochemistry and molecular biology. The standard technique commonly used for the spectral analysis of a sample is given by spectrophotometry that consists on the quantitative measurements of the reflection or transmission properties of a material as a function of the light wavelength[51]. Since the aim of standard spectrophotometry is to measure the overall optical properties of a sample, spectral measurements performed with this experimental apparatus correspond to the averaged area of the illuminated sample region, which typically lies in the millimeter range. However, many scientific and technical applications in the field of nanotechnology and material science require optical characterization of a surface with higher spatial resolution[52,93] and, therefore, standard spectrophotometry is not suitable for all this range of applications. During last decades different technical solutions have been developed for spectral analysis of a sample with high spatial resolution, also known as micro-spectrophotometric techniques[46,52,96-102].

Micro-spectrophotometry is a widely used technique for the spectral analysis of a sample surface with micrometrical spatial resolution[52] and since

several decades it has been used for the spatially-resolved spectral analysis of samples in a huge variety of fields, such as forensic science[103], colorimetry[98,100], material science[46,99,102], and biotechnology[101,104]. Standard micro-spectrophotometers can be described as a hybrid instrument that combines the magnifying power of an optical microscope with the spectral capability of an optical spectrometer. In these instruments, a white light beam is tightly focused onto the sample surface through a microscope objective and the reflected or transmitted light coming from the sample is collected and coupled to the entrance aperture of an optical spectrometer by means of an optical fiber or a mirrored aperture.

Currently, standard micro-spectrophotometers have been also widely applied for dark-field spectroscopy of nanoscale objects. The good capability to measure the scattering radiation coming from individual nanostructures has become of primary importance in both fundamental and applied research focused on pure optics, plasmonics and optoelectronics[38,105-113]. The main strengths of micro-spectrophotometry are: (*i*) the spectral characteristics of samples can be mapped with good spatial resolution (few μm), (*ii*) it is a non-destructive test and uses small amount of sample with little or no sample preparation and (*iii*) it has a good versatility as both bright-field and dark-field modes are accessible by simply replacing some optical components in the experimental setup.

The main drawback of standard micro-spectrophotometry is the fact that measurements can be performed only onto a specific sample area, so the spatial mapping of spectral properties on extended areas requires the movement of the sample with a manual or automatic control stage which is usually tedious, costly and time-consuming[46]. For a fixed spatial resolution, the time measurement scales linearly with the sample detection area, thus limiting the use of this technique as an efficient characterization and quality control tool in science and industry. The low throughput of standard micro-spectrophotometry is a limitation in many scientific and industrial applications and for this reason, still today there is a special need for an optical technique able to accurately analyze

spectral properties of large sample surfaces with high spectral and spatial resolution in a faster and simpler manner.

In this chapter it will be described the experimental realization of an innovative optical technique for the fast spectral analysis of millimeter size areas with high spatial resolution, on the verge of few hundreds of nm. This technique, referred from now on as Spatially Multiplexed Micro-Spectrophotometry (SMMS) is cost-effective, simple and robust and it guarantees its feasibility in a wide variety of application fields.

After a detailed description of the SMMS technique in the Section 2.1, in Section 2.2 it will be described the potential of the technique through dark-field spectroscopy of plasmonic gold nanoparticles. All the main advantages of the SMMS technique are finally summarized in the Section 2.3, describing also potential application fields that can benefit of this new experimental method.

2.1 Spatially Multiplexed Micro-Spectrophotometry (SMMS) technique

The spectral characterization of a sample surface requires the acquisition of a tridimensional data set commonly known as spectral cube, as shown in the schematic drawings of Figure 2.1. The X and Y coordinates of the spectral cube represent the sample surface, while the third coordinate is the light wavelength (λ). In standard micro-spectrophotometers, the full spectral analysis of a single point onto the sample is acquired in a one-shot measurement, while the spatial mapping is performed by sequentially scanning point-by-point the sample surface. So, standard micro-spectrophotometers are parallel, or multiplexed, in the spectral coordinate λ and sequential in the spatial coordinates X and Y (Figure 2.1*a*). As will be shown shortly, the way that the entire spectral cube is acquired in the SMMS technique is the main difference as compared to the conventional micro-spectrophotometry. In the SMMS technique the measurement on extended sample surfaces is achieved in a single

measurement for each selected wavelength λ, that is, a parallel measurement in the spatial coordinates X and Y, whereas the spectral analysis is performed sequentially by sweeping the light wavelength λ, (Figure 2.1*b*).

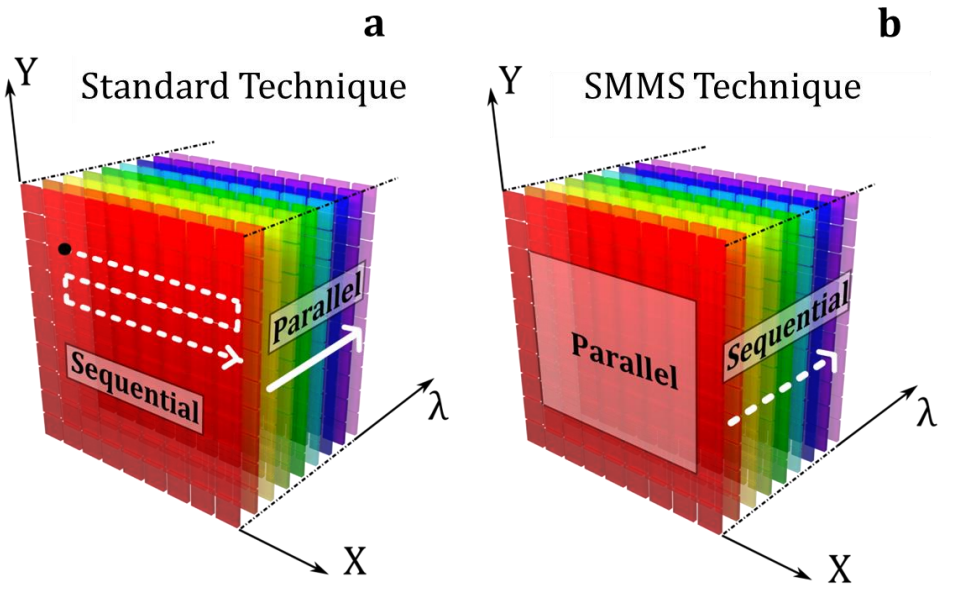

Figure 2.1. (*a*) Working principle of the standard micro-spectrophotometry; the spectral analysis is performed in a parallel way in the spectral coordinate, while the spatial analysis is achieved sequentially. *(b)* Working principle of the SMMS technique; the spatial measurements along X and Y coordinates is acquired in a parallel way (multiplexed), while the spectral analysis is performed sequentially.

In Figure 2.2 a schematic drawing of the SMMS experimental setup configuration in the reflection mode is shown. The working principle of the SMMS technique is based on the sequential illumination of the sample surface at different wavelengths λ and on the detection of the reflected or scattered light coming from a large sample area with a photodetector array.

The practical realization of the instrument was obtained by using a Xenon lamp and a VI-IR motorized monochromator (Tunable PowerArc™ Illuminator, Optical Build Blocks) coupled via a liquid light guide (LLG0538-6,

Thorlabs) and a collimating adapter (LLG5A5-A, Thorlabs) to a commercial optical microscope column (Nikon Eclipse). In order to avoid the overlapping of the second-order diffraction of light coming from the monochromator, a long-wave pass optical filter (GG475, Microbeam, cut-on λ=475 nm) was placed along the illumination arm of the experimental setup. Measurements were acquired with a Peltier-cooled color CCD camera (DS-Ri1, Nikon, working spectral range from 400nm to 700 nm) connected to a PC through a camera controller (DS-U3, Nikon). When polarized-resolved spectral measurements were performed, a linear polarizer (Prinz, M42) placed along the illumination arm of the experimental setup was used. The monochromator light wavelength is routinely calibrated by using a high quality band-pass filter (FL 05632.8-1, Thorlabs, center wavelength λ=632.8±0.2 nm) that ensures a control of the light wavelength with an uncertainty of 0.2 nm.

This experimental configuration can be easily implemented in both bright-field and dark-field modes as long as the appropriate optical components for each of the configurations are used. It is also noteworthy that the SMMS technique can also be used as a standard optical microscope by simply using the zero order diffraction of the monochromator grating.

The measurement of large sample areas (typical range from several hundreds of μm^2 up to few mm^2) using the SMMS technique is much faster than the standard micro-spectrophotometric techniques, because there is no need to make use of control stages for the movement of the sample. Moreover, an important characteristic of the SMMS technique is the absence of an optical fiber along the detection arm that is often used in standard micro-spectrophotometers. The coupling between the fiber and the optical microscope requires the periodic alignment from highly-trained staff because small tilt angles can hugely compromise the performance of the equipment. For this reason the absence of an optical fiber ensures better robustness and easier maintenance to the SMMS technique.

In the following section, the potential of the SMMS technique was demonstrated by performing the polarization-resolved dark-field spectral analysis of gold nanoparticles deposited onto a silicon substrate.

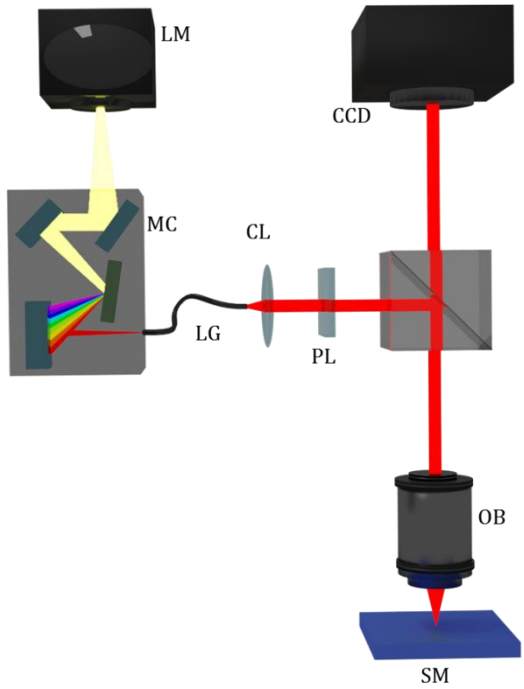

Figure 2.2. Schematic drawing of a SMMS experimental setup in reflection mode configuration. The white light from a lamp (LM) is directed to a motorized monochromator (MC) that disperses the light into its constituent wavelengths. A narrow band of the dispersed spectrum passing from the exit slit of the monochromator is connected to a light guide (LG) and then collimated and focused to the sample (SM) by means of a collimator (CL) and a microscope objective (OB). A high resolution CCD camera placed at the image plane of the experimental setup collects for each single wavelength λ the reflected (bright-field) or scattered light (dark-field) coming from a large surface area of the sample. Light polarization is controlled by a linear polarizer (PL) placed along the illumination arm. The SMMS technique can be employed also as a standard optical microscope by making use of the zero-order diffraction of the monochromator grating.

2.2 Polarization-Resolved Dark-Field Spectral Analysis of Plasmonic Nanoparticles with the SMMS Technique

Metal nanoparticles experience collective coherent oscillations of the conduction band electrons on their surface, a phenomenon known as localized surface plasmon resonance (LSPR)[106,114,115]. The intensity, wavelength and spectral width of these resonances are determined by the size, shape, and material of the nanoparticle, as well as the dielectric constant of the surrounding environment. The capability to tune the plasmon resonances of metallic nanoparticles and the characterization of such responses are at the core of research in nanoplasmonics[116,117,118,110,99,102,119] and it is essential for the development of plasmonic particle-based therapies[110], plasmonic detection of biomolecules[38,120-123], photo-catalysts[124], plasmonic rulers[105,125], nanoantennas[126-129] or surface enhanced Raman spectroscopy[130].

The plasmon response of nanoparticles can be characterized through standard spectrophotometric techniques providing average values of resonance energies and plasmon linewidths of ensembles of nanoparticles, but then the responses are broadened by the unavoidable size and shape dispersion of the nanoparticles. For this reason, practical applications of plasmonic nanoparticles require the characterization of large numbers of nanoparticles with single nanoparticle resolution. Spectral analysis of individual nano-objects is a key aspect for the quantitative comparison to theory[131], to derive information about the morphology or composition (analysis of multilayer spherical nanoparticles) of nanoparticles[132-134] and to optimize the performance of plasmonic nanoparticles[135].

Dark-field spectral analysis is the gold standard optical technique to perform quantitative spectral analysis of single plasmonic nanoparticles. During the last years, several experimental methods have been developed based on

nanoparticle scattering[136,137], absorption[97,138,139] or extinction[140-142]. In most of these instruments, a white light beam is tightly focused onto the sample surface through a microscope objective and the scattered light coming from the sample is collected and coupled to the entrance aperture of an optical spectrometer. A specific nanoparticle is then isolated by closing the spectrograph's entrance slit and centering the nanoparticle on the slit by moving either the sample or the spectrograph. As standard dark-field spectral analyzers need to perform the spatial mapping of a sample surface in a sequential way, the measurement time increases tremendously with the sample detection area making its use not suitable for industrial applications. As described previously in Section 2.1, the SMMS technique has the potential to overcome this typical drawback of standard micro-spectrophotometric techniques due to the capability to measure large sample areas at a fixed wavelength λ in a one shot measurement.

The spectral analysis of a large number of individual nanoparticles represents an excellent test sample to demonstrate all the main characteristics of the SMMS technique, because it requires to combine *i*) a high signal to noise ratio and a high spatial resolution able to detect and distinguish individual scattering objects and *ii*) extended detection area for the fast characterization of statistically significant number of nanoparticles. Moreover, the spectral analysis of this sample was motivated by the fundamental importance to study the effect of the substrate on the plasmonic properties of single nanoparticles. In fact, when a nanoparticle is bounded to a surface, the degeneration of the plasmon modes parallel and perpendicular to the substrate is broken, showing the presence of multiple resonance peaks that have a strong dependence on the incident light polarization and different shapes of the far-field scattering emission[143]. Despite its fundamental importance in different applied and fundamental research fields, such as the study of the Fano-like resonances[136,144,145], the development of highly sensitive biosensors[38] and the selective tuning of the scattering emission both in plasmonic nanoantennas[129] and plasmonic nanorulers[125], experimental studies about this effect are still

scarce in literature due to the lack of a technology with the capability to measure large sample areas with high spatial resolution.

2.2.1 Methods

Sample preparation is critical to ensure the presence of individual nanoparticles within a diffraction limited area[106]. For this reason, a low nanoparticle density of less than 1 nanoparticle per 10 μm^2 is necessary to facilitate single particle spectroscopy analysis. The preparation of gold nanoparticle was performed as following. Silicon wafer was cut in pieces of 5 mm x 5 mm, cleaned with piranha solution (H_2SO_4: H_2O_2, 2:1) for 5 minutes, rinsed three times with Milli-Q® water and dried under a stream of N_2. The silicon surfaces were dipped into a solution 0.001% w/v of poly-lisyne (Sigma-Aldrich) in Milli-Q® water for 1 hour and 25ºC under gentle agitation. The samples were washed twice with Milli-Q® water and dried with N_2. Then the surfaces were dipped into a solution 1 x 10^8 nps/ml of 100 nm diameter gold nanoparticles (coated with 5 nm thick polymer coating, Nanopartz™, USA) in Milli-Q® water for 1 hour and 25ºC under agitation. The silicon surfaces were removed from the gold nanoparticles solution, rinsed vigorously with Milli-Q® water and dried under a stream of N_2.

The spectral characterization was performed by using the experimental setup described in the Section 2.1 in dark-field mode. The use of the SMMS experimental setup in dark-field mode requires the mounting of a beam-splitter and an optical objective specifically designed for dark-field analysis. The measurements were carried out with a 100X dark-field objective (LU Plan Fluor 100X, Nikon, numerical aperture *NA* 0.9) that guarantees a spatial lateral resolution of about 300 nm. Although the magnification of the objective is high, the detection area is still large of 163 µm X 125 µm (0.02 mm^2), thus ensuring the simultaneous measurement of hundreds of individual nanoparticles for each selected wavelength. Polarization-resolved spectral analysis was performed by modifying the polarization axis of the linear polarizer placed along the illumination arm of the experimental setup. P-polarized and S-polarized

illumination correspond to the electric field direction being parallel and perpendicular to the plane of incidence, respectively; the unpolarized illumination was calculated by averaging the spectra of S and P polarized light, i.e. $I_{\mathrm{unpol}} = (I_{\mathrm{S}} + I_{\mathrm{P}})/2$.

As each image frame contains spectral information of hundreds of nanoparticles at the same time, a careful post-processing data analysis is needed in order to isolate the spectral information of individual nanoparticles. In the first step a custom-built routine developed in Matlab® determines all the nanoparticles spatial positions and thus it individuates *i*) all the pixels corresponding to the scattering signal of each nanoparticle and *ii*) an extended doughnut-shaped region placed around each nanoparticle that corresponds to the background scattering coming from the substrate (see Figure 2.3). The algorithm here developed allows also the elimination of eventual saturated scattered objects produced by the presence of large clusters agglomerations or pairs of individual nanoparticles placed at a distance less than the diffraction limit that are saturating the scattering signal in the CCD camera. In the following step every pixel corresponding to the scattering signal I_{scatt} of each nanoparticle (yellow pattern in Figure 2.3) is corrected for the background intensity I_{b} coming from the weak scattering of the substrate (blue pattern in Figure 2.3) and adjusted with a white light spectrum I_{ref} to account for the wavelength response of the experimental setup. The normalized scattered intensity I_{norm} is then obtained according to

$$I_{\mathrm{norm}}(x, y, \lambda) = \frac{I_{\mathrm{scatt}}(x, y, \lambda) - I_{\mathrm{b}}(\lambda)}{I_{\mathrm{ref}}(\lambda)}; \qquad (2.1)$$

I_{ref} was obtained by measuring for each wavelength λ the scattering signal of a white scattering signal (USRS-99-010, LabSphere Inc.) and averaging the signal from all the pixels of the CCD frame while I_{b} was determined for each wavelength λ by averaging between all the pixels corresponding to the background scattering of the substrate, which is the doughnut-shaped region schematically represented by the blue striped pattern in Figure 2.3.

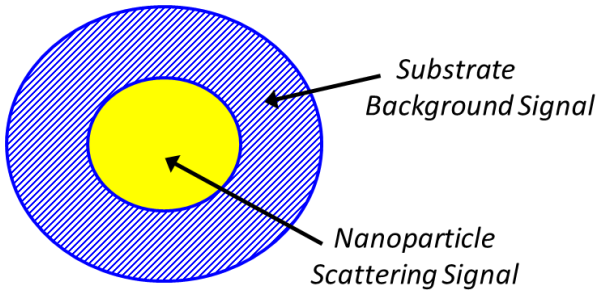

Figure 2.3. Schematic drawing of the *in-situ background correction*.

This *in-situ background correction* is other important advantage of the SMMS technique compared to standard micro-spectrophotometry and it is now possible because the spatial analysis in the SMMS technique is performed in a parallel way. The two main advantages of this new experimental procedure are *i*) there is no-need of an additional measurement for the background correction as in standard micro-spectrophotometry and *ii*) an improved signal-to-noise ratio because the background scattering is measured simultaneously to the nanoparticles scattering, thus guaranteeing that the measurement was indeed performed with the same experimental conditions. In the present experimental conditions the CCD dark-counts (I_{dc}) measured with the light illumination switched off are negligible. This is due to the fast acquisition time of the measurements and the low operating temperature of the CCD camera (-10 ºC); so I_{dc} is not taken into account in the raw data correction described by Equation (2.1). It is also noteworthy that the knowledge of the spatial coordinates of each nanoparticle is particularly important for the development of ex-situ sensing measurements, as it is necessary to perform the spectral analysis of each nanoparticle before and after the sensing experiment. This is now possible with the SMMS technique.

2.2.2 Polarization-Resolved Spectral Analysis

A dark-field image of gold nanoparticles deposited on silicon is shown in Figure 2.4*a*. The image was obtained by illuminating the sample with a broad

light spectrum, condition that is achieved by employing the zero-order diffraction of the monochromator grating. The sample under study contains mainly a mixture of single and dimer nanoparticles, as confirmed by the SEM images shown in Figure 2.4*b*; single and dimer nanoparticles are marked by blue and red circles, respectively. In the present experimental conditions trimers, tetramers and larger agglomerates are detected as saturated scattering signal and were discarded from the analysis. Figures 2.4*c* and 2.4*d* show the far-field scattering of the same SEM surface area of Figure 2.4b obtained at two different wavelengths, 538 nm and 620 nm. Single and dimer nanoparticles present two different scattering patterns depending on the wavelength selected: *i*) a typical Airy pattern with green light illumination (538 nm) and *ii*) a doughnut-shape emission with red light (620 nm). The observed phenomenology is related to the presence of the dielectric substrate that provides a mechanism for symmetry-breaking of plasmon resonances[136,143,146,147].

While a spherical nanoparticle in an isotropic environment exhibits three degenerate dipolar resonances, the reduced symmetry induced by the presence of the dielectric results in the splitting of these modes into two resonance peaks, corresponding to two plasmonic dipoles oscillating parallel (S-mode) and perpendicular (P-mode) to the surface substrate. The energy splitting of the two modes is induced by their interaction with the underneath substrate and the difference in the spatial distribution of the far-field scattering emission is produced by the different orientation of the dipole modes with respect to the surface substrate[136]. Moreover, since the optical response of both the S-mode and P-mode have a strong polarization dependence, their scattering efficiency can be selectively attenuated or enhanced by changing the polarization state of the illuminating source[148].

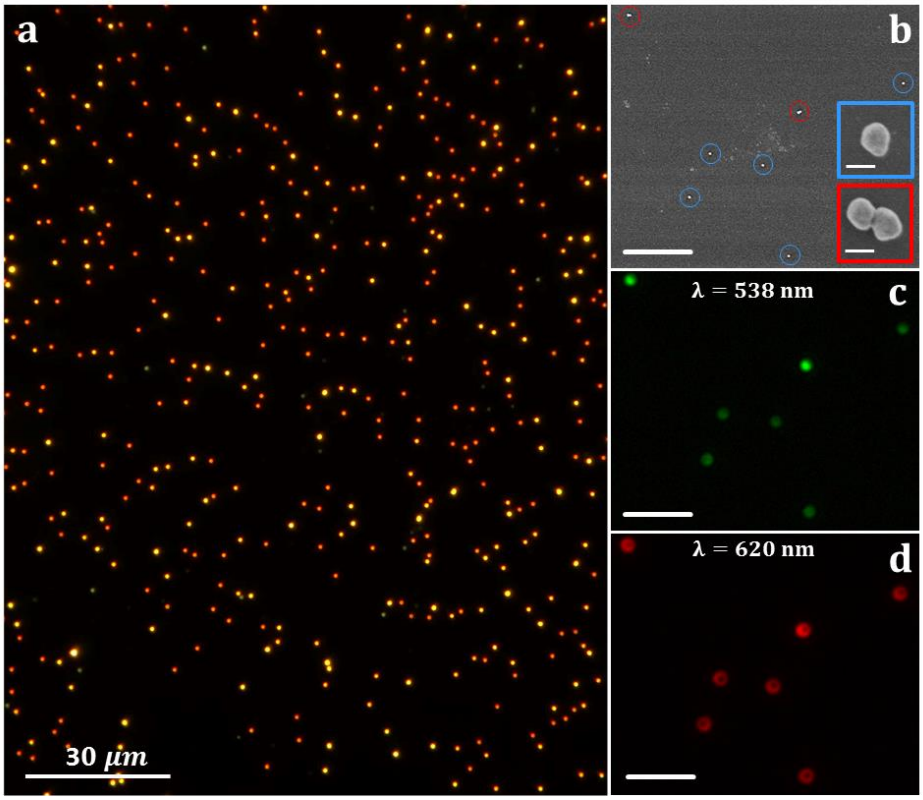

Figure 2.4. (*a*) Optical dark-field image of 100 nm diameter gold nanoparticles deposited onto a silicon substrate. The sample surface is illuminated here with a broad light spectrum by using the zero-order diffraction of the monochromator grating. (*b*) SEM image of a zoomed area of 16 μm X 19 μm, where single nanoparticles and dimers are respectively identified by blue and red circles. The scale bar shown in the figure corresponds to 4 μm. The insets show SEM images of one monomer and one dimer nanoparticle selected from those shown in (b); white bar scales correspond to 100 nm. (*c*-*d*) Dark-field optical images of the same surface area shown in Figure 2.4b, obtained at two different wavelengths; 538 nm (*c*) and 620 nm (*d*). The scale bars correspond to 4 μm.

Normalized scattering spectra of 241 gold nanoparticles obtained with unpolarized illumination are shown in the color contour plot of Figure 2.5*a*; blue color corresponds to single nanoparticles, while red color belongs to

dimers. The entire spectral characterization in the visible spectral range (from 480 nm to 700 nm with steps of 1 nm) was obtained by fixing for each selected wavelength an acquisition time of 300 ms; the overall characterization for each selected polarization was performed in less than two minutes. Taking a look to the whole nanoparticle ensemble, it is clear how single and dimer nanoparticles have very different spectral fingerprint. As highlighted by the black dotted line shown in Figure 2.5*a*, single nanoparticles have a scattering maximum around 600 nm while dimers more efficiently scatter light close to 580 nm. This spectral behavior is caused by the influence of the high refractive index silicon substrate. In order to analyze in detail the spectral features of single and dimer nanoparticles, polarization-resolved spectral analysis was performed by modifying the polarization state of the illumination light.

The polarization-resolved spectra of representative single and dimer nanoparticles are shown in Figures 2.5*b* and 2.5*c*, respectively. The P-polarized and S-polarized illumination correspond to the electric field direction being parallel and perpendicular to the plane of incidence, respectively (see the inset on the top right). The SEM images in Figures 2.5*b* and 2.5*c* correspond to the nanoparticles under analysis. Polarization-resolved scattering spectra performed on a single nanoparticle (Figure 2.5*b*) show two resonant peaks related to a low energy P mode, around 620 nm, and to a high energy S mode that exhibits its maximum close to 540 nm. As mentioned before, the energy splitting between the two modes is due to the different interaction with the underlying silicon substrate. The P-mode, which is a plasmonic excitation normal to the surface substrate, presents a strong interaction with the underneath substrate. Since silicon refractive index is high in the visible spectral range, $n \simeq 4$, a huge red-shift of its plasmon energy is observed. Conversely the S-mode, which is a plasmonic excitation parallel to the surface, localizes the charge further away from the substrate, resulting in a much weaker interaction than that for the P-mode. Moreover, depending on the polarization selected we can enhance or reduce one resonance peak in relation to the other one.[148]

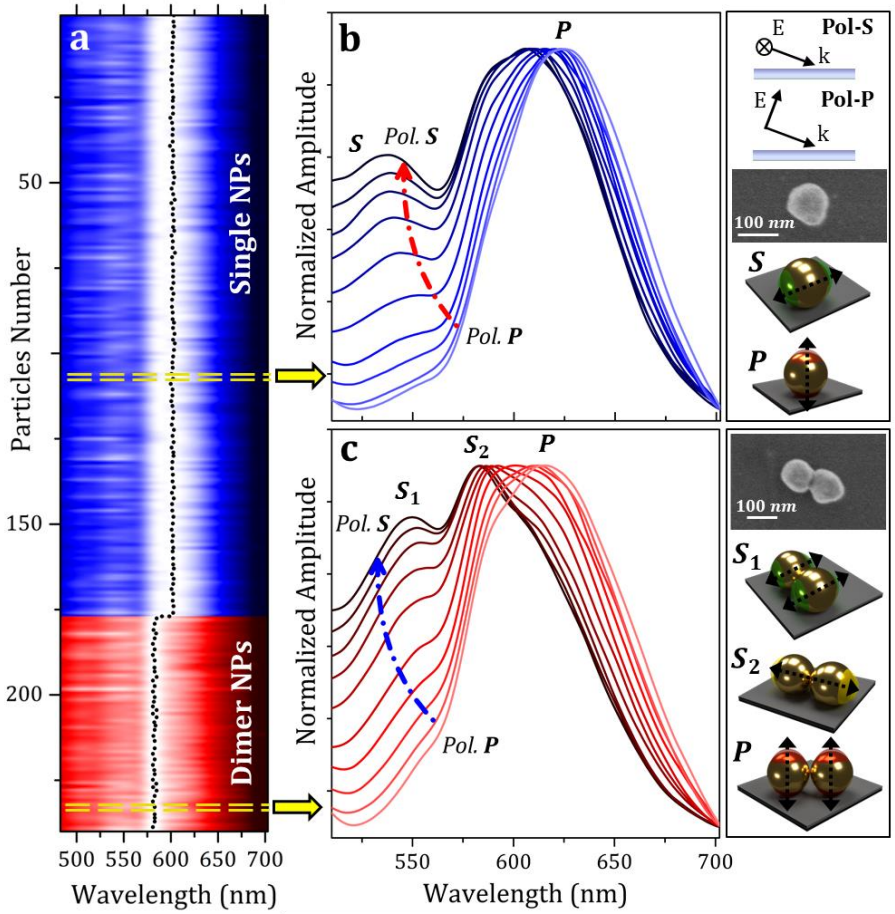

Figure 2.5. (a) Color contour plot of normalized scattering spectra of 177 single (blue color) and 64 dimer (red color) nanoparticles obtained for unpolarized illumination on an imaging area of 0.02 mm^2. The black dotted lines represent the spectral maximum of each analyzed nanoparticle. (b-c) Normalized scattering spectra of a single (Figure 2.5b) and a dimer (Figure 2.5c) obtained at different polarization of the incident light. Insets on the right side show a schematic drawing of the Pol-S and Pol-P illumination source configurations, SEM images of the single and dimer nanoparticles analyzed and a schematic drawing of the dipole plasmon modes observed in the spectra.

In comparison to single nanoparticles, dimer nanoparticle spectra have a more complex behavior[149] (Figure 2.5*c*). The loss of azimuthal symmetry in dimer nanostructures produces the splitting of two different modes oscillating parallel to the surface substrate; the S_1 mode is a plasmonic excitation occurring along the dimer short axis, while the S_2 mode is a dipolar excitation acting on the long dimer axis (see right bottom insets of Figure 2.5*c*). While the S_1 mode and P_1 mode have resonant energies similar to the *S* mode and *P* mode of the single nanoparticle[150], the S_2 mode presents a remarkable red-shift (around 580 nm) because the plasmonic oscillation occurs along the major axis of the dimer. It is important to remark that all the detailed spectral features here reported for individual single and dimer nanoparticles are readily available also for all of the nanoparticles present in the sample (Figure 2.4*a*) due to the high throughput of the SMMS technique that allows the spectral characterization of large sample areas in few minutes.

The experimentally observed spectral positions of single and dimer nanoparticles were therefore corroborated by analytical models and numerical simulations. A qualitative theoretical interpretation about the presence of two different peaks can be obtained from the analytical Mie scattering theory[151] for coated spheres. Scattering spectra of a coated sphere for different refractive indexes of the surrounding environment are shown in Figure 2.6*a*. The S-mode, being a plasmonic excitation parallel to the substrate surface, has a very weak interaction with the underneath substrate and thus, the spectral position of its maximum greatly matches with the Mie scattering spectrum calculated for a refractive index n = 1 (green curve in Figure 2.6*a*). Conversely, the P-mode is a plasmonic excitation normal to the silicon surface and exhibits a strong interaction with the underlying substrate. The huge red-shift of ≈ 80 nm is in good agreement with the Mie Scattering spectrum obtained by considering a refractive index of about ≈ 1.6 (red curve in Figure 2.6*a*). The present qualitative interpretation was also confirmed by numerical simulations performed with finite-difference time domain (FDTD) technique. Numerical analysis, performed with the commercial software Lumerical, considered a

polymer coated gold nanoparticle bound to a silicon substrate and illuminated with S and P-polarized light at an incident angle of ~ 40 degrees. P-polarized light can simultaneously excite both the plasmonic *S*-mode and *P*-mode (black curve of Figure 2.6b), because the electric field of P-polarized light can be decomposed as a sum of two components tangential and normal to the substrate surface. The tangential component of the electric field excites the *S*-mode (left inset of Figure 2.6*b*), while the normal component induces the excitation of the *P*-mode (right inset of Figure 2.6*b*).

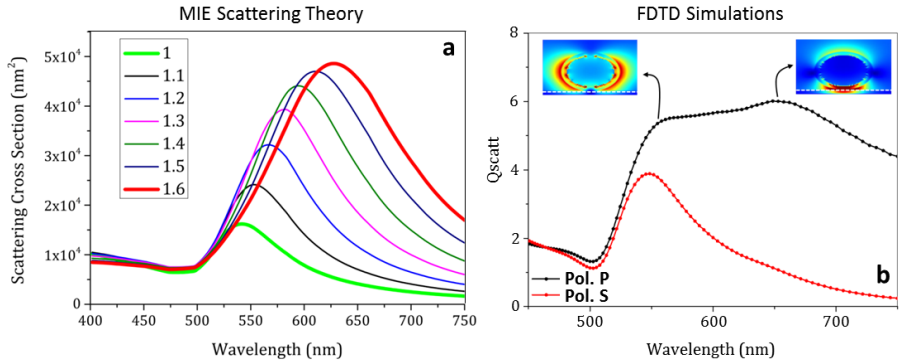

Figure 2.6 *a*) Theoretical scattering cross section obtained with Mie scattering theory of a 100 nm gold nanoparticle coated with 5 nm thick polymer layer calculated for different refractive indexes of the surrounding environment. The dispersive behavior of the gold[152] and silicon[153] optical properties was included in the calculations and the refractive index of the polymer coating was fixed at n=1.5. *b*) FDTD simulations of the scattering cross section of a polymer coated gold nanoparticle bounded to a silicon substrate illuminated with P-polarized and S-polarized light. Numerical analysis was performed by setting an incident angle of ~40 degrees. The two insets represent the spatial distribution of the electromagnetic field of the two dipole plasmon resonances.

In the case of S-polarized light, the scattering spectrum is mainly dominated by the excitation of the *S*-mode (red curve in Figure 2.6*b*), because the electric field in this case has only a component tangential to the substrate surface. However, a careful analysis revealed also the presence of a discrete shoulder peak placed at the spectral position of the *P*-mode (~ 650 nm). For a small

nanoparticle-substrate separation of few nm, the surface mediates an effective interaction between the nanoparticle plasmon resonances resulting in a hybridization of the plasmon resonances[147]. This hybridization takes particular relevance for dielectric substrates with high refractive index such as silicon.

In the following analysis regarding the theoretical study of dimer nanoparticles resonance modes, the S_1 and P_1 dimer modes will not be taken into account, because with good approximation are qualitatively similar to the S and P modes of the single nanoparticle[150]. Conversely, a deeper analysis about the spectral position of the S_2-mode is required. As the S_2-mode is a plasmonic excitation parallel to the substrate surface, the interaction with the underneath substrate is weak and the substrate influence can be considered negligible. The optical response of a dimer nanoparticle immersed in a homogeneous environment can be treated with the analytical model described by Garcia de Abajo[154]. The normalized scattering spectra of a dimer nanoparticle obtained for different inter-particle distances are shown in Figure 2.7; the light illumination is polarized along the longitudinal axis of the dimer.

The spectral position of the S_2-mode strongly depends on the nanoparticles inter-distance and a red-shift is observed by reducing the gap between the two nanoparticles. However, theoretical spectra confirmed a plasmon resonance of the S_2-mode around 580 nm for inter-particle distances of 7 nm, that is plausible with the previous experimental results (each nanoparticle is covered by 5 nm thick polymer coating).

2.2.3 Wavelength-Dependence Analysis of the Scattering Emission

The high spatial resolution of the SMMS technique allows the detailed spatial analysis of the scattering emission of individual plasmonic nanoparticles as well. The shape of the far-field scattering emission is an important fingerprint for both the identification of different plasmonic modes in the same nanoparticle and for the study of nanoparticle-substrate plasmonic coupling.

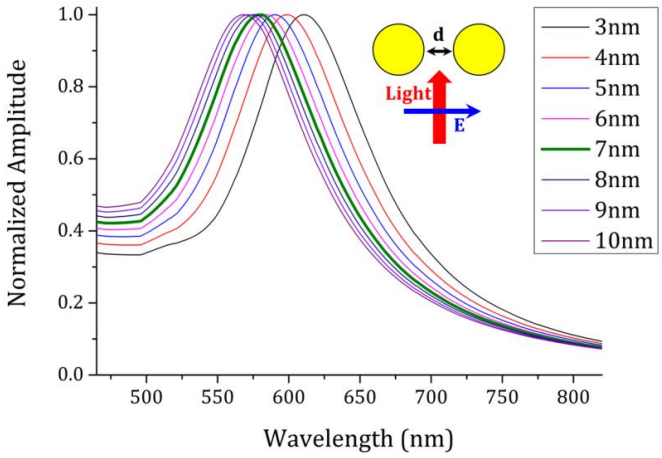

Figure 2.7. Normalized scattering spectra of a dimer for different inter-particle distances; illumination light is polarized along the longitudinal axis of the dimer. The inset in the figure is a schematic drawing of a sphere dimer nanoparticle. The dispersive behaviors of the gold optical properties[152] were included in the calculations and the refractive index of the surrounding environment was set to 1.

Theory predicts the characteristic spatial distribution of the far-field emission depending on the plasmonic modes considered.[125,136,155] Since the size of the nanoparticles under study is much smaller than the wavelength of the incident light, the plasmon resonances of single and dimer nanoparticles can be treated as polarizable electric point dipoles[155]. The dipole moment emanating parallel to the substrate surface (*S*-mode) generates a solid bright far-field scattering pattern, while a dipole moment oscillating normal to the substrate (*P*-mode) is related to a characteristic doughnut shape. Single gold nanoparticles here under study have a clear spectral separation between the *S*-mode and the *P*-mode due to the different coupling with the underneath silicon substrate and, for this reason, it is expected to observe two different scattering patterns in the same nanoparticle depending on the wavelength selected. The capability of the SMMS technique is demonstrated by analyzing the scattering pattern shapes in single and dimer nanoparticles at different wavelengths of the excitation light.

Dark-field images of the same single nanoparticle analyzed in Figure 2.5*b* obtained at three different wavelengths of the excitation light of the visible spectrum are shown in Figure 2.8*a*: at the maximum of the *S*-mode (green, λ_1=540 nm), at the maximum of the *P*-mode (red, λ_3=618 nm) and at an intermediate wavelength (yellow, λ_2=578 nm).

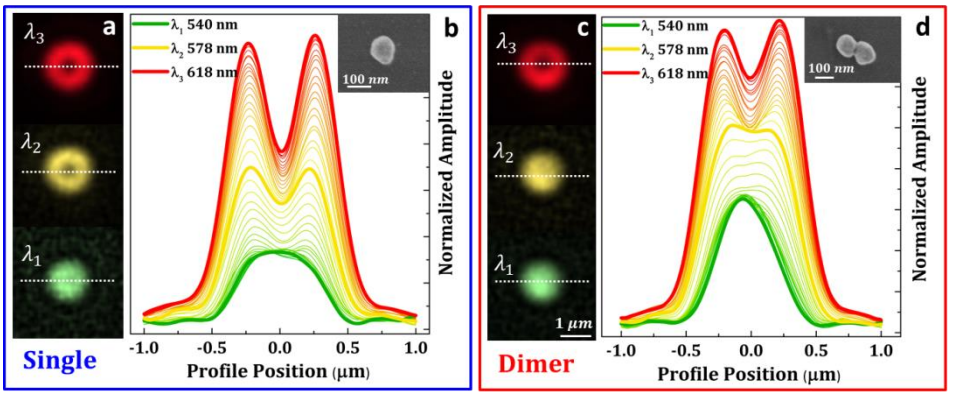

Figure 2.8. (*a*) Normalized dark-field images of the single nanoparticle previously characterized in Figure 2.5*b* at three different wavelengths: λ_1 (540 nm), λ_2 (578 nm), λ_3 (618 nm). Images were obtained with P-polarized illumination. (*b*) Spatial profile of the scattering emission of a single nanoparticle measured along the white dotted lines drawn in Figure 2.8a while changing the wavelength of the light illumination from 540 nm to 618 nm, in steps of 2 nm. Scattering profiles were obtained with P-polarized light. The top inset is a SEM image of the single nanoparticle under study. (*c*) Normalized dark-field images of the dimer nanoparticle previously characterized in Figure 2.5*c* at three different wavelengths: λ_1 (540 nm), λ_2(578 nm), λ_3 (618 nm). The images were obtained with P-polarized illumination. (*d*) Spatial profile of the scattering emission of a dimer measured along the white dotted lines drawn in Figure 2.8*c*. Scattering profiles were obtained with P-polarized light. The top inset is a SEM image of the studied dimer nanoparticle.

A single nanoparticle has a solid bright scattering at the maximum of the *S*-mode (λ_1, green solid pattern) and a typical doughnut-shape at the maximum of the *P*-mode (λ_3, red doughnut pattern). At the intermediate wavelength (λ_2, 578 nm) the scattering has still a doughnut-shape emission

(yellow doughnut pattern), because the scattering is dominated by the *P*-mode. The entire evolution from spherical to doughnut-shape emission can be followed by the SMMS technique, as seen in Figure 2.8*b*, where it is shown the wavelength-dependence of the spatial profile of the single nanoparticle (spatial profiles traced along the white dotted lines shown in Figure 2.8*a*). The unique capability of the SMMS technique to quantitatively characterize the spatial profile highlights that the doughnut shaped scattering emission is significantly broader than the solid bright scattering.

The analysis of the scattering patterns was performed also for the dimer nanoparticle previously analyzed in Figure 2.5*c*. Dark-field images of the dimer obtained both at the maximum of the *S*-mode (λ_1, Figure 2.8*c*) and of the *P*-mode (λ_3, Figure 2.8*c*) are qualitatively similar to the case of the single nanoparticle, while a notable difference can be observed at the intermediate wavelength (λ_2, yellow scattering in Figure 2.8c). At this wavelength, the dimer scattering emission is dominated by the S_2-mode that shows a solid bright scattering pattern. The entire wavelength-dependence of the dimer spatial profiles shown in Figure 2.8*d* allows appreciating the slower transition from spherical to doughnut shape due to the dominancy of the S_2-mode at 578 nm.

The differences seen in the scattering patterns between single and dimer nanoparticles offer a straightforward method to easily distinguish single and dimer nanoparticles from a one shot image with the SMMS technique. In the present experimental conditions, at a wavelength close to 580 nm, the 177 single and 64 dimer nanoparticles can be rapidly discerned by simply analyzing their different scattering patterns, doughnut-shaped or solid bright , respectively, as shown in Figure 2.9. This analysis is possible thanks to two distinctive characteristics of the SMMS technique; its high spatial lateral resolution and the capability to select the wavelength of the excitation light. It is important to remark that this experimental analysis is not feasible with a standard dark-field spectroscopy experimental setup, due to the need of image stitching that deteriorates the shape of the scattering emission.

More importantly, the high signal-to-noise ratio measurements proved by the SMMS technique make now possible to observe previously undetectable scattering features coming from individual nanoparticles; for example at the excitation wavelength of 540 nm the scattering pattern of the single nanoparticle is significantly broader than that of the dimer (Figures 2.8*b* and 2.8*d*). The SMMS provides a new avenue for the spatially-resolved characterization of the far field scattering emission of single and coupled plasmonic systems that is key for the design of nanoantennas[129], the development of plasmonic rulers[125] and to correct variations in SERS enhancement[156-158] from nanostructure to nanostructure. Although the present study was focused exclusively in single and dimer nanoparticles, the SMMS technique has the potential to properly distinguish also trimers, tetramers and larger agglomerates. However, for such analysis, a CCD camera with an extended working spectral range should be used.

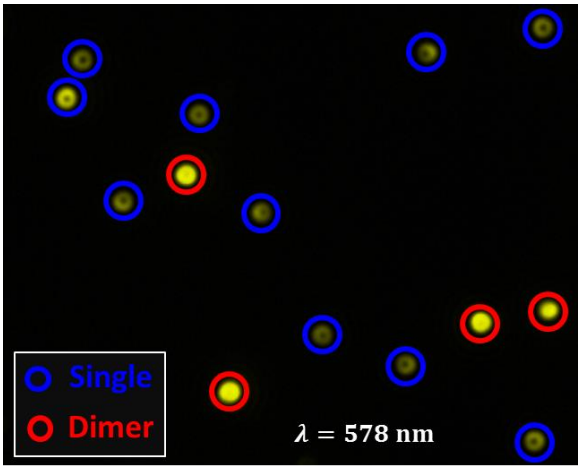

Figure 2 . 9 Single and Dimer NPs at 578nm

Figure 2.9. Dark-field image obtained at 578 nm using P-polarized light. Single (blue circles) and dimer (red circles) nanoparticles can be easily distinguished with a single measurement.

2.2.4 Measurement of the NPs diameter with the SMMS Technique

The capability of the SMMS technique is finally proved with a practical application; the characterization of the diameter of hundreds of single nanoparticles. To this purpose, dimers nanoparticles were identified and eliminated from the analysis and hereinafter only the polarization-resolved spectra of the remaining 177 single nanoparticles will be considered. The nanoparticles appear of different colors in the dark-field images due to the differences in their diameter[54] when there are no changes of the surrounding medium (see Figure 2.10*a*).

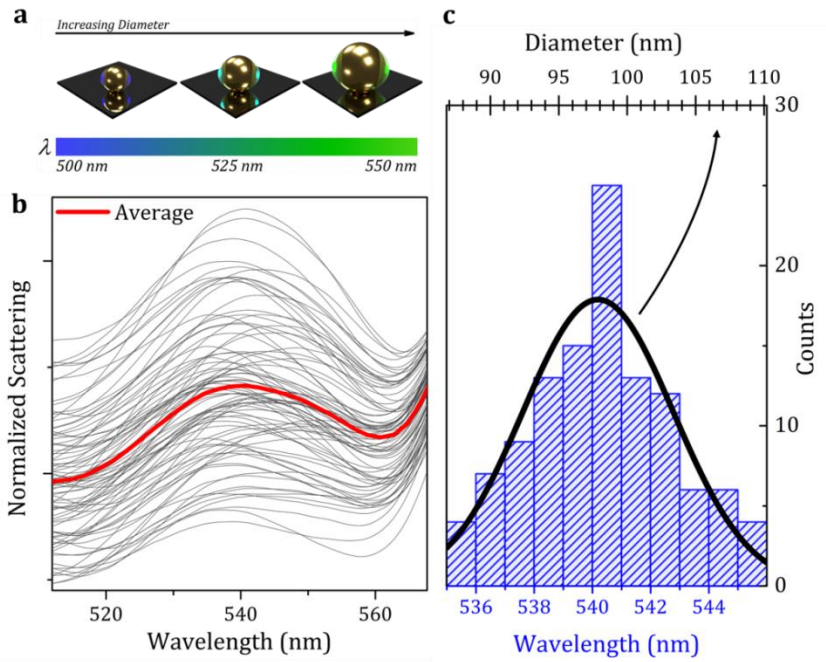

Figure 2.10 (*a*) Schematic drawing representing the wavelength-dependence of the *S*-mode on the nanoparticle size. (*b*) Normalized S-polarized spectra of the 177 single nanoparticles in the spectral range near to the *S*-mode. (*c*) Histogram distribution of the spectral position of the *S*-mode (bottom axis). The solid black line represents the calculated Gaussian distribution of nanoparticle diameter population (top axis).

As the dipole moment oriented parallel to the substrate surface is poorly influenced by possible variations of the substrate refractive index[143], it can be assumed that the spectral shift of its peak depends almost exclusively on differences of the nanoparticle size.

In Figure 2.10*b* it is shown the S-polarized spectra around the maximum of the S-mode of all 177 single nanoparticles (dark gray solid lines) and of their average value (red solid line). The S-peak spectral position of the single nanoparticles presents small spectral changes around the average value of $\simeq 540$ nm. The histogram distribution of the spectral position of the S-peak is therefore calculated, as it is shown in Figure 2.10*c*; the maximum of the S-peak was calculated by fitting the S-polarized spectra of each nanoparticle with two Lorentzian curves that take into account both the S-mode and the P-mode. In the calculus of the histogram distribution all the nanoparticle spectra that were fitted with a fit goodness below than 0.99[159] were discarded.

The spectral position of the maximum of the S-mode can be related to the nanoparticle diameter by considering the analytical Mie scattering theory for coated spheres[151,154,160]. By assuming that the underneath substrate has a negligible influence on the spectral properties of the S-mode[143], the following numerical linear relationship is obtained:

$$D = \alpha + \beta P, \tag{2.2}$$

where D and P represent respectively the nanoparticle diameter and the maximum of the S-peak both expressed in nm, while $\alpha \cong (-1058.9 \pm 0.1)$ nm and $\beta \cong (2.1413 \pm 0.0001)$ are constants obtained by the numerical fitting. The calculations were performed by considering 100 nm gold nanoparticles with a 5 nm thick polymer coating, as specified by the manufacturer. Calculations were performed by including the wavelength-dependence of the gold optical properties[152], while the refractive index of the polymer layer was fixed to 1.5. It is important to remark that the numerical Equation (2.2) is only valid for nanoparticle diameter that deviate few nm from the nominal diameter value of

100 nm. In Figure 2.10*c* the Gaussian distribution of the nanoparticle diameter (solid black line) is also reported, showing an average value of 98 nm $\pm$ 5.4 nm. Although this value is a rough estimation due to the approximations present in the calculation, it is in good agreement with the nominal value and the uncertainty given by the manufacturer (nominal diameter of 100 nm with an uncertainty of 4%). The full analysis of the 177 nanoparticles was completed in only 2.5 minutes.

Advantageously, the diameter of each individual nanoparticle is easily available, because the spatial coordinates of each nanoparticle are also known. This aspect is particularly useful for the development of sensing devices with large multiplexing capability.

2.3 Conclusions

In this chapter a new experimental technique named Spatially Multiplexed Micro-Spectrophotometry (SMMS) was presented. This technique allows performing fast spectral analysis of millimeter-size sample area with sub-micrometrical spatial resolution. The key advantage compared to standard micro-spectrophotometry instruments is the capability to perform the spatial analysis of a large sample area in a parallel way without the need of a time-consuming scanning system. The experimental realization of a SMMS instrument was demonstrated by modifying the illumination arm of a standard optical microscope with a wavelength-tunable illuminator.

The capabilities of the SMMS technique were proven by performing, in minutes, the polarization-resolved dark-field spectral analysis of hundreds of nanoparticles placed on a dielectric substrate with single particle resolution. Gold nanoparticles present a plasmonic behavior that is influenced by the presence of the nearby substrate, resulting in nanoparticle spectra with a strong influence on the incident light polarization and on the scattering emission shape that is wavelength-dependent. Polarization-resolved spectral characterization of 241 single and dimer nanoparticles was demonstrated. The high spatial

resolution of the SMMS technique allows observing details of ~ 40 nm in the spatial distribution of the nanoparticle scattering patterns that in some experimental conditions allowed the rapid discrimination between single and dimer nanoparticles. Moreover, a practical application based on the SMMS technique demonstrated the possibility to rapidly assess the diameter of individual nanoparticles with 1 nm accuracy and in just 2.5 minutes.

The SMMS is optimally suited for characterizing a variety of nanoscale scatterers of different size, shape and material, as well as large assemblies of plasmonic nanoparticles, not viable to techniques that can only address small surface areas. So, fast and high resolution spatially resolved spectral characterization of large sample surfaces is now feasible, offering a new experimental tool in a multitude of application fields in nanoplasmonics. Although the present technique was implemented in reflection mode, the SMMS technique can also be developed in extinction configuration with the same cited advantages. In the following chapter the capability of the SMMS technique will be demonstrated also for the spectral characterization of a sample surface in bright field mode.

3. Fast Thin Film Thickness Characterization with the SMMS Technique

The knowledge of the thickness of thin films is of primary importance in a large variety application fields ranging from construction of integrated circuits in the semiconductor industry[94,161], engineering design of optical coatings[162], performance optimization of thin-film batteries[163] and photovoltaic cells[93,164] and quality control of nanofabrication processes[86].

Optical techniques, such as imaging ellipsometry[165-167], white light interferometry[47-49,168-172] and micro-spectrophotometry[46,52,173-176] are the most used techniques for the thickness characterization of thin films because they are nondestructive methods, do not require any previous sample preparation and they achieve high spatial resolution at the verge of few microns. Imaging ellipsometry is a versatile technique for the non-destructive optical characterization of thin films. However, in this technique only a limited area of the sample surface can be focused due to the inclined observation angle. Thus, a motorized focusing system is needed, increasing the measurement time and the complexity of the equipment due to the need for constant sample focusing[167]. White light interferometry (WLI) was implemented during the last decades for the simultaneous measurement of both the top surface topography and film thickness[177]. Although the WLI is a powerful technique, a critical inconvenience that inhibits its extensive use for film thickness measurement is the fact that it is

very challenging to decouple the film thickness and top surface topography from the data, due to the complex mixture of overlapped interference signals[47,169]. Micro-spectrophotometry is also commonly used for the thickness characterization of thin film[46]. However, since in standard micro-spectrophotometry the spatial mapping of a sample is performed sequentially, the measurement time increases dramatically with extended detection areas and therefore, it could not be feasible both for scientific and industrial applications.

For this reason there is still a need for an experimental technique that allows fast and accurate thickness mapping of millimeter size samples in a cost-effective, simple and robust way. As previously described in Chapter 2, the SMMS technique has the potential to match these requirements, because it can perform the spatial analysis of large sample area in a parallel way.

3.1 Spectral Characterization of Commercial Silicon Cantilevers

Standard cantilevers are excellent candidates to demonstrate the capability of the SMMS technique for thin film thickness characterization. Cantilevers, broadly used in atomic force microscopy and in cantilever sensing applications, are normally fabricated by standard microlithography technologies. Although these techniques have excellent lateral resolution, the uncertainty in thickness of suspended structures is appreciable and compromise dramatically the device performance[178,179]. Moreover, the industrial quality control of micro- and nanofabrication processes is a demanding task, because large volume inspections are needed and high spatial resolution is indispensable as the size under inspection reduces with ever-increased package density.

3.1.1 Methods

High quality commercial silicon cantilevers 500 μm long, 100 μm wide and 1 μm thick (CLA-500-010-08, Concentris GmbH) were used for the experimental characterization. The array of cantilevers is comprised of eight

cantilevers with a pitch of 250 μm from lever to lever connected to the chip through a 6 μm thick pre-clamping region as shown in the SEM images of Figure 3.1*a*.

The spectral characterization was performed with a SMMS experimental setup in bright-field reflection mode configuration. A schematic drawing of the experimental setup is shown in Figure 3.1*b*. As most of the technical details of the experimental setup was previously described in the Chapter 2, in this chapter only the main components of the experimental setup will be described. The white light from a Xenon lamp is directed to a motorized monochromator (Tunable PowerArc™ Illuminator, Optical Build Blocks) that disperses the light into its constituent wavelengths λ. A narrow band of the dispersed spectrum is then coupled through a light guide (LLG0538-6, Thorlabs) and a collimating adapter (LLG5A5-A, Thorlabs) to a commercial optical microscope column (Nikon Eclipse). A CCD camera (DS-Ri1, Nikon) placed at the image plane of the experimental setup collects for each single wavelength λ the reflected light coming from the sample.

Measurements were performed by using a 10X objective (LU Plan Fluor, Nikon, numerical aperture *NA* 0.3). The low magnification of the objective guarantees a large detection area ($\simeq$ 1.2 mm X 1.5 mm), which allows the simultaneous characterization of four cantilevers at the same time. The entire visible spectral characterization (from 538 nm to 700 nm with steps of 1 nm) of the four cantilevers was achieved with a spatial resolution $\sim$1 μm, i.e., the resolving power of the objective used. Every image frame was acquired by setting an acquisition time of 1 ms and the overall spectral characterization took less than one minute. In order to simplify the data analysis, the reflectivity measurement at normal incident angle is recommended. This experimental condition can be achieved by simply modifying the aperture stop of the optical setup. In fact, the aperture stop is an adjustable diaphragm that allows the tuning of the numerical aperture of the light illumination from zero to a maximum angle defined by the numerical aperture of the objective used. The combination

of an optical objective with low numerical aperture and a small aperture stop guarantee the measurement of the sample reflectivity at almost incident angle. This experimental configuration ensures a numerical aperture of the light illumination below 0.05 and thus, the influence of the incidence angle can be considered negligible.

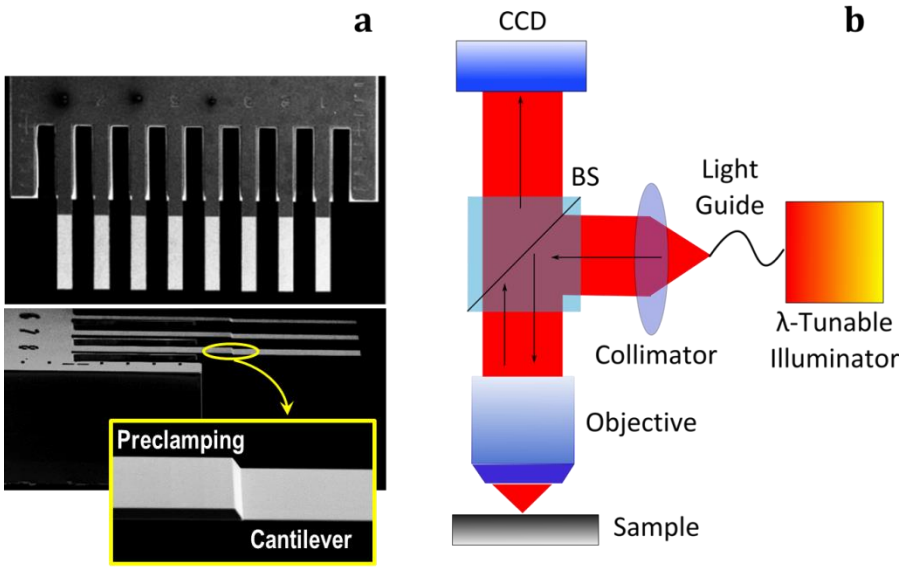

Figure 3.1. *(a)* SEM images of an array of silicon cantilevers. Top image represents the top view of the entire array, bottom image is a perspective view of three cantilevers. The bottom inset is a zoomed SEM image near the cantilever clamping that evidences the frontier between the 6 µm thick preclamping structure fixed to the chip and the 1 µm thick cantilever. *(b)* Schematic drawing of the SMMS experimental setup in reflection mode configuration.

The raw data have to be normalized with a reference sample for two reasons: (*i*) the illuminating source, the CCD camera and all the optical components of the experimental setup are wavelength-dependent and (*ii*) the light source does not illuminate the whole sample surface with spatial homogeneity. The practical procedure requires the normalization of each image frame containing a wavelength component of the sample reflectivity $I(x, y, \lambda)$

by normalizing pixel by pixel the reflectivity spectra of a reference material $I_{\mathrm{ref}}(x, y, \lambda)$, ie

$$I_{\mathrm{norm}}(x, y, \lambda) = \frac{I(x, y, \lambda)}{I_{\mathrm{ref}}(x, y, \lambda)} \tag{3.1}$$

x and y are the spatial coordinate of the sample surface. A silicon bulk sample was used as reference material for data normalization. Hereinafter, the following analysis will be referred to the normalized data.

3.1.2 Experimental Results

Bright-field images of a cantilever and its pre-clamping obtained at different wavelengths λ of the visible spectrum are displayed in Figure 3.2*a*. The cantilever presented differences in reflectivity depending on the selected wavelength λ. This is due to the reflectivity modulation known as Fabry-Perot interference, which arises from multiple reflections that occur inside the thin microstructure[180,181]. This reflectivity enhancement occurs for certain wavelengths in which these multiple reflections generate constructive interference. Conversely, the reflectivity is suppressed for other wavelengths by destructive interference. At the pre-clamping region this optical modulation is negligible due to the absorption of silicon in the visible spectral range that avoids multiple reflections inside a thicker structure.

The color contour map in the bottom of Figure 3.2*b* is the normalized reflectivity change acquired along the cantilever longitudinal position, schematically represented by the white dashed line in the cantilever optical image at the top, as a function of the light wavelength λ. Each point measured along the cantilever exhibits a reflectivity modulation induced by the Fabry-Perot interference [182]. However, the spectral positions of minima and maxima of reflectivity depend considerably on the cantilever position. This feature is more evident in Figure 3.2*c* where the normalized reflectivity changes acquired at three different positions are presented: near the clamping (magenta), at the middle (dark green) and close to the cantilever free end (red). The spectral shift

between the three reflectivity curves is produced by small thickness variations in the cantilever structure generated during the micro-fabrication process.

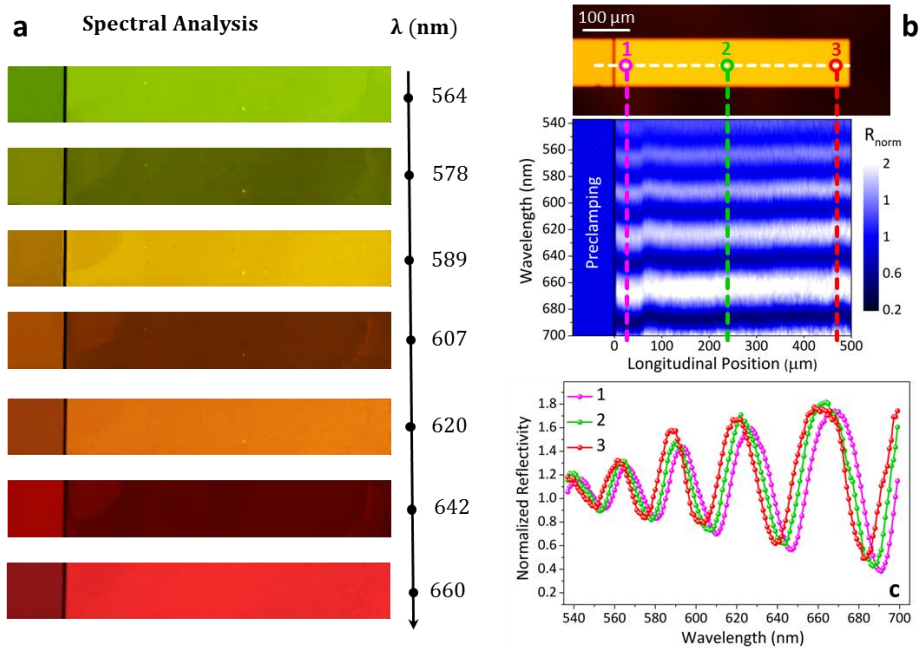

Figure 3.2 (*a*) Bright field images of a cantilever obtained at different wavelengths. (*b*) (Top) Optical image of a cantilever, (Bottom) Color contour plot of the normalized reflectivity as a function of the longitudinal position along the cantilever (white dashed line in the top optical image) and the light wavelength (y-axis). (*c*) Normalized Reflectivity spectra obtained at three different positions along the cantilever.

The thickness d at each point on the cantilever surface was therefore calculated by fitting the normalized experimental data with the following analytical expression[180]

$$\widetilde{R} = \left|\left(\frac{\alpha_+}{\alpha_-}\right)^2\right| \left|\left(\frac{\alpha_+\alpha_-\left(e^{\frac{4i\pi d\tilde{n}}{\lambda}} - 1\right)}{\alpha_+^2 - \alpha_-^2 e^{\frac{4i\pi d\tilde{n}}{\lambda}}}\right)^2\right|, \tag{3.2}$$

that represents the cantilever reflectivity normalized to the reflectivity of the bulk substrate; $\alpha_+ = 1 + n$, $\alpha_- = -1 + n$, i is the imaginary unit and $\tilde{n} = n + i\kappa$ is the complex refractive index, which is the sum of the refractive index n with extinction coefficient κ. The Equation (3.2) that is valid for a light beam with normal angle of incidence, was obtained by combining the Fresnel equations with the transfer matrix technique[182]. The only free parameter of this fitting is the cantilever thickness d, as it is the only unknown physical quantity related to changes in the reflectivity modulation, while the dispersive behavior of silicon optical properties was considered according to Vuye[153].

The thickness mapping of an entire array of cantilevers is shown in Figure 3.3; the cantilever nominal thickness is 1000 nm and the color bar scales represent the cantilever thicknesses along the microstructure in nanometers.

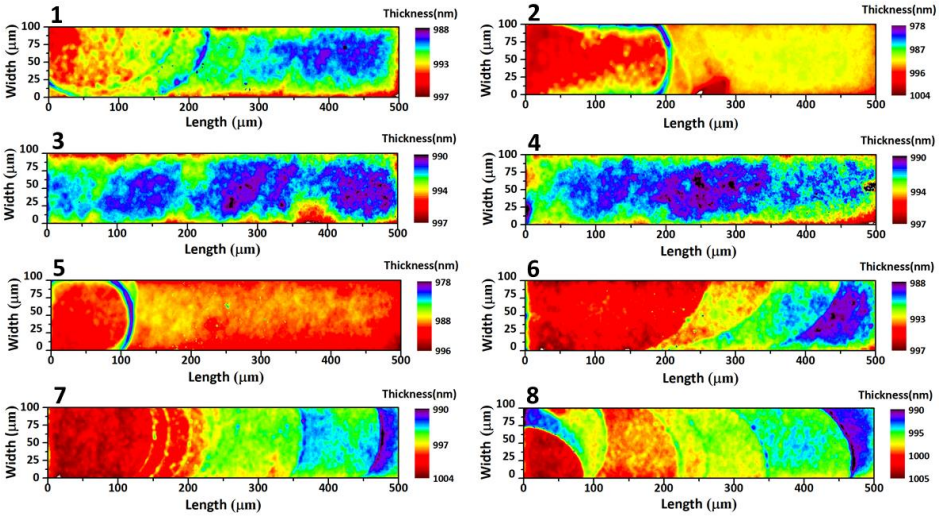

Figure 3.3. Thickness mapping of eight silicon cantilevers from the same chip array; the color bars represent the cantilever thicknesses along the microstructure in nanometers.

The thickness mapping of each cantilever was obtained with around 50k non-linear fittings with a goodness of fit[159] always higher than 0.99. The SMMS technique is able to distinguish thickness variations as low as 1 nm. Thickness

maps reveal significant discrepancies between different cantilevers placed in the same array. For example, cantilevers 3 and 4 present good thickness homogeneity with a root mean square (RMS) thickness variation of about 1.1 nm along all the microstructure. In turn, cantilevers 2 and 7 show higher thickness heterogeneity with a RMS thickness variation of 3.5 nm. It is noteworthy that the cantilevers are usually thicker in the vicinity of the clamping region, getting thinner near the free end. The high spatial resolution combined with the large detection area of the SMMS technique allows quick and precise inspection of micro-fabrication defects in the entire array of cantilevers.

In a recent work, Salmon and co-workers presented the thickness characterization of cantilevers using a standard micro-spectrophotometer[46]. They reported a spatial resolution of 15 μm and a measurement time of 30 minutes for the characterization of an individual cantilever with the same planar dimensions of the ones used in this work. The spatial variation in thickness mapped by the SMMS technique presented higher spatial resolution (1 μm) and, in addition, the measurement of four cantilevers took only one minute. Although micro-fabrication defects can be easily observed also in a routine inspection with a scanning electron microscope, measurements are usually time-consuming, in some cases destructive, and a quantitative analysis of microstructures is generally complex to perform.

3.1.3 Variability Calculation of Cantilevers Mechanical Properties

Thickness control of suspended devices is very difficult to control during the standard nanofabrication process. As most of the mechanical parameters of a resonator strongly depend on its thickness, it represents the most important undefined factor in mechanical variability. The error produced by thickness inhomogeneity can play a crucial role in a large variety of applications, such as calibration of cantilever spring constant in single molecule

force-spectroscopy and scanning-probe microscopy or the mass and surface stress sensitivities in cantilever sensing applications.

A common strategy in nanomechanical sensors is the use of a reference cantilever placed in the same array to eliminate common noise and drift signals from non-specific interactions, variations in temperature, analyte medium refractive index, pressure, etc[183-185]. This approach is implicitly assuming that the reference and sensor cantilevers have the same mechanical responsivity. Although the effect of the thickness inhomogeneity is completely neglected in literature, it can produce appreciable mechanical variability between cantilevers placed in the same chip and for this reason needs to be considered to avoid misinterpretation of results.

The accurate thickness mapping performed with the SMMS technique allows calculating the differences in the mechanical performance produced by thickness inhomogeneity for each cantilever shown in Figure 3.3. In particular it was analyzed: *i*) the *mass sensitivity* $S_{\mathrm{mass}} = \Delta f / \Delta m$, defined as the cantilever frequency shift Δf per unit of mass Δm added onto the cantilever and *ii*) the *surface stress sensitivity* $S_{\mathrm{stress}} = \Delta z / \Delta \sigma$, defined as the displacement of the cantilever free end per unit of uniform and isotropic differential surface stress $\Delta \sigma$ exerted on the cantilever surfaces.

In order to take into account of the cantilever thickness irregularities on mass and surface stress sensitivities, finite element simulations with the commercial software Comsol® were performed. The experimental cantilever thickness is imported in the numerical simulations by generating a parametric surface from the experimental thickness mappings of Figure 3.3. The top cantilever surface is given by this parametrical surface while the bottom surface is completely flat. Mass sensitivity was calculated by evaluating the resonance frequency shift of the first flexural mode before and after the addition of a uniform mass layer onto the cantilever. Numerical simulations after mass deposition were obtained by adding an infinitely thin layer of 10^{-5} kg/m^2 on the bottom face of each of the 8 cantilevers. Surface stress sensitivity was evaluated

by calculating the deflection of the cantilever free end subjected to an isotropic and uniform surface stress onto one side of the cantilever surface. In this case, a shell of 10 nm on the bottom face of each cantilever was added and an initial surface stress of 0.08 N/m was considered. Numerical simulations were obtained by considering a Young modulus E = 170GPa, a material density ρ=2329 kg/m^3 and a Poisson`s ratio ν = 0.28. The calculated average mass and surface stress sensitivity found are 24 Hz/ng and 3.2 nm/(mN/m), respectively. The numerical percentage deviations of mass and surface-stress sensitivities with respect to their mean values are shown in Figure 3.4. The calculations show a deviation in mass and surface-stress between cantilevers in the same array up to 1% and 2%, respectively.

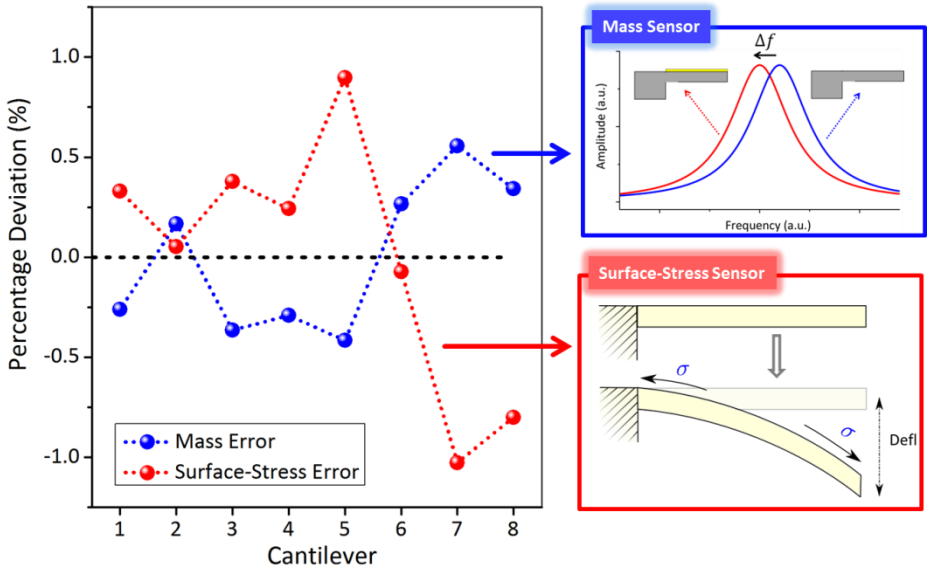

Figure 3.4. Percentage deviation in mass and surface-stress sensitivity with respect to their mean value found for the eight cantilevers from the same array presented in Figure 3.1*a*. (Top inset) - Mass sensitivity was evaluated by calculating the frequency resonance shift produced by the addition of a uniform mass layer deposited on the top cantilever surface. (Bottom inset) - Surface stress sensitivity was evaluated by calculating the displacement of the free cantilever end induced by a uniform and isotropic surface stress exerted on the upper cantilever surface.

The differences in the mechanical properties between the cantilevers of the same array will be examined in a hypothetical sensing experiment: the deformation induced by the immobilization of a densely packed single-strand DNA layer exerting 150 mN/m of surface stress on the top cantilever surface. The deflection differences between cantilevers of the same array can reach up to 10 nm. This difference in sensitivity must be taken into account when comparing the responses between the reference and sensor cantilevers, because its magnitude is of the same order of other noise sources[50] commonly taken into account in a biosensing experiment. Furthermore, assessing the mechanical variability becomes even more important when using large cantilever arrays made of individual chips[186] and in statistical cantilever biosensing[187], where the variability between cantilevers on different arrays can be much larger when compared to the use of a single internal cantilever as reference [185]. It is important to notice that high quality cantilevers were used and the variability in cantilevers sensitivity in the same array can be in the range of a biological recognition[188]. When using standard-quality cantilevers, where the thickness inhomogeneity can be much higher, the differences in sensitivity between cantilevers in the same chip can increase dramatically[46].

3.2 Conclusions

Fast thickness characterization of commercial cantilevers with high micrometrical spatial resolution was performed with the SMMS technique in bright-field mode. The thickness characterization of an entire array of 8 commercial silicon cantilevers can be performed in just 2 minutes and with a spatial resolution of 1 μm. A faster characterization and improved spatial resolution due to the no-need of control stages for the sample movement and the no-need of an optical fiber guarantee at least two order of magnitude shorter analysis time than standard micro-spectrophotometers. The capability of the SMMS technique to observe thickness variation as low as 1 nm allows quick and precise inspection of micro-fabrication defects in the entire array of cantilevers. Although the effect of thickness inhomogeneity is completely

neglected in literature, it can induce an appreciable mechanical variability in cantilevers that needs to be account in order to avoid the misunderstanding of experimental results.

4. Study of the Interferometric Transduction Method for High-Sensitivity Measurement of Nanomechanical Resonators

The aim of the transduction methods in NEMS-based devices is to translate the vibration of a micro- and nanomechanical structure into a measurable electrical signal[189,190]. During the last 30 years many experimental techniques have been implemented for the detection of a vibrating mechanical structure, such as optical[53,58-60,191], piezoresistive[11,57,61,62], piezoelectric[11,56,63], magnetic[64] and so on[86].

The full understanding of the transduction mechanisms is a key aspect in the development and design of new generation NEMS-based sensing applications, because the achievement of the highest sensitivity requires a careful optimization of the detection transduction methods[54,59]. Currently, optical interferometry is one of the best choices to achieve ultra-high displacement detection sensitivity[3,17,29,32,40,42,58,67,192-200] and it has demonstrated the capability to measure small thermal fluctuations of mechanical structures with sensitivity on the verge of few fm/$Hz^{1/2}$. However, there is still a need for a thorough analysis of the influence of the detection light source on the

performance of an interferometric setup, such as its wavelength, polarization, angle of incidence and spatial coherence.

In this chapter, the transduction mechanism of an interferometric setup was studied both theoretically and experimentally through the Brownian motion measurement of a silicon nitride membrane suspended onto a silicon substrate. Several physical parameters that can strongly influence the detection transduction mechanism will be analyzed and the best strategy to achieve the highest sensitivity will be presented. The proposed methodology allowed the characterization of several vibration modes in the MHz frequency range with high signal-to-noise ratio of the silicon nitride nanomechanical resonators.

4.1 Theory of the Displacement Sensitivity in an Interferometric Setup

In a Fabry-Perot interferometric setup, the incident light beam is reflected both by the mechanical resonator and by the underlying substrate (see Figure 4.1). The recombined optical signal, given by the interferometric superposition of different optical paths, is measured by a photodetector. Since the recombined optical signal is sensitive to tiny vertical movements of the mechanical resonator, this optical method allows high-sensitivity measurement of membrane vertical movements.

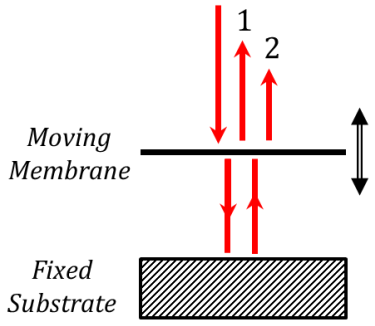

Figure 4.1. Schematic drawing of a Fabry-Perot interferometric setup.

The displacement sensitivity S in an interferometric setup is defined as the absolute value of the change of reflectivity for a given vertical displacement of the mechanical structure[59] i.e.

$$S = \left|\frac{\partial R}{\partial d}\right|, \tag{4.1}$$

where R is the total reflectivity of the suspended mechanical structure and d is the length of the cavity layer underneath the membrane.

The nanomechanical detection in an interferometric setup is usually achieved by making use of an optical objective with a finite numerical aperture *NA* that illuminates the sample surface with a light cone whose acceptance angle $\theta_{NA} = \sin^{-1}(NA)$ is determined by the numerical aperture itself as shown in the scheme in Figure 4.2. As the incidence angle modifies the light optical path and thus the spectral position of the Fabry-Perot interferences, the simultaneous light illumination at different incidence angles produces an overall reflectivity that is given by the superposition of multiple Fabry-Perot optical cavities. Light illumination with a finite numerical aperture adds complexity to the problem, because the calculus of the overall reflectivity is now dependent on the spatial coherence of the light source[182,201,202] and on the polarization state of the light source as well. Theoretical reflectivity of spatially coherent and incoherent light sources can be described by the two following expressions,

$$R_{w,\text{uncoh}} = \frac{1}{\theta_{NA}} \int_0^{\theta_{NA}} |r_w(\theta)|^2 \, d\theta \tag{4.2}$$

$$R_{w,\text{coh}} = \frac{1}{\theta_{NA}} \left| \int_0^{\theta_{NA}} r_w(\theta) \, d\theta \right|^2 \tag{4.3}$$

where the subscript $w = s, p, \text{unpol}$ determines the light polarization state and $r_w(\theta)$ is the complex amplitude of the reflected wave at the incidence angle θ.

Therefore, the use of an optical objective with a finite numerical aperture has as a consequence that the displacement sensitivity will also depend on the spatial coherence of the light source. Theoretical displacement sensitivities of spatially incoherent and coherent light sources are easily obtained by substituting the reflectivity described by Equations (4.2) and (4.3) in the definition of the detection sensitivity given by Equation (4.1).

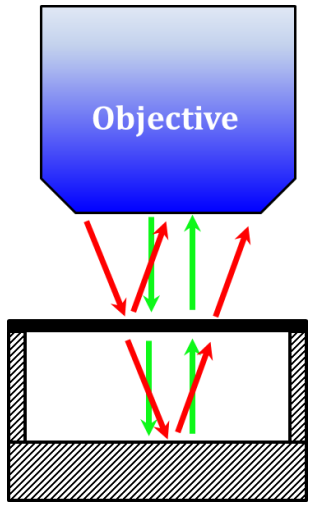

Figure 4.2. Schematic drawing of a Fabry-Perot interferometric setup that implements an optical objective with a finite numerical aperture *NA*. The light source illuminates simultaneously the sample surface with different incidence angles.

The theoretical approach here described is useful for optimizing the design of an interferometric setup. However, as the displacement sensitivity strongly depends both on the optical properties and the geometry of the device, an accurate knowledge of all these physical parameters is needed for its correct analysis. Some geometrical dimensions, such as the layers thicknesses are challenging to control during the nanofabrication process, and their experimental uncertainties are typically higher than those required for the high-sensitivity detection of a nanomechanical resonator. For this reason, the following section will be focused to a detailed experimental characterization of the mechanical devices.

4.2 Characterization of Silicon Nitride Membranes

Arrays of suspended silicon-nitride plates were fabricated by Dr. Zachary James Davis and Dr. Alberto Cagliani of Technical University of Denmark; the plates are suspended onto a silicon substrate and their nominal thickness is 100 nm. A schematic drawing of a suspended plate is shown in Figure 4.3*a*.

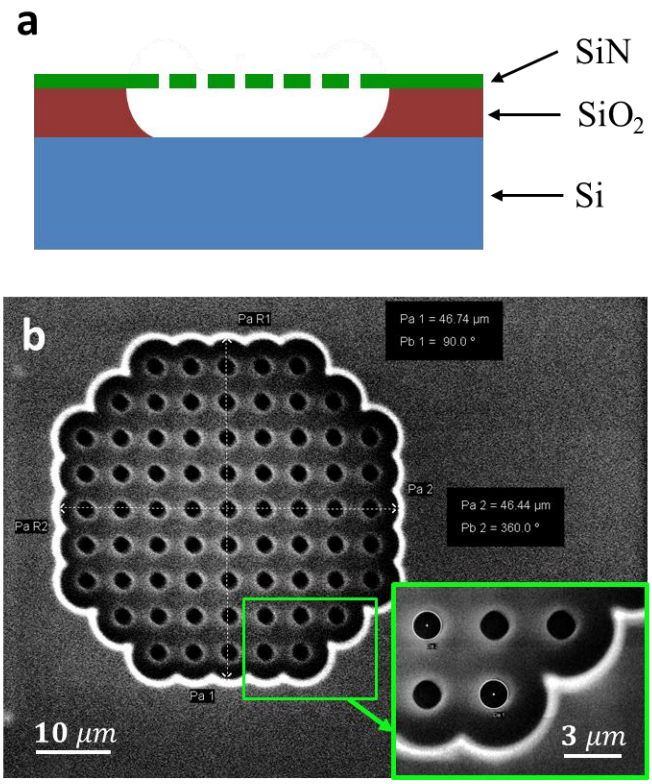

Figure 4.3 a) Schematic drawing of a suspended silicon nitride plate. b) SEM image of a silicon nitride plate; the clamping of the membrane is represented by the bright boundary that surrounds the holey surface while the black circles correspond to the etching holes used during the nanofabrication for the removal of the silicon oxide underneath the suspended membrane. The inset is zoomed area of the mechanical resonator.

The suspended devices have a nominal diameter of 50 μm and a nominal substrate-plate distance of 1270 nm. They were fabricated by growing thermal oxide on a silicon wafer and by depositing a silicon nitride layer with LPCVD. After the oxide and silicon nitride deposition steps, UV lithography and reactive ion etching (RIE) were performed to etch holes into the silicon nitride layer. Finally, the plates were released by controlled etching with wet hydrofluoric acid. Due to the nanofabrication process the structures accumulate a tensile stress on the silicon nitride of ~ 1GPa; more technical details about the nanofabrication process can be found elsewhere[32].

A scanning electron microscopy (SEM) image of a suspended plate is shown in Figure 4.3*b*; the surface of each plate is constituted by a square lattice of 1.5 μm circular holes with a period of 5 μm, necessary during the nanofabrication process for the etching removal of the silicon oxide placed underneath the membranes.

4.2.1 Optical Characterization with the SMMS technique

The optical characterization of a nanomechanical device with the SMMS technique allows the measurement of important geometrical properties of a sample that are typically difficult to control in the nanofabrication process. In the present study both the plate thickness and its distance to the substrate play a crucial role in the optimization of the interferometric transduction mechanism and then, an accurate experimental characterization of both geometrical dimensions with the SMMS technique is needed[59].

As previously described in Chapter 3, the SMMS technique is able to determine the thickness of a thin layer by taking advantage of the Fabry-Perot interferences occurring inside the micromechanical structure. In the following discussion, it will be used the same experimental approach adopted in Chapter

3. Bright-field spectral characterization of the sample was performed both inside and outside the silicon nitride device. In fact, by combining both measurements, important information about the nanofabrication process and the state of deformation of the suspended plate can be obtained. Optical characterization of the sample surface in the visible spectrum from 480 nm to 700 nm with steps of 2 nm was carried out with a 10X optical objective (LU-Plan Fluor 10X, *NA* 0.3). Each image frame was obtained by setting an acquisition time of 10 ms and the overall spectral characterization took less than a minute. In order to eliminate the dependence of the reflectivity measurements on the light incidence angle, measurements were performed at almost normal incidence by setting the numerical aperture of the light illumination close to zero. This experimental condition can be obtained by reducing to the minimum the aperture stop of the optical setup; more technical details about the experimental characterization in bright-field mode were previously described in Chapter 3. The wavelength-dependence of the SMMS system response was eliminated by normalizing raw data with the reflectivity spectra of a bare silicon substrate. Hereinafter, the following analysis will always refer to the normalized data.

Fabry-Perot interferences in the reflectivity spectra are expected to be observed both inside (blue arrow, Figure 4.4a) and outside (black arrow, Figure 4.4b) the suspended structure. These regions correspond to two different optical cavities given by the superposition of thin dielectric layers (see Figure 4.4*a*).

On top of the suspended device, the optical cavity is given by the silicon-nitride plate and the underneath air layer (blue arrow), while outside the suspended plate, the cavity is formed by a silicon nitride layer and the underlying silicon oxide (black arrow). Normalized reflectivity spectra measured both inside and outside of a suspended plate (blue and black solid symbols, respectively) are shown in Figure 4.4*b*.

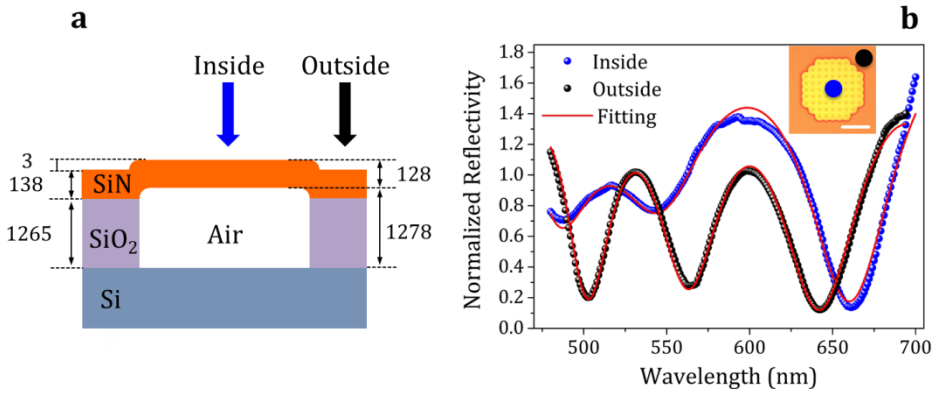

Figure 4.4 *a*) Schematic drawing of the suspended silicon-nitride plate with the calculated geometrical parameters (in nm) obtained by the fitting of experimental data. *b*) Experimental measurements of the normalized reflectivity measured inside and outside the suspended plate (blue and black solid symbols respectively) are shown. Fitting of experimental data are represented by red solid lines; the coefficient of determination R^2 inside and outside the suspended mechanical structure results 0.996 and 0.997 respectively. The top inset is an optical image of the measured drum-shaped resonator; the white scale bar corresponds to 20 μm.

Experimental results were then compared with theoretical reflectivity obtained through the calculus of a plane monochromatic wave propagating through four dielectric layers[182] :

$$R = \left|\frac{a_- + b_+}{a_+ + b_-}\right|^2, \tag{4.4}$$

where $a_{\mp}$ and $b_{\pm}$ are given by

$$\begin{aligned} a_{\mp} = \big[&e^{-\phi_1+\phi_2}(n_0 \mp n_1)(n_1 - n_2) \\ &+ e^{\phi_1+\phi_2}(n_0 \pm n_1)(n_1 + n_2)\big](n_2 - n_3) \\ b_{\pm} = \big[&e^{\phi_1-\phi_2}(n_0 \pm n_1)(n_1 - n_2) \\ &+ e^{-\phi_1-\phi_2}(n_0 \mp n_1)(n_1 + n_2)\big](n_2 + n_3); \end{aligned} \tag{4.5}$$

the subscripts correspond to the order number of the layer considered, being 0 the top layer and 3 the bottom layer. The phase $\phi_m = 2i\, d_m n_m\, \pi/\lambda$ with $m = 1,2$ is the optical path, being d_m the thickness of the layer m and n_m its complex refractive index. Theoretical reflectivity defined in Equation (4.4) was then normalized to the reflectivity of the silicon substrate $R_{\mathrm{ref}} = \left|\frac{1-n_3}{1+n_3}\right|^2$, obtaining the following equation:

$$\bar{R} = \frac{R}{R_{\mathrm{ref}}} \tag{4.6}$$

As the materials used for the sample fabrication are known a priori, fitting analysis (red solid curves in Figure 4.4*b*) was performed by considering as free parameters only the two thin films thicknesses d_1 and d_2, which are the experimentally unknown parameters. The dispersive behavior of materials optical properties was taken into account according to tabulated data found elsewhere[153,203,204]. Fitting analysis performed on 48 mechanical devices gives a devices thickness of d_{plate}= (128.4 ± 0.4) nm and an air cavity layer of d_{air} = (1278.3 ± 0.8) nm. Outside the suspended devices it was calculated a thickness of d_{SiN} = (138.1 ± 0.3) nm and d_{SiO2} = (1265.4 ± 0.7) nm for the silicon nitride and silicon oxide layers, respectively. The average values and their uncertainties here found confirm the high thickness homogeneity of the mechanical devices under study over large surface areas (≃ 1.8 mm^2). Moreover, important information about the nanofabrication process and the initial out-of-plane static deformation of the mechanical structures can be obtained. Firstly, the thickness of the suspended plates is ≃ 10 nm thinner than the silicon nitride layer. This is due to the increase of the etching rate in the holey suspended plates due to an increase of the contact area of the silicon nitride layer with the wet etcher (hydrofluoric acid). Secondly, the air layer under the suspended plates is about ≃ 13 nm thicker than the silicon oxide layer. As it is shown in the schematic drawing of Figure 4.4*a*, the increase of the air gap underneath the suspended structures is due to: *i*) the previously discussed 10 nm thinning of the suspended

silicon nitride plates and *ii*) the upward static deformation of the suspended plates of about ≃ 3 nm.

The upward deformation of the plates comes from the tensile stress accumulated inside the mechanical structure during the nanofabrication process. The quantitative measurement of the accumulated tensile stress is fundamental for the accurate determination of the mechanical properties of the nanomechanical structures[42,57,205] and therefore, the following section will be focused on the experimental and numerical analysis of the plates static deformation.

4.2.2 AFM Measurement of the Static Deformation and Numerical Analysis

The self-standing structures are in a deformation state due to the tensile stress accumulated during the nanofabrication process. An accurate measurement of the tensile stress is of key importance for the mechanical characterization of fully-clamped plates, because the mechanical properties of such structures dramatically depend on the stress accumulated inside the device material[200]. In order to corroborate the experimental results found with the SMMS technique, the static deformation of the suspended resonators was characterized with a commercial atomic force microscope in tapping mode (Bruker Multimode AFM with a Nanoscope V controller).

AFM measurements shown in Figure 4.5*a* confirmed an upward static deformation of ≃ 2 nm that is consistent with the optical characterization performed previously with the SMMS technique (≃ 3 nm). The AFM measurements of the deformed plate were therefore used in finite element simulations to extrapolate the initial tensile stress necessary to induce a deformation in the plate. Numerical simulations, performed with the commercial software Comsol®, considered the real shape of the mechanical structure by taking into account the geometrical dimensions of the suspended structure and of the etch release holes measured with SEM and the SMMS

technique. Numerical analysis consisted on the stationary study of a mechanical structure subjected to an initial tensile stress and it was performed in a range of tensile stress around the nominal value of 1 GPa, from 0.85 GPa to 1.15 GPa. The dependence of the initial tensile stress as a function of the static deformation of the suspended plate is shown in Figure 4.5*b*.

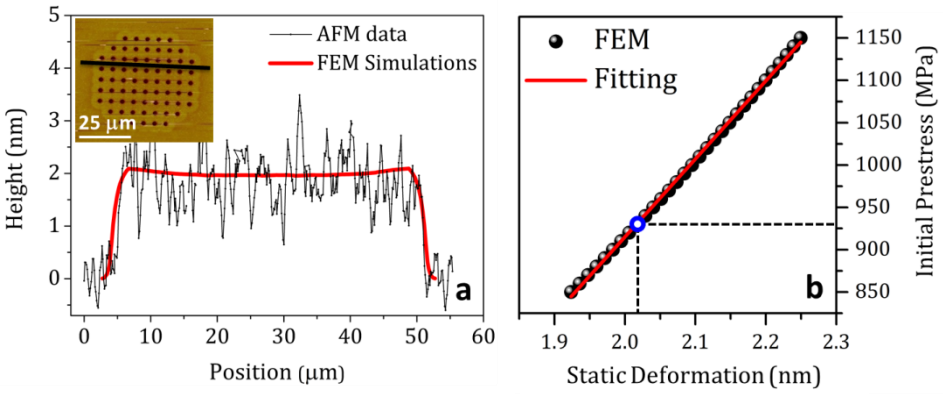

Figure 4.5 (*a*) The black curve shows the spatial profile of the topography measured with AFM along the black line drawn in the top inset. The red curve shows the static deformation numerically calculated with FEM by considering an initial tensile stress of 927 MPa. (*b*) Dependence of the initial tensile stress as a function of the plate static deformation calculated with FEM (black solid circle); the red solid curve represents the linear fitting to the numerical data. The coefficient of determination R^2 of the linear fitting is 0.996. The empty blue circle represents the initial tensile stress that best approximates to the experimental spatial profile shown in Figure 4.5*a*.

The tensile stress P exhibits an almost linear dependence with the plate deformation H; the numerical results were fitted to the linear function

$$P = \alpha H + \beta, \tag{4.7}$$

obtaining $\alpha = (922 \pm 5)$ MPa/nm and $\beta = (-929 \pm 10)$ MPa. The red solid curve in Figure 4.5*a* represents the numerical spatial profile of the membrane displacement obtained with an initial tensile stress of 927 MPa.

The stress accumulation inside a fully-clamped plate strongly modifies its mechanical properties, because the anchor region in these mechanical structures prevents the relaxation of the stress by expansion or contraction. Previous works found in the literature evidenced the high-tunability of both the frequency resonance and the quality factor of doubly-clamped mechanical resonators[76,206-209], envisioning the possibility to design highly-sensitive tunable mechanical filters. For clamped structures with low accumulated stress (typically below 100 MPa), known in literature as plate-like structures, the resonance frequency is mainly dependent on the flexural rigidity of the plate and the influence of the internal stresses is negligible[55,127,210,211]. Conversely, when higher values of stress are accumulated inside the mechanical structure (typically higher than few hundreds of MPa), the resonance frequency is exclusively determined by the inner stress accumulated and the flexural rigidity has a minimal influence; these mechanical structures are known in literature as membrane-like resonators[4,5,7,31,209,212,213]. The tensile stress measured in the silicon-nitride plates used here is about 900 Mpa, confirming that these devices are membrane-like mechanical structures. Hereinafter the term *membrane* will be adopted for these structures for the sake of simplicity. The resonance frequencies $f_{n,m}$ of a circular membrane are well described by the following equation[214]

$$f_{n,m} \cong \frac{\xi_{n,m}}{\pi D}\sqrt{\frac{\sigma}{\rho}}, \tag{4.8}$$

where σ is the applied tensile stress, D is the membrane diameter, ρ the material density and $\xi_{n,m}$ are the m^{th} zeros of the Bessel function $J_n(x)$, hence the tuple (n, m) refers to the azimuthal and radial mode numbers, respectively. A rough estimation with Equation (4.8) gives a resonant frequency for the fundamental mode (0,1) around 8.6 MHz, that is in agreement with the experimental data that will be shown in Section 4.4. This estimation was obtained by considering $D = 50$ μm and $\sigma = 927$ MPa. The presence of the holes in the membrane was taken into account by considering an effective value for the material density $\rho_{eff} =$

$\alpha\,\rho_{SiN}$, where $\rho_{SiN} = 3100$ Kg/m^3 is the silicon nitride material density and $\alpha = 0.94$ is the ratio between the volume of the membrane without and with the etching release holes.

4.3 Calculus of the Displacement Sensitivity

The calculus of the displacement sensitivity is firstly provided by considering the case of a light beam normally incident to the sample surface. In this case, the displacement sensitivity S is obtained by simply substituting the total reflectivity R described by Equation (4.4) and (4.5) into Equation (4.1). The wavelength-dependence of the displacement sensitivity S and of the absolute reflectivity R of the devices is shown in Figure 4.6; the calculation was performed by considering the devices geometrical dimensions found in Section 4.2.1. The displacement sensitivity exhibits a strong wavelength-dependence and the minimum values of sensitivity, being zero, confirms that at certain wavelengths no vertical displacement of the resonator can be measured. Moreover, one should be aware that at first sight the displacement sensitivity S seems to be equivalent to the wavelength derivative of the reflectivity $\left|\frac{\partial R}{\partial \lambda}\right|$. However, these two quantities are not equivalent. In the definition of the sensitivity, S, given by Equation (4.1), just one physical property of the two optical cavities is changing, that is the air thickness layer underlying the membrane, while when the expression $\left|\frac{\partial R}{\partial \lambda}\right|$ is considered, both the optical path inside the suspended membrane and the underneath air cavity are modified.

The results confirm that for a light beam normally incident to the sample, the only physical parameter that influences the displacement sensitivity is given by the light wavelength. However, as previously described in Section 4.1, in most of interferometric setups the light illumination is provided by an optical objective with a finite numerical aperture, that simultaneously illuminates the sample at different incidence angles. Light illumination with a finite numerical aperture adds complexity to the problem as the overall

reflectivity depends on the numerical aperture of the objective used, the light polarization and the spatial coherence of the light source[182,201,202].

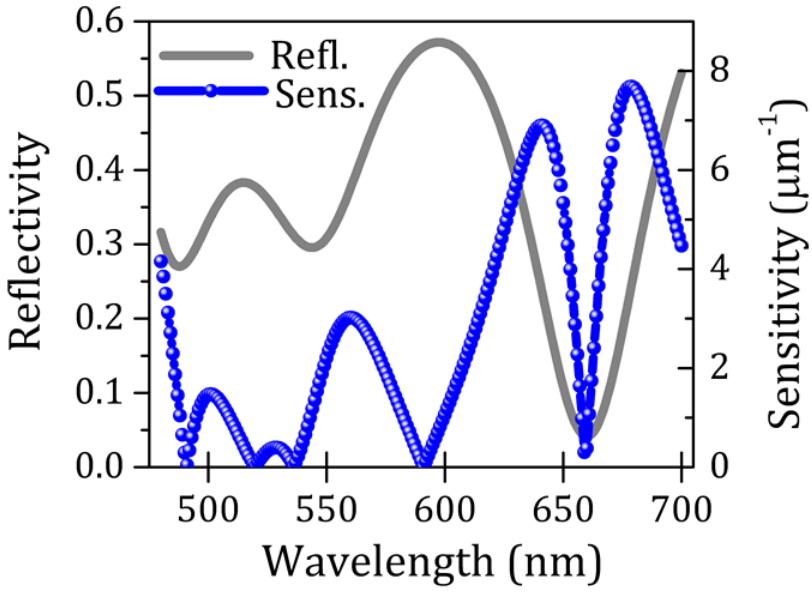

Figure 4.6. Wavelength-dependence of the interferometric sensitivity (blue solid circle) and of the absolute reflectivity (solid gray line) at normal incidence angle. Reflectivity *R* described by Equation (4.1) was calculated by using the thickness of the two layers d_{plate} and d_{air} previously obtained in 4.2.1.

Normalized reflectivity spectra of a silicon nitride membrane obtained for different numerical apertures (from 0 to 0.65) by illuminating the sample with a spatially incoherent and unpolarized light source are shown in Figure 4.7*a*. The normalization was obtained by dividing the theoretical curves with the reflectivity spectra of a bare silicon substrate. Reflectivity spectra point out how the increase of the numerical aperture induces an attenuation of the reflectivity modulation, due to the increased number of multiple Fabry-Perot cavities that are contributing to the overall reflectivity. Theoretical predictions were experimentally confirmed by measuring the reflectivity spectra of the silicon nitride membranes at different numerical apertures and by illuminating the sample surface with an unpolarized Xenon lamp (Figure 4.7*b*).

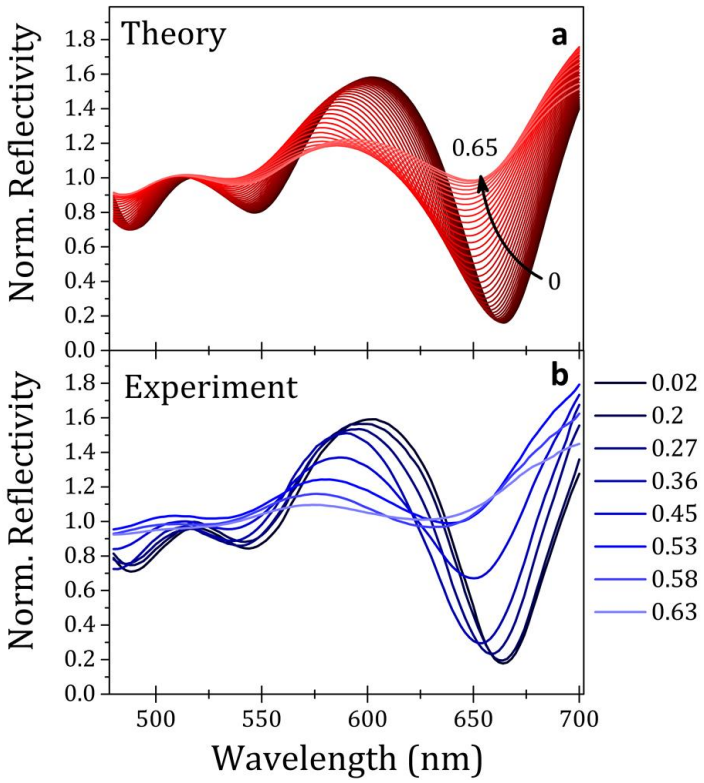

Figure 4.7. *a*) Theoretical spectra of the normalized-reflectivity calculated for different numerical apertures and obtained for a spatially incoherent and unpolarized light source. Calculations were obtained by considering the same material and geometrical properties of the suspended membranes characterized in Section 4.2.1. *b*) Experimental normalized reflectivity spectra obtained for different numerical apertures by illuminating the sample with an unpolarized Xenon lamp.

The numerical aperture of the illuminating light was experimentally controlled in the following manner: *i*) by using optical objectives with different magnification (10X, 20X and 50X) and *ii*) by modifying the aperture stop of the optical microscope. Hence, the effective numerical aperture is given by a combination of the numerical aperture of the objective and the aperture stop of the optical setup. Additionally, in the experiments it was found a progressive attenuation of the reflectivity modulation by increasing the numerical aperture.

The values of the numerical apertures shown in the legend of Figure 4.7*b* were estimated after a comparison with the theoretical data.

A strong dependence on the numerical aperture is also observed in the calculus of the displacement sensitivity. The color contour plots of Figures 4.8*a* and 4.8*b* represent, respectively, the membrane theoretical displacement sensitivity of incoherent and coherent unpolarized light sources as a function of the light wavelength and the numerical aperture of the optical system. Figures 4.8*c* and 4.8*d* show respectively the theoretical displacement sensitivity spectra for spatially incoherent and coherent light sources for four different numerical apertures: 0, 0.2, 0.4 and 0.6. The displacement sensitivities of both spatially coherent and incoherent light illumination are almost identical for low numerical apertures (below 0.1) and qualitative differences can be observed for numerical apertures higher than 0.2. In the case of spatially incoherent light sources, the increase of the numerical aperture smooths the spectral dependence of the displacement sensitivity. Conversely, the spectral dependence of the displacement sensitivity for a spatially coherent light source does not exhibit a smoothed effect while increasing the numerical aperture; for high numerical apertures, maxima result spectrally shifted and slightly attenuated while minima besides to be spectrally shifted goes to zero such as in the case of zero numerical aperture.

As the main goal consists on the maximization of the displacement sensitivity, the optimum strategy for spatially coherent and incoherent light is the use of light wavelength close to the maxima and of an objective with low numerical aperture (maxima of black curves of Figures 4.8*c* and 4.8*d*), because the displacement sensitivity tends to decrease for higher numerical apertures. However, as it is commonly difficult to find light sources operating at a given wavelength, in most of the practical experiments the right choice of the light wavelength could be not feasible. In this case a careful tuning of the numerical aperture of the light illumination could improve the displacement sensitivity of the interferometric setup. In particular, if the available light wavelength is close to the minima of sensitivity for normal incidence angle (minima of black curves

of Figures 4.8*c* and 4.8*d*), the use of an objective with high numerical aperture could significantly enhance the sensitivity of the setup.

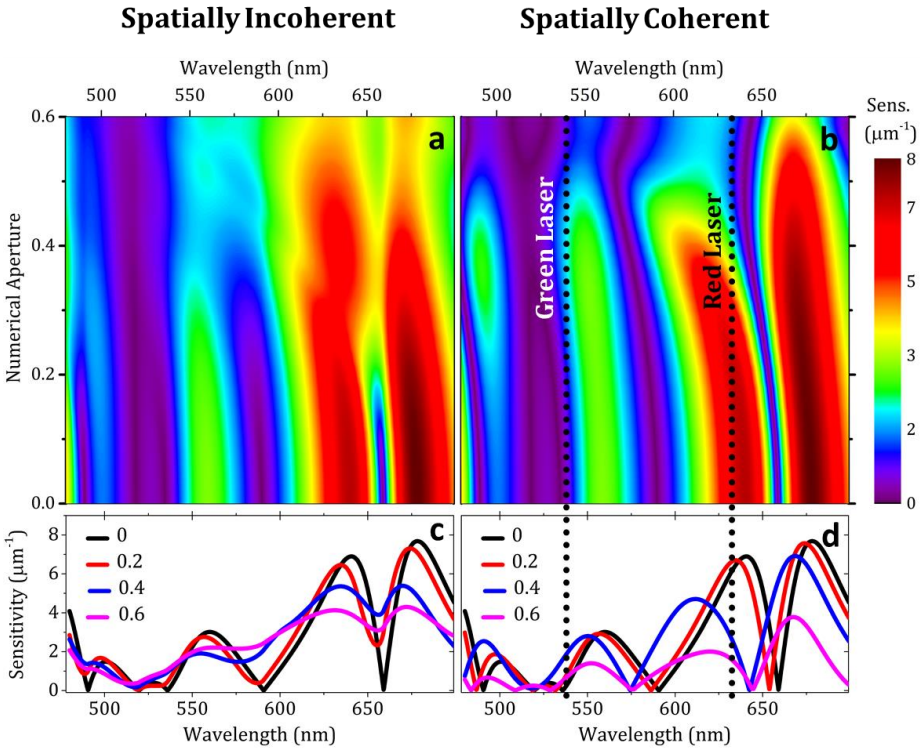

Figure 4.8 (*a-b*) Color contour plot of the theoretical displacement sensitivity calculated for spatially incoherent and coherent light sources as a function of the wavelength and the numerical aperture. *c-d*) Spectral response of the theoretical displacement sensitivity calculated respectively for spatially incoherent and coherent light sources at four different numerical apertures: 0, 0.2, 0.4 and 0.6. The dotted vertical black lines shown in Figures 4.8*b* and 4.8*d* are the wavelengths of the two laser sources used for the experiments. Calculations were performed by considering a silicon nitride membrane with the same material and geometrical properties found in Section 4.2.1.

These results can be useful for the design of an optimized interferometric transduction mechanism. Once it is known the device to be analyzed, it is possible to determine the best strategy to achieve the highest sensitivity by simply choosing the appropriate light source in terms of spatial

coherence, wavelength and polarization, and by choosing the adequate optical objective to maximize the effect of the numerical aperture.

4.4 Brownian Motion Measurement of a Suspended Membrane with an Interferometric Setup

Mechanical detection of the suspended membranes was performed with a custom-built interferometric setup, schematically represented in Figure 4.9.

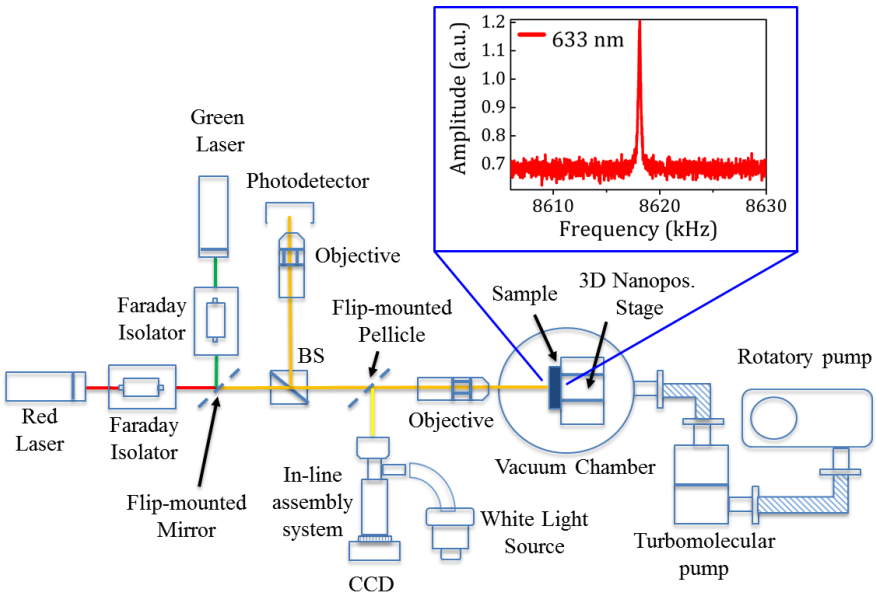

Figure 4.9 Schematic drawing of the custom-built interferometric setup used for the mechanical characterization of silicon nitride membranes. (Inset) Thermal spectrum of the fundamental vibration mode (0,1), obtained with the red laser (633 nm).

The optical setup is able to detect with two different lasers in the visible range: a red laser (5 mW, 632.8 nm, Thorlabs, Inc.) and a green laser (3 mW, 543 nm, Edmund Optics Ltd.). The laser beam is focused on the sample by a 50X objective (Mitutoyo, *NA* 0.55) that allows obtaining a spot size of about 2

μm. Light reflected from the sample is then collected with a silicon amplified photodetector (Thorlabs, Inc.). The sample is held into a vacuum chamber that achieves vacuum conditions up to 10^{-7} mbar by mounting in series a rotatory and turbomolecular pump (Varian, Inc.). In order to avoid eventual backscattering reflections that could damage the laser, a Faraday isolator cell was introduced along the optical path. A collimated LED white source is used to image the laser position on top of the sample with a CCD camera. The sample position is controlled by a three-dimensional nanopositioning stage (Attocube Systems, AG).

As previously described in Section 4.3, the displacement sensitivity is highly dependent on the light wavelength and notable differences should be observed between the green and the red laser (see the black dotted lines in Figure 4.8*b* and 4.8*d*). In fact, the green and the red laser are close to a minimum and a maximum of the displacement sensitivity, respectively, showing a difference that is almost one order of magnitude. Preliminary measurements performed with the green laser confirmed the theoretical calculations; any membrane displacement was measured with the green laser not even using optical objectives with different numerical apertures. For this reason, the following discussion will be focused entirely on the mechanical characterization with the red laser. The inset of Figure 4.9 shows a typical thermal spectrum of the fundamental mode $f_{0,1}$ of the membrane obtained with the red laser (633 nm), revealing a quality factor of about $\cong$ 57000. Since the mechanical detection with the red laser is higher for low numerical aperture, measurements were carried out by illuminating only the inner part of the optical pupil of the 50X objective; this experimental configuration guarantees an effective numerical aperture of about 0.1.

Experimental shapes of the membrane vibration modes were obtained by mapping the thermal amplitude of the vibration along the surface of the suspended membrane. In Figure 4.10 the experimental shapes and the FEM simulations of six different vibrational modes are reported. The experimental

shapes were obtained by changing the relative position between the sample and the laser with the nanopositioning stage and by measuring for each position the maximum of the thermal amplitude for each vibration mode. The software of data acquisition allows the measurement of three different vibration modes simultaneously. The measurement time of an entire spatial mapping depends on the spatial resolution selected; for a spatial mapping with a lateral step of 0.1 μm, the membrane of the entire membrane surface lasts about 2 hours. The mode number (n, m) can be recognized by counting the number of azimuthal and radial nodal lines respectively. FEM simulations performed with Comsol® were obtained by performing an eigenfrequency analysis of a clamped plate previously deformed by a tensile stress of 927 MPa (Section 4.2.2). Moreover, the true geometrical shape of the device with the etch release holes was also taken into account in the calculations. The resonant frequencies calculated by FEM are in good agreement with the experimental results, showing an average discrepancy below 0.5%.

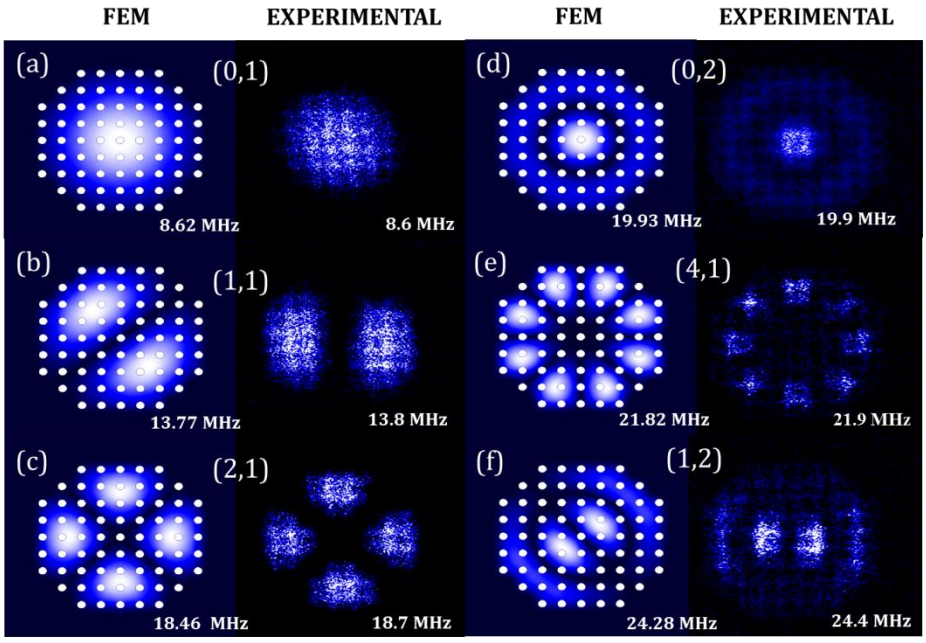

Figure 4.10. Comparison between the experimental shapes (right columns) of six vibration modes and the FEM simulations (left columns).

The spatial mapping of the vibration modes of a resonating structure were performed also in other works[44,79,193]; in particular Feng and co-workers[41,215] have recently mapped the Brownian motions of high-frequency silicon carbide micro-disk resonators. However, the accurate optimization of the interferometric detection mechanism as showed before guarantees the measurement of tiny thermal vibrations with higher signal to noise ratio and, thus, the possibility to observe interesting features in the spatial mapping. A direct demonstration of it can be observed by analyzing in more detail the spatial profile of the fundamental vibration mode. In Figure 4.11*a* it is shown the spatial profile of the vibration amplitude measured along a spatial region without holes (black dashed line in the top inset).

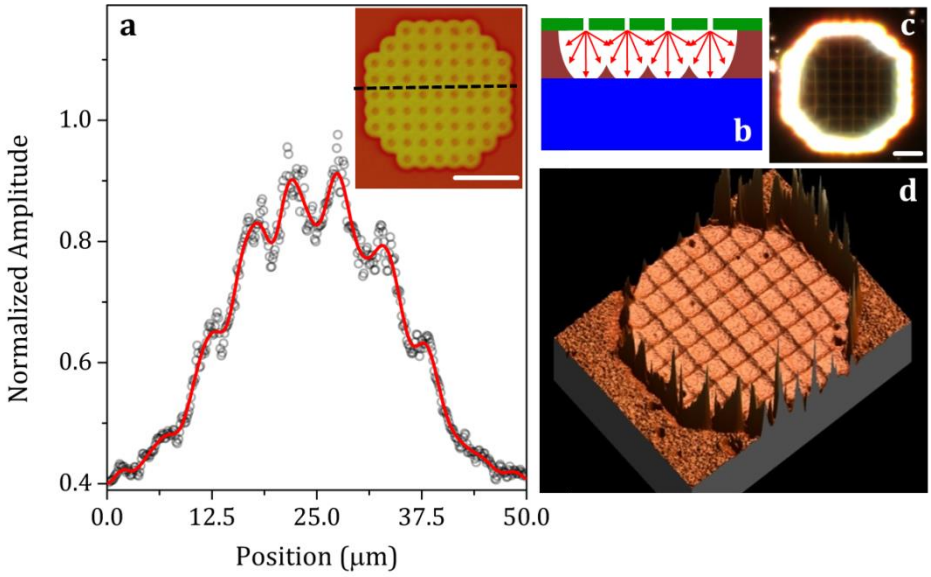

Figure 4.11. (*a*) Spatial profile of the fundamental resonant mode $f_{0,1}$ measured along the black dashed line shown in the top inset; the white scale bar in the inset corresponds to 20 μm. *b*) Schematic drawing of a suspended membrane subjected to the final etching process. *c*) 100X dark-field optical image of a hollow obtained after the peeling of the suspended membrane; the white scale bar corresponds to 10 μm. *d*) Surface topography of a hollow produced after the exfoliation of the suspended membrane. Experiments were carried out with a commercial white light interferometer (Veeco).

The overall spatial profile is given by the convolution of the fundamental vibration mode with a periodical signal whose spatial periodicity is equal to the holes distance (≅ 5 μm). This periodical signal is an experimental artifact produced by the presence of some nanofabrication defects of the device. The most plausible explanation is that the reflectivity modulation could arise by the presence of some oxide residues that were not fully etched from the underneath silicon substrate. In fact, as silicon oxide below the holes is etched faster than the oxide situated between the etch holes, this results in the formation of a square grid of silicon oxide (as depicted in Figure 4.11*b* for the sake of clarity).

In order to corroborate this hypothesis, the removal of the suspended membrane is needed. Previous attempts to remove the membrane with a focused ion beam (ionLiNE, Raith GmbH) were unsuccessful because the ion beam collapsed the membrane to the silicon substrate being unable to cut the suspended membrane. Conversely, the removal of the membrane was possible by exfoliating the membrane with a tape stripping process; a dark-field image of the resulting hollow obtained after the peeling of the membrane is shown in Figure 4.11*c*. Dark-field image points out a measurable signal scattering inside the hollow that has a square lattice shape. White light interferometry carried out with a commercial setup (Wyko NT9100, Veeco) confirmed the presence of etching oxide residues (Figure 4.11*d*) inside the optical cavity.

4.5 Conclusions

Optical interferometry represents one of the best choices for the achievement of ultra-high detection sensitivity of micro and nanomechanical resonators. Despite the very-high sensitivity that can be achieved by an interferometric detection scheme, several physical parameters can strongly affect its performance, such as the light wavelength, the numerical aperture of the objective, the light polarization and the degree of spatial coherence of the light source.

In this work a detailed study of the interferometric transduction mechanism was performed by considering as model the Brownian motion measurement of silicon nitride membranes suspended on a silicon substrate. After an accurate characterization of the suspended membranes, the theoretical displacement sensitivity of an interferometric setup was calculated by considering the influence of the wavelength, polarization, angle of incidence and spatial coherence of the detection light source. Therefore, suspended membranes were mechanically characterized by measuring the shape of six different vibration modes. The high signal to noise ratio here achieved after a careful optimization of the interferometric setup revealed the presence of small manufacturing defects generated during the nanofabrication process.

5. Detection Back-Action Effects on Ultrathin Bilayer Cantilevers

Nanomechanical resonators are getting increasingly smaller in order to achieve unprecedented detection limits in mass sensing[17,216-218], biological[13-21,81] and chemical sensing[9,13-21,82-84], and force spectroscopy measurements[67,79,80,195,197,219]. However, the use of minuscule resonators brings complexity to the design and optimization of the detection setup; by diminishing the dimensions of a resonator it is needed to take into account the influence of the detection back-action effect[23,25,68-70], which is usually negligible for commonly used mechanical resonators. Nevertheless, in the case of ultra-thin cantilevers this effect may be taken into account as the amount of energy interchanged during the detection process can significantly alter the mechanical state of the resonator.

In this chapter the detection back-action effects produced by a laser beam focused onto ultrathin bimetallic cantilevers will be presented. Experimental results followed by a careful theoretical analysis were used to understand the observed huge frequency resonance shift induced by the small optical absorption of the laser beam that modifies the temperature inside the bimetallic mechanical structure. The elucidation of this issue is fundamental in the development of applications based on nanomechanical resonators. In fact, the extraordinary fundamental detection limits promised by these tiny structures can be significantly impaired if the detection mechanism itself significantly

modifies the mechanical state of the resonator. Conversely, this drawback can turn into a relevant advantage in different applications consisting in active signal filtering[2,220,221], parametric amplification[222,223], self-excitation[70,224,225] and post-fabrication tuning of the mechanical properties[76,88]. Moreover, the found phenomenology is intimately connected to an old unsolved problem of the structural mechanics that is the effect of the out-of-plane deformation on the resonance frequency of singly clamped beams[63,75,226]. The results found in this study demonstrate a new mechanism responsible for the frequency resonance shift produced by the bending-induced deformation of the cantilever plate[69].

5.1 Methods

5.1.1 Characterization of Ultrathin Single-Clamped Cantilevers

Arrays of bilayers cantilevers consisting of a 50 nm thick low-stress silicon-rich silicon nitride and a 20 nm thick gold layer were fabricated in collaboration with Nanosens (Zutphen, The Netherlands). Cantilevers have also an adhesion layer of 5 nm of Cr between gold and silicon nitride to promote the adhesion between the silicon nitride surface and the gold layer. The cantilevers are 30 μm long and 12 μm wide, each chip with dimensions of 3 mm by 1.7 mm contains four cantilever beams. Technical details about the nanofabrication process are described elsewhere[227]. SEM images of the ultrathin bimetallic cantilevers are shown in Figure 5.1. A careful analysis of the SEM images revealed the presence of $\simeq$ 2.5 μm long underetching membrane at the cantilever clamping, that is formed during the last etching step of the nanofabrication process[28].

The internal stresses accumulated inside the bilayer cantilevers during the nanofabrication process produce a bending-induced out-of-plane deformation of the mechanical structure[60,191]. Optical characterization performed with a commercial white light interferometer (Wyko NT9100, Veeco) revealed

a downward out-of-plane displacement of about 1 μm, as it is shown in the 3D color contour plot of Figure 5.2.

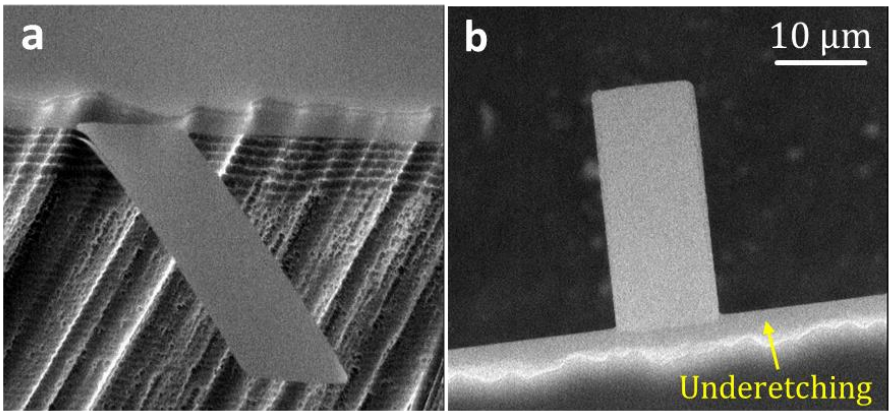

Figure 5.1 SEM images of ultrathin bimetallic cantilevers.

5.1.2 Design of the Custom-Built Laser Beam Deflection Setup

The high-sensitivity measurement of the thermal fluctuations of ultrathin small cantilevers is a demanding task, as it requires the measurement of tiny thermal movements with high signal to noise ratio[1,8]. This stringent requirement pushed the design from scratch of a custom-built laser beam deflection setup. The choice to measure the Brownian motion of cantilevers without external amplification is motivated by the fact that the main objective of this work is the study of the influence of the detection process and thus, is recommended to avoid the use of any external actuation scheme that could potentially alter the experimental results. As the cantilevers to be detected have a thermal noise[50] of $\simeq$ 2 pm/Hz$^{1/2}$, the measurement of cantilever thermal fluctuations requires the design of an experimental setup with a mechanical sensitivity higher than 1 pm/Hz$^{1/2}$. This technical requirement demands the use of a segmented photodetector instead of a position sensitive detector (PSD). Despite their narrow linearity range, segmented photodiodes presents higher

sensitivity than standard PSDs, demonstrating to achieve sensitivity[228-230] up to 5 fm/Hz$^{1/2}$. Moreover, as the fine control of the laser intensity is crucial for this experiment, a laser with high power stability was used.

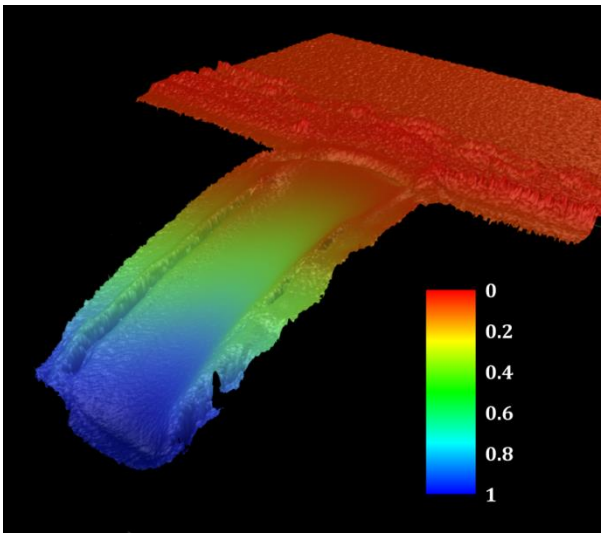

Figure 5.2. 3D color contour plot of the cantilever out-of-plane displacement measured with white light interferometry. The color bar represents the cantilever deflection in micrometers.

A schematic drawing of the custom-built laser beam deflection setup is shown in Figure 5.3. The light beam from an intensity-modulated linearly-polarized laser diode (λ = 785 nm, CUBE 785-40C, Coherent) was directed to the cantilever surface at an incident angle ≃ 45° through an optical objective (20X M Plan Apo, Mitutoyo, *NA* 0.42), obtaining a spot size of about 3 μm. In this experimental configuration cantilevers are illuminated with S-polarized laser light during all the experimental characterization. The high-performance laser diode guarantees a power stability less than 1% within 8 hours. The light reflected off the cantilevers was collected by a second objective (10X M Plan Apo, Mitutoyo, *NA* 0.28) and then by a four-quadrant photodetector (S4349, Hamamatsu) able to detect both flexural and torsional movements of

cantilevers. The segment photocurrents were amplified by low-noise current to voltage preamplifiers and acquired by a high speed voltage digitizer connected to a PC. The collimated light of a halogen lamp is used to image with a color CCD camera (PL-A782, PixeLINK) both the cantilevers surface and the position of the focused laser spot. The optical and mechanical components of the experimental setup were mounted on an optical breadboard (B6090A, Thorlabs) that allows the drastic reduction of the external mechanical and acoustic noise produced by the surrounding environment.

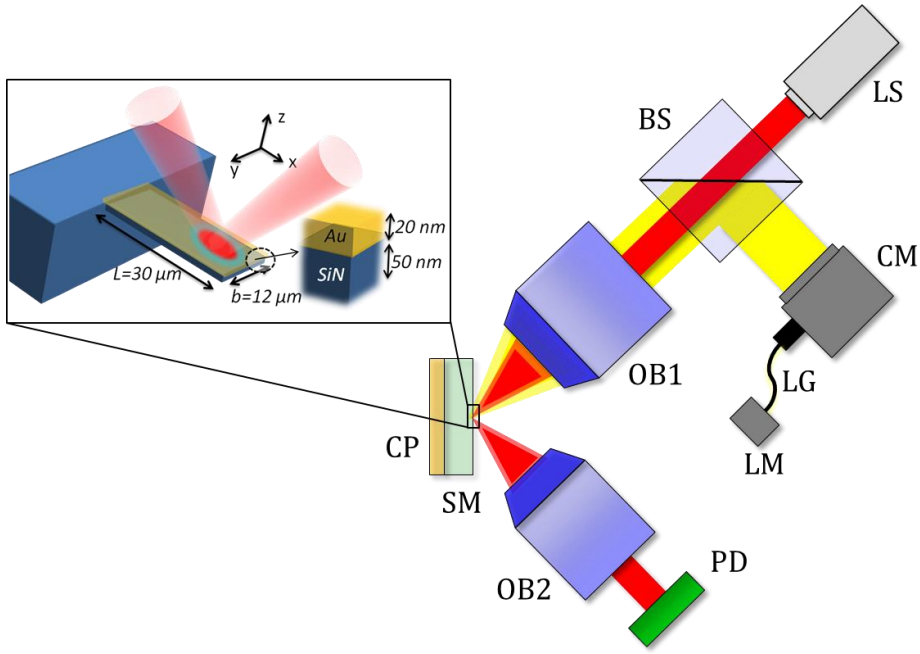

Figure 5.3 Schematic depiction of the laser beam deflection technique used to measure the cantilever deflection. The following component labels are used: LS, laser; BS, beam-splitter; CP, Peltier cell; OB1-OB2, microscope objectives; PD, photodetector; CM, CCD camera; LG, light guide; LM, lamp; SM, sample. The path of the laser (LS) is shown in red, while that of the camera light (CM) is shown in yellow. In the left inset, a schematic drawing of the bimetallic cantilever used for the experiments is shown.

Cantilevers chips were mounted onto a homemade sample holder, that allow the temperature control of cantilever by mounting a Peltier cell at its backside. The Peltier element itself was cooled with an external water-cooling loop passing water at ambient temperature. With this setup, the sample temperature can be controlled from 0 °C to 60 °C. The chip temperature is monitored by means of a thermocouple (K type, TC Direct) placed near the cantilever chip that allows the temperature control with an accuracy of ± 0.1°C.

The optimized alignment of the experimental setup requires a meticulous position control of all the mechanical and optical components, because the optimal conditions require that the focusing position of the laser beam and of the collimated white light coincide in the same position. This was achieved by mounting all the experimental components onto three-axis manual stages (MVN50 and UMR5.25, Newport) that guarantee the movements in X, Y and Z directions with micrometrical resolution. Moreover, as the two optical objectives required also of fine angle adjustments, they were mounted into two adjuster kinematic mounts (KM 100, Thorlabs) with micro-radiant angle precision.

Preliminary measurements performed with ultrathin cantilevers evidenced that the described custom-built detection setup reaches a sensitivity of about 500 fm/$Hz^{1/2}$, thus thermal measurements of the cantilevers can be performed with good signal to noise ratio. All the thermal spectral measurements were carried out in air environment.

5.1.3 Calibration of the Laser Optical Power

In order to accurately quantify the amount of energy interchanged during the detection process, the calibration of the power laser intensity is needed. The laser power can be changed by sending an additional voltage offset to the laser driver box. The calibration was obtained by mounting a calibrated photodiode (S120VC, Thorlabs) at the output of the 20X optical objective and

by measuring for different values of the applied voltage the corresponding laser optical power.

5.1.4 Calibration of the Cantilever Temperature

The cantilever temperature is experimentally controlled by placing a thermocouple sensor in contact to the chip. However, as the temperature sensor is not directly in contact to the cantilever, it is important to quantify the discrepancy between the temperature measured by the thermocouple and the temperature reached by the cantilever; this temperature difference could arise from the convective and radiation heat losses occurring at the outer surface of the whole chip. The temperature field of an entire chip placed in contact to a surface at a temperature T_0=293.15 K and surrounded by air at a temperature T_{air}=313.15 K was calculated through finite element analysis by taking into account both convective and radiation heat transfers with the surrounding environment[231]. The temperature difference between the chip and the surrounding environment was set to 20 K, because it represents the maximum temperature change achieved in the experiments and therefore where it is observed the maximum discrepancy. In Figure 5.4 is shown the temperature field of the cantilever chip numerically obtained with FEM (Comsol®). Numerical analysis calculated a maximum temperature discrepancy of $\simeq$ 0.05 K between the chip and the cantilever. This thermal discrepancy is negligible as it is below the temperature accuracy (0.1 K) of the thermocouple sensor used in the experiments; for this reason in the following discussion the cantilever temperature will be considered equal to the temperature measured by the thermocouple sensor placed onto the chip.

5.2 Experimental and Numerical Results

The experimental characterization of detection back-action effect was performed by measuring the first cantilever vibration modes of the ultrathin bilayer cantilevers. The experimental results discussed are based on experiments

carried out with eight cantilevers from three different chips. The thermomechanical spectrum shown in Figure 5.5 outlined that these ultrathin cantilevers have four different resonant peaks within the MHz range; the first and the third peak correspond respectively to the first and second flexural modes, while the second and the fourth belong to the first and second torsional modes. The insets shown in Figure 5.5 represent the cantilever mode shapes obtained with a numerical eigenfrequency analysis of the ultrathin bilayer resonator.

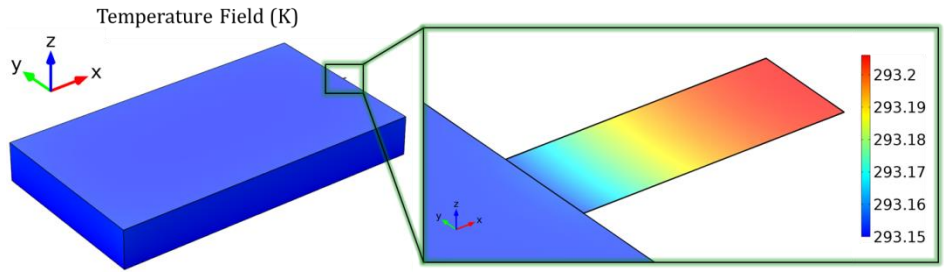

Figure 5.4. Temperature field of a cantilever chip numerically calculated with FEM; the color bar scale represents the temperature in K. Calculations were obtained by considering the geometrical dimensions and the material properties of the cantilever chips described in the Section 5.1.1. The bottom surface of the cantilever chip was fixed at the temperature =293.15 K, while the outer surfaces are surrounded by air at a temperature =313.15 K. Simulation was performed by considering a heat transfer coefficient between air and solids[231] of h = 25 W/(m^{2}K) and an emissivity coefficient = 1 for all the materials.

The study of detection back-action effect consisted on the measurement of the frequency resonance shifts of flexural and torsional modes produced by changing the optical power of the laser detection. Preliminary measurements on these cantilevers outlined that the best experimental condition was obtained by focusing the laser detection close to the cantilever clamping. Although cantilever thermal vibrations are more difficult to measure in this region, this choice is advisable for some important issues.

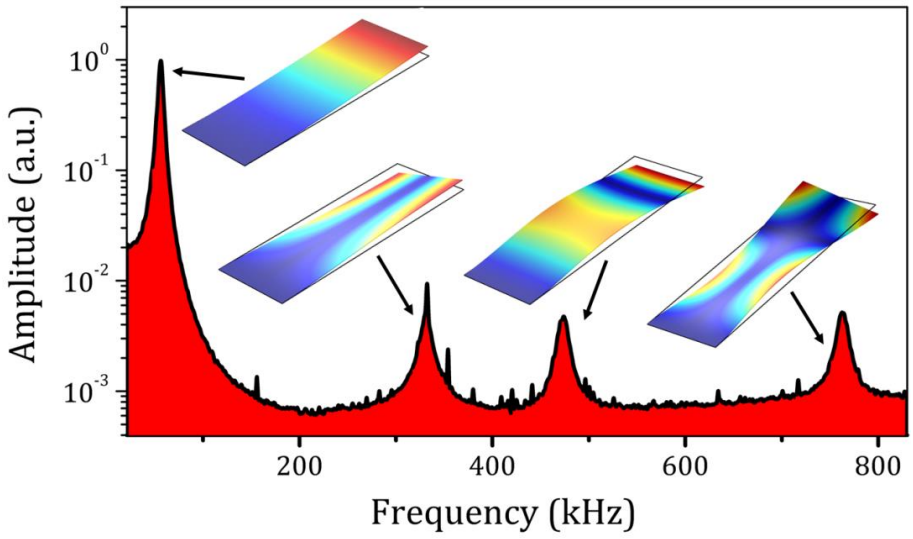

Figure 5.5. Frequency spectrum of the thermomechanical fluctuations of a cantilever. Beside each resonance peak is shown a schematic drawing of the vibration mode shape calculated by finite element simulations (Comsol®).

The optical power absorption in a bilayer cantilever produces a bending-induced deflection due to the difference in thermal expansion between the substrate and the coating layer, known in literature as photothermal effect[5,6,10,83,97,139,224,225,232-235]. When the laser optical power is changed, besides to induce a cantilever deflection also the focusing position of the laser is modified. The change of focusing position progressively increases by approaching the laser towards the cantilever free end, while it approaches to zero at the clamping. As a change of the laser position significantly modifies the temperature distribution inside the cantilever, a fine control of the laser position is needed and thus the laser focused at the clamping is a highly recommended choice. Moreover, by focusing the laser close to the anchor region ensures also that the angle of incidence of the laser beam is maintained constant during all the experimental characterization without any influence both on the optical power applied and on the focusing position of the laser. In addition, as the light used to image the sample could potentially alter the frequency resonances of the

cantilevers, the halogen lamp was turned off during the cantilever spectral measurements.

The essence of the detection back-action effect can be captured by measuring the dependence of the fourth vibration mode on the laser power intensity; this vibration mode was the most sensitive to the light power. Figure 5.6*a* shows how its frequency largely shifts to lower frequencies when the power of the laser used to probe the mechanical state of the cantilever is increased from 0.6 to 1.6 mW for a constant temperature of about 21 ^{0}C. The laser power increase of 1 mW gives rise to a decrease of the resonant frequency of about 35%.

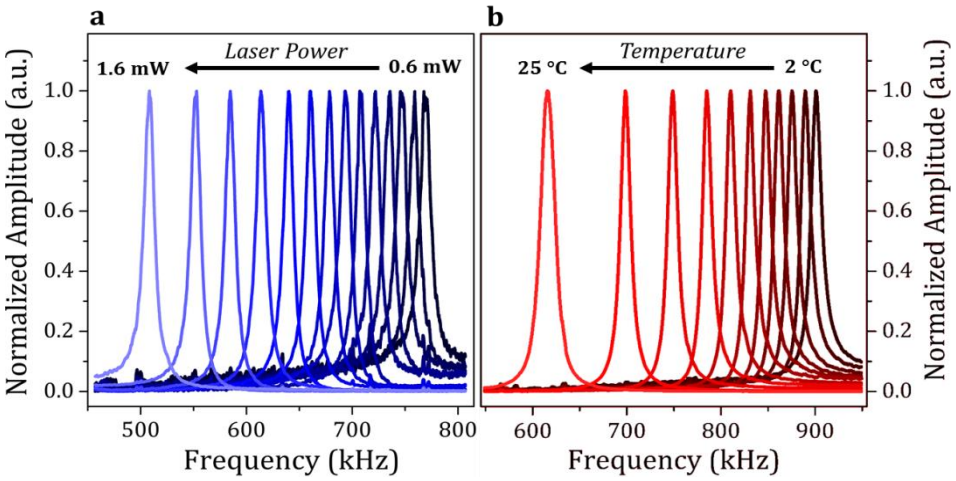

Figure 5.6 Evolution of the resonance peak of the fourth vibration mode as the laser power intensity used to measure the cantilever displacement is increased from 0.6 mW to 1.6 mW in even steps at a temperature of approximately 21 ºC (a), and as the temperature is increased from 2 ºC to 25 ºC in even steps at a laser power intensity of 850 μW (b). The laser beam is focused at approximately 6 μm from the clamping that is one fifth of the cantilever length.

To get insight into the origin of the huge laser-induced frequency shift, the resonant frequency of the fourth vibration mode was measured also by changing the cantilever temperature and by maintaining the laser optical power constant at 850 μW. The temperature dependence of the frequency resonance

(Figure 5.6*b*) evidences that a temperature increase of 23 ºC induces a downward frequency shift of about 30%.

The results suggest that the laser cantilever heating is the mechanism responsible of the downward frequency shift. However, in order to corroborate if laser power intensity measurements are compatible with a thermal mechanism, a quantitative estimation of the cantilever temperature distribution induced by a laser beam is needed. The absorbed optical power in this experimental study depends both on the wavelength and the polarization of the laser detection, on the optical absorption of the cantilever layers and on the incident angle between the incident beam and the cantilever[182]. The optical absorption of the S-polarized light[182] at the incident angle of 45º is approximately $\simeq 0.13$; this theoretical estimation was carried out by taking into account the dispersive optical properties of the cantilever layers[152,203]. Therefore, by applying the heat diffusion equation to a Gaussian heating source to mimic the experimental laser spot, the cantilever temperature distribution induced by an absorbed optical power was calculated.

Numerical simulations outlined that the 50 nm thick underetching membrane is key for the calculation of the cantilever temperature distribution and thus it was taken into account in the following FEM analysis. In fact, as the heat is poorly dissipated by air convection, the most contribution of heat loss arises from the heat that is flowing towards the chip. As silicon nitride is a good thermal insulator ($\simeq 20$ W $m^{-1}K^{-1}$), the ultrathin underetching membrane at the clamping represents a strong thermal barrier for the heat absorbed by the gold layer.

The numerical temperature field shown in Figure 5.7 was obtained by focusing the laser beam close to the clamping at one fifth of the cantilever length (6 μm from the clamping) and by considering 150 μW of optical power absorbed. Convective and radiative heat losses were neglected in the calculations, because they represent respectively at most the 0.5% and 0.15% of the total optical power pumped into the mechanical structure. The inset shown in Figure 5.7 is the cantilever temperature profile calculated along its

longitudinal axis. The induced temperature is uniform along the cantilever except near the clamping, where a temperature decrease of about 25% is observed. By comparing simulations with and without the underetching membrane it was found that the thin membrane at the clamping increases three times the cantilever temperature and smooths the temperature distribution in the mechanical structure. The average temperature increase in the cantilever is about 0.22 K per μW of optical power absorbed, resulting in good agreement with the experimental results previously shown (see Figure 5.6). This estimation evidences how the frequency shift produced by laser back-action is mediated by a thermal mechanism.

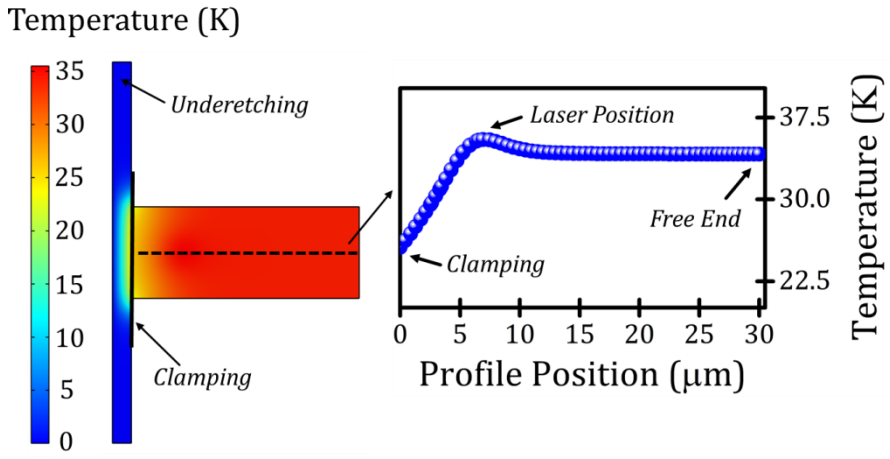

Figure 5.7 (Left) Two-dimensional color map of the temperature increase across the cantilever and the underetching membrane obtained with FEM analysis; the laser beam is placed near the clamping at one fifth of the cantilever length (6 μm from the clamping), the beam waist is 3 μm and the optical power absorbed is 150 μW. The color bar represents the temperature change in K. (Right) Spatial profile of the cantilever temperature increase calculated along its longitudinal axis. The X-axis origin is the cantilever clamping.

The frequency resonances and the relative frequency shifts of the first four vibration modes of a single micro plate as a function of the laser power are summarized in Figure 5.8. The uncertainty in both the laser spot position on the

cantilever and its spot size gives rise to an error in the frequency of 0.2 % that is smaller than the symbol size in Figure 5.8.

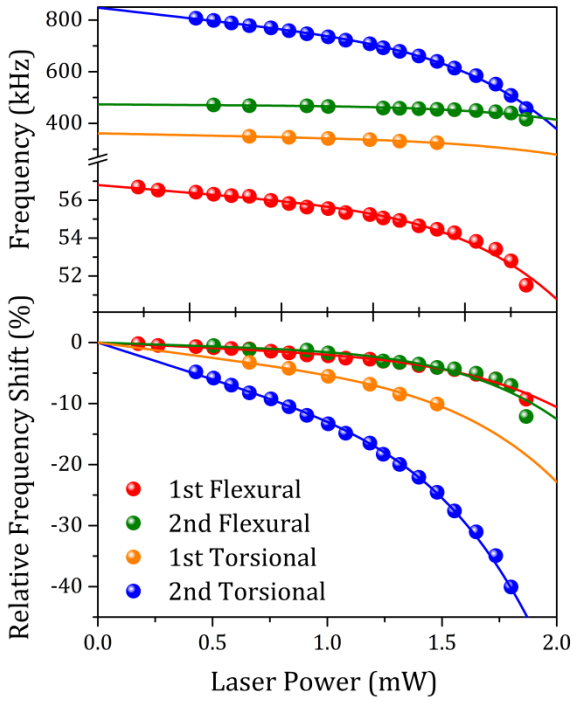

Figure 5.8 Frequency resonances of the first two flexural and torsional modes as a function of the laser power intensity; in (*a*) the frequency values are shown whereas in (b), the relative frequency shifts normalized to the extrapolated value at zero laser power intensity are reported. The temperature during the experiments was set to 21 ºC.

Interestingly, the resonant frequency shifts follow a non-linear behavior with the laser power. In addition, the relative frequency shift depends on the vibration mode index and on the kind of motion. The torsional modes, second and fourth vibration modes, are more sensitive to the laser power than the flexural modes (first and third mode). In this nanomechanical system, the second torsional mode is the mode that shows higher laser back-action effect. Its frequency is reduced 40 ± 10% by illuminating the cantilever with a power intensity of almost 2 mW (measurements in eight different cantilevers), reaching a state in which the third and fourth eigenmodes are close to being

degenerated in frequency. Thus, this extraordinary light-tuning of the eigenfrequencies can lead to singular situations in the dynamic response of these nanomechanical resonators such as the alteration in the frequency order of the vibration modes.

Most of the methods to tune the resonance frequency of nanomechanical resonators are based on controlling the stress of the beam by mechanical[76], electrical[236,237] and thermal effects[5,7]. In this work the thermal-induced optical absorption was used to control the stress of the beam. However, the most relevant difference is that the applicability of the aforementioned methods is limited to constrained structures such as doubly clamped beams where the stress cannot relax by expanding or contracting. In this case, the mechanical structure is an ultrathin microcantilever plate, and since the cantilever free end is unrestrained, most of the axial force along the beam can be relieved through the beam deformation[63,75,226]. So far, the only reported mechanisms that can modify the resonance frequencies on singly-clamped cantilevers within the framework of the linear elasticity are *i)* the temperature dependence of the geometrical dimension and of the elastic properties of the cantilever plate[71,238] and *ii*) the unreleased axial stress accumulated close to the anchor region[63,75,239].

The frequency resonance shift induced by a thermal change of the geometrical and elastic properties of a singly-clamped mechanical structure was analyzed in detail in several previous works[68,71,238,240]; by taking into account the thermal properties of silicon nitride and of the gold layers[240], this effect is about $\simeq -8\cdot10^{-5}$ for every degree of temperature increase. As this thermal effect is at least two orders of magnitude smaller than the effect observed in the present experiments, this thermal change will be considered negligible in the following discussion.

The effect of the unreleased axial stress at the cantilever clamping was studied by Lachut and Sader[75,226,239]. A simply-clamped cantilever plate subjected to an axial deformation results free to relax its stress in most of the mechanical structure due to the free boundary conditions at the edges and at the

cantilever free end. However, the boundary conditions imposed by the cantilever clamping restrict its movement and small residual stress is accumulated at its anchor region. This effect results particularly relevant for ultrathin cantilever plates and thus, a quantitative estimation of this effect is needed. As this effect was studied only for homogeneous cantilevers and for the first flexural mode, for a quantitative estimation a careful numerical analysis is needed.

In order to simplify the numerical modeling in the following discussion will be assumed a uniform temperature distribution along the whole cantilever plate. This assumption is well verified in this study as it was previously demonstrated that a laser beam focused close to the cantilever clamping induces a temperature distribution approximately uniform along the cantilever.

An isotropic bilayer cantilever beam subjected to a uniform temperature change suffers both an axial and an out-of-plane deformation given respectively by a biaxial in-plane force per unit width and a biaxial bending moment per unit width[241]

$$N_{\mathrm{th}} \cong \left(\frac{E_{\mathrm{s}}\alpha_{\mathrm{s}}h_{\mathrm{s}}}{1-\nu_{\mathrm{s}}} + \frac{E_{\mathrm{f}}\alpha_{\mathrm{f}}h_{\mathrm{f}}}{1-\nu_{\mathrm{f}}}\right)\Delta T \tag{5.1}$$

$$M_{\mathrm{th}} \cong \frac{E_{\mathrm{f}}h_{\mathrm{f}}h_{\mathrm{s}}(\alpha_{\mathrm{f}}-\alpha_{\mathrm{s}})}{2(1-\nu_{\mathrm{f}})}\Delta T \tag{5.2}$$

where E is the Young's modulus, ν is the Poisson's ratio, α is the thermal expansion coefficient, ΔT is the temperature variation, h is the layer thickness, and the subscripts s and f denote the substrate and the coating layer, respectively.

Since both in-plane and out-of-plane deformation can produce in principle a frequency resonance shift, in a standard bilayer cantilever is difficult to quantify the amount of each of the two effects. To isolate the effect of the axial deformation, numerical analysis was performed with ad-hoc tri-layer cantilever in which half of the gold layer is adhered to the bottom surface and the other half to the top (see Figure 5.9). In this symmetric tri-layer structure, the temperature does not induce a cantilever bending and the only effect that can shift the frequency resonances is the unreleased axial stress.

Numerical simulations consist in the eigenfrequencies calculation of the tri-layer cantilever, previously deformed by a uniform temperature change. In order to avoid long-time consuming simulations and to obtain accurate solutions, the meshing of the cantilever structure that has large aspect ratio was individually adapted to each direction, by using a customized free tetrahedral meshing. In addition, since the stress and strain near the clamping region play a critical role in the vibration response of the cantilevers, the clamping region was refined with an extremely-fine meshing. A convergence study was performed by refining the mesh element size until the relative error in the cantilever eigenfrequency was below 10^{-4}; this corresponds approximately to a mesh of $5 \cdot 10^5$ elements and $2.5 \cdot 10^6$ degrees of freedom.

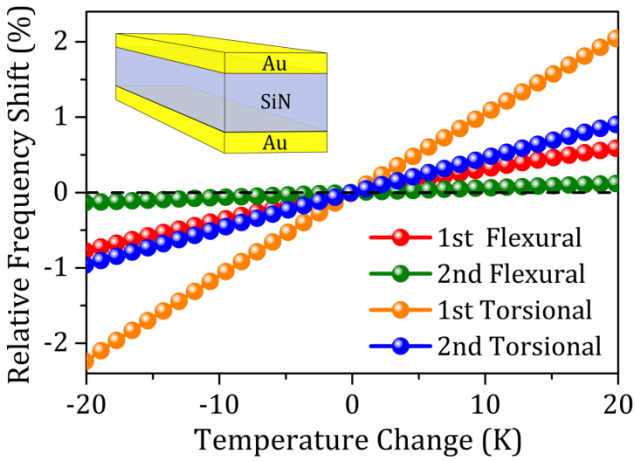

Figure 5.9 Finite element simulations of the percentage relative frequency shift of the first four vibration modes as a function of the temperature for a tri-layer cantilever consisting of 10 nm of Au, 50 nm of silicon nitride and 10 nm of Au.

The simulations show that the resonant frequencies linearly depend on the temperature and that the frequency shift is positive by increasing the temperature. Moreover, the relative frequency shifts ranging from $10^{-4}\ K^{-1}$ to $10^{-3}\ K^{-1}$ depending on the mode considered result about one order of magnitude smaller than the experimental results. Therefore, although the effect of

unreleased axial stress could be present in the experiments due to the axial deformation that is suffering a heated bilayer cantilever, it cannot explain the experimental results for the following reasons: *i*) the effect is linear with the temperature applied, *ii*) positive for increasing temperature and *iii*) at least one order of magnitude smaller than the found phenomenology.

By studying the frequency resonance shift on heated bilayer plates, it is possible to study the influence of bending moment on the resonance frequency of cantilevers. Although this classical problem of structural mechanics was debated during the last four decades, a consensus on the solution has not been achieved yet. Classical beam theory stated a negligible influence of the bending moment on the resonance frequency of cantilevers, arguing that within the framework of the linear elasticity is not possible to tune the frequency resonance of singly-clamped cantilevers with a bending deformation[226].

Surprisingly, numerical analysis on the ultrathin cantilevers unveiled that bending-induced deformation can modify the cantilever frequency resonance within the framework of the linear elasticity. In Figure 5.10 is shown the frequency resonance shift of the first four vibration modes of a bilayer cantilever, obtained by applying a uniform temperature change. Except for the first flexural mode when the temperature increases below 5 K, the resonant frequencies decrease for positive and negative variations of the temperature.
In the simulations the zero-temperature variation corresponds to the cantilever without thermal strain, i.e., null deflection. However, the cantilevers are bent downwards about 1 μm as a consequence of the nanofabrication process (see Figure 5.2) and therefore the initial state of the experimental cantilevers is represented by the vertical dashed line shown in Figure 5.10. Interestingly, if cantilevers were initially bent upwards (towards the Au) as a consequence of a different residual stress, the frequency shifts would be positive with the temperature. The theoretical frequency shifts for temperatures around this value are similar to those found experimentally and in consistency with the experiments. The torsional modes result more sensitive to the temperature. The main discrepancy between the theory and the experiments is found for the first

torsional mode that shows in the simulation a temperature sensitivity similar to the second torsional whereas in the experiments this sensitivity is significantly smaller (Figure 5.8). However, although it is found a good qualitative agreement, the numerical analysis does not intend to quantitatively match the experimental results. In fact, these discrepancies can be originated from many experimental uncertainties, such as the uncertainty on the initial plate deformation, the uncertainties both on the thicknesses and the elastic properties of the cantilever layers or the presence of the underetching membrane.

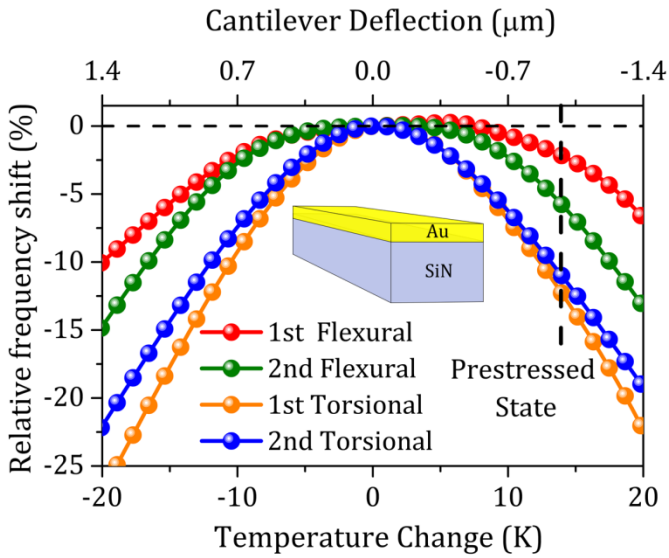

Figure 5.10 Finite element simulations of the relative frequency shifts of the first four vibration modes as a function of the cantilever temperature for a bilayer cantilever consisting of 20 nm of Au and 50 nm of silicon nitride. The top X-axis indicates the static deflection of the cantilever free end.

An interesting feature that can be observed in the frequency resonance shifts of a bilayer cantilever is the small asymmetry between the positive and the negative temperature changes. This asymmetry comes from the unreleased axial deformation occurring at the cantilever clamping that, as described previously (see Figure 5.9), is linear and positive by increasing the temperature.

The presence of this term explains the small positive frequency shift of the first flexural mode for temperature increase below 5 K. It is worth to notice that although both effects are always present in a heated bilayer structure, these two effects can be easily distinguished and uncoupled due to their different temperature dependence: the axial effect is odd whereas the cantilever bending effect is even.

The effect of bending deformation on the frequency resonances of a thin plate has been so far underestimated in the literature and the most accepted theoretical arguments claim that is not possible to produce any bending-induced frequency change in the framework of the linear elasticity. In Chapter 5 this novel mechanism will be detailed discussed and it will be shown that can be theoretically demonstrated by taking into account only linear elastic effects.

5.3 Conclusions

The use of smaller mechanical structures is crucial for ultrasensitive mass sensing[17,216-218], biological[13-21,81] and chemical sensing[9,13-21,82-84], and ultrasensitive force detectors[67,79,80,195,197,219], to name a few applications, because of the small active masses and high resonance frequencies. However, by shrinking their size dimensions, the mechanical state of a nanostructure can be sensitively influenced by the detection mechanism[23,25,68-70].

In this chapter was demonstrated that a laser beam commonly used for the static and dynamic cantilever detection significantly alters the frequency resonances of ultrathin singly-clamped cantilever plates[69]. The effect observed is also expected in several detection methods such as electrical, piezoresistive or magnetostrictive techniques that inherently generate internal stresses inside the mechanical structure. The measurement back-action imposes a limit in the accuracy of the measurement and it may prevent the achievement of the fundamental detection limits established so far. Therefore, when ultrathin cantilevers, nanowires or nanotubes are used, methods must be developed to

reconstruct the unperturbed mechanical state in order to achieve a highly sensitive and reliable measurement.

Conversely, this detriment can turn into a relevant advantage in applications consisting in active signal filtering[2,220,221], parametric amplification[222,223], self-excitation[70,224,225] and post-fabrication tuning of the mechanical properties[76,88].

Moreover, these experimental and numerical results shed light on the effect of the stress on singly-clamped cantilever plates. Thermal-induced stresses on bilayer cantilevers present two different effects responsible for the frequency resonance shifts: (*i*) the unreleased axial stress accumulated near the anchor region that is odd with the temperature change and (*ii*) the bending-induced deflection that is an even effect. The second effect, which has been traditionally disregarded, was revealed as the most important contribution in the case of ultrathin cantilevers. A thorough theoretical analysis on the effect of bending-induced deformation on the frequency resonance of ultrathin cantilever plates will be discussed in the following chapter.

6. Effect of the Bending Deformation on the Stiffness and the Resonance Frequencies of Cantilever Plates

Since 40 years ago a long debate has been carried out about the possibility to tune, within the framework of the linear elasticity, the resonance frequencies of a simply-clamped cantilever plate subjected to a small deformation[242,243]. Recently, Lachut and Sader demonstrated theoretically and considering only linear elastic effects that a thin cantilever plate subjected to a pure axial deformation can modify its resonance frequencies[75,226,239,244]. These theoretical predictions were then experimentally demonstrated by Karabalin *et al.*, in which they observed a frequency shift in cantilevers[63] by applying a pure axial deformation.

However, still today the effect of bending-induced deformation on the stiffness of a plate has received little attention by most of the scientific community, arguing that bending deformation is irrelevant to the stiffness change unless nonlinear elastic effects that typically occur for large cantilever deflections are considered. These theoretical arguments resulted contradictory when compared to the experimental results that were presented in Chapter 5, where it was shown how small bending deformation in ultrathin bilayer cantilevers can produce huge resonance frequency shifts. Moreover, numerical

analysis performed on these experiments confirmed how the found phenomenology can be well explained within the framework of the linear elasticity. This study demonstrated the potential relevance of bending deformation on the mechanical properties of thin cantilever plates. However, there is still a need for a rigorous theoretical approach of its physical mechanism. In this work it will be theoretically demonstrated that biaxial bending can significantly modify the stiffness and the resonance frequency of simply-clamped cantilever plates in the framework of the linear elasticity.

The main motivation that pushed the study of this intriguing problem is that bending effect can be observed in several natural processes, such as in plant leaves[72], insect wings[73], cell's membrane[74], to name a few. However, this ancient mechanism ubiquitously found in nature still remains unexplained in physics. A deep understanding of bending effect could be also extremely relevant in the field of nanotechnology and material science to engineer mechanical structures with reconfigurable stiffness and resonance frequency[76,245]. Bending deformation can be produced, in principle, by any kind of external stress distribution such as thermal effects induced by optical absorption or Joule heating effects[68,69,238], surface stress triggered by chemical or biological absorption[27] or by internal residual stresses accumulated during the fabrication process[60,246].

As bending effect results dramatically enhanced when the thickness of the structure is extremely smaller than its planar dimensions, this issue explains why bending effect resulted completely undetectable for most of the micro and nanomechanical structures developed so far in nanotechnology. However, during last years, many efforts have been focused on the development of atomically-thick mechanical structures[45], such as graphene and MoS_2 mechanical resonators, because their small active masses and high resonance frequencies ensure ultrasensitive mass sensing[41,216,247] and stiffness spectrometry[248] and unprecedented surface stress sensitivity[26,27,249]. Bending effect is expected to be extremely relevant for these latter mechanical structures

and thus, in order to accurately design and optimize these future devices, a thorough knowledge of the underlying physical mechanism is fundamental.

In the present chapter, it will be analyzed in detail the effect of bending deformation on the stiffness properties of ultrathin mechanical structures. After the development of a theoretical model valid for rectangular free plates in Section 6.1, clamping effects will be studied through a detailed numerical analysis in Section 6.2. The theoretical study will be then validated in 6.3 through an experiment performed with a macro aluminum plate. Finally, in Section 6.4, all the theoretical and experimental results will be summarized.

6.1 Analytical Theory of Rectangular Free Plate

According to the framework of standard plate theory, it is known that the stiffness of a plate subjected to bending deformation remains unchanged. This statement results in contradiction with the experimental evidence that a thin sheet is harder to deform when is subjected to bending in the transversal direction[250-253]. In the following paragraph two simple experiments performed with a plastic laminated A4 paper sheet are described in order to unveil three important properties of thin sheets.

In the first experiment, it is possible to observe that a thin sheet can be easily bent when it is deformed in only one direction, but this task cannot be easily achieved when the sheet has been previously deformed in the transversal direction (see Figure 6.1a). In this case the sheet, instead of deforming with a parabolic-like surface, exhibits a wrinkle pattern that impedes the bending deformation of the sheet. This simple experiment shows one first important property of thin sheets, internal stresses are developed when the sheet is subjected to bending along two in-plane axes.

A second experiment can be performed by simply fixing one of the ends of the sheet to a solid support (Figure 6.1b). The sheet is unable to mechanically sustain the gravity force and largely bends vertically. If a small downward

transversal curvature is added to the clamped sheet, the sheet bends due to the gravity, but substantially less than in the flat configuration. This experiment outlines a second property: the transversal bending induces bending stiffening in the longitudinal direction. Additionally, if the transversal curvature is oriented against the gravity, the sheet is even more rigid because the gravity force can barely bend it. Bending asymmetry is the third property of thin sheet, i.e. the bending stiffness is different when a plate is subjected to upward and downward transversal bending.

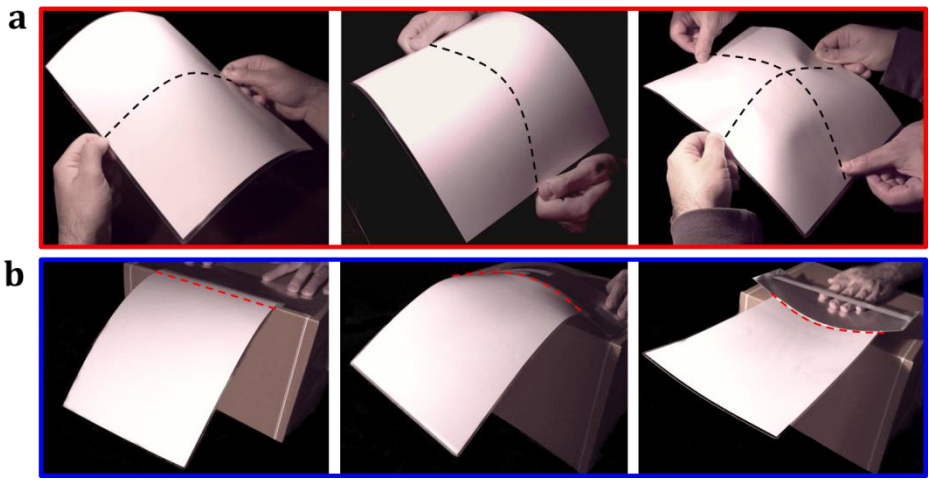

Figure 6.1. Two Experiments performed with a plastic laminated A4 sheet. (**a**) The sheet is easily bent transversally (left) or longitudinally (center) showing a parabolic-like shape. However, when the bending of the sheet is produced at the same time on both directions (right), it appears a wrinkle pattern that impedes the sheet deformation. (**b**) The bending of the sheet due to the gravity force depends critically on its transversal bending state. When there is no transversal bending (left) the sheet is unable to mechanically sustain gravity force and largely bends downwards. If a downward transversal bending is applied to the sheet (center) the deflection due to the gravity force is substantially less than in the flat configuration. Finally, if the transversal bending applied is upward (right) the sheet barely bends due to the strong increment of its stiffness.

The phenomenology found in the previous two experiments cannot be explained in the framework of standard plate theory in which it is stated that the stiffness of unrestrained plates subjected to bending deformation is independent of the out-of-plane displacement[254]. This statement is implicitly assuming that an isotropic, homogenous and unrestrained plate subjected to uniform biaxial bending will bend with constant curvature in the two axes without internal stresses[255,256]. It can be demonstrated through geometrical arguments that this statement leads to a paradoxical result.

In the present theoretical analysis it will be considered a thin sheet with length, width and thickness referred to as L, b and h, respectively (Figure 6.2). The original flat structure, subjected only to bending moments, will transform into a structure with out-of-plane displacement $w_s(x,y)$ that obeys the following three topological constraints; the volume, contour length and contour width must remain constant. For small displacements ($w_s(x,y) \ll L,b$), the constraints are mathematically expressed by applying Pythagorean theorem to infinitesimal lengths in the chosen Cartesian coordinate system,

$$bhL = \int_0^{L_x} \int_{-\frac{b_y}{2}}^{\frac{b_y}{2}} h_z dx dy \tag{6.1a}$$

$$L = \int_0^{L_x} \left\{1 + \tfrac{1}{2}(\partial_x w_s)^2\right\} dx \tag{6.1b}$$

$$b = \int_{-\frac{b_y}{2}}^{\frac{b_y}{2}} \left\{1 + \frac{1}{2}\left(\partial_y w_s\right)^2\right\} dy \tag{6.1c}$$

where L_x and b_y are the projections of the length and the width of the deformed sheet onto the x- and y- axes, respectively (Figure 6.2); and h_z is the thickness of the deformed sheet along the z- axis given by,

$$h_z = h\left\{1 + \frac{1}{2}(\partial_x w_s)^2 + \frac{1}{2}\left(\partial_y w_s\right)^2\right\} \tag{6.2}$$

Since, there are more equations than unknowns, L_x and b_y, the system of equations Eqns. (6.1a)-(6.1c) results overdetermined. This result can be clearly observed by substituting Eqns. (6.1b), (6.1c) and (6.2) into Eq. (6.1a), which results in the paradoxical equation,

$$(L_x - L)(b_y - b) = 0 \tag{6.3}$$

Since $L_x \leq L$ and $b_y \leq b$, equation (6.3) is only satisfied when the sheet is only bent in one direction as the dimension of the sheet in the orthogonal direction remains constant. Equation (6.3) implies that when a sheet is subjected to biaxial bending, internal stresses that modify the contour length of the sheet are necessarily generated, thus violating Eqns. (6.1b) and (6.1c).

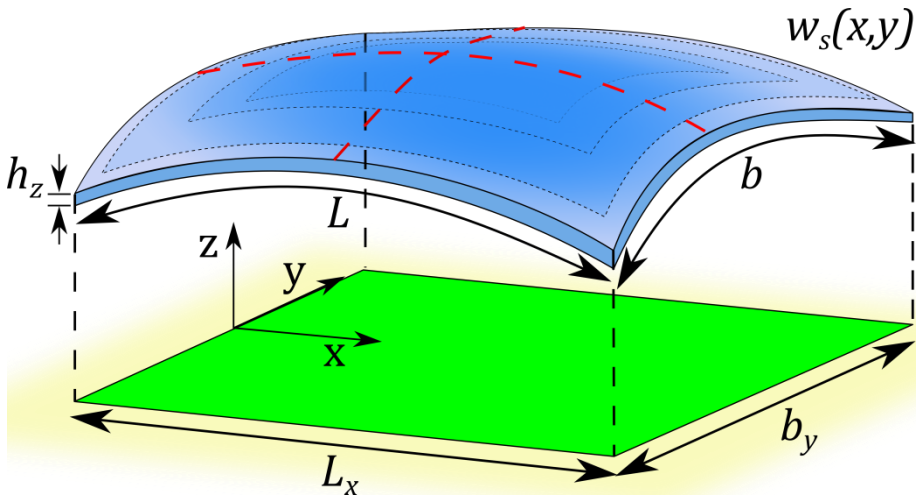

Figure 6.2. Schematic depiction of the bending of a free thin sheet. The original flat sheet with length, width and thickness given by L, b and h respectively is located on the $x-y$ plane and is afterwards bent with an out-of-plane displacement (z direction) given by $w_s(x,y)$. The projections of the length and the width of the deformed sheet onto the x- and y- axes are given by L_x and b_y respectively.

The calculus of the internal stresses generated in thin plates is a formidable theoretical challenge. As the straining energy scales[254] with $\sim\frac{h}{L}$ in

comparison to the bending energy that goes with $\sim \left(\frac{h}{L}\right)^3$, also small straining energy can induce three dimensional configurations such as buckling or wrinkling-like instabilities[250,251]. In order to circumvent the high complexity of the problem, in the following a thin sheet with an initial out-of-plane deformation given by $w_s(X,Y)$ will be considered. The energy cost associated to an additional small deformation $\Delta w(X,Y)$, where $X = \frac{x}{L}$ and $Y = \frac{y}{b}$, will be then calculated. In analogy with classical Kirchhoff-Love plate theory[254], the x and y in-plane displacements produced by $\Delta w(X,Y)$ are expanded as a power series along the z coordinate until the first order,

$$\Delta u(X,Y,z) = \Delta u_0(X,Y) - \partial_X \Delta w(X,Y)\left(\frac{z - w_s(X,Y)}{L}\right) \tag{6.4a}$$

$$\Delta v(X,Y,z) = \Delta v_0(X,Y) - \partial_Y \Delta w(X,Y)\left(\frac{z - w_s(X,Y)}{\beta L}\right) \tag{6.4b}$$

where $\beta \equiv \frac{b}{L}$; the main difference with standard Kirchoff-Love plate theory is that the neutral plane of the plate is now substituted by the curved surface $w_s(X,Y)$. By taking advantage of the symmetry of the problem, the functions $\Delta w(X,Y)$ and w_s are developed as power series in Y up to second order assuming that any bending in the transversal direction can be well approximated by a parabolic function,

$$w_s(X,Y) = a_x \widetilde{w}_{sx}(X) + \frac{1}{2} a_y \widetilde{w}_{sy}(X) Y^2 \beta^2 \tag{6.5a}$$

$$\Delta w(X,Y) = \Delta w_x(X) + \frac{1}{2} \Delta w_y(X) Y^2 \beta^2 \tag{6.5b}$$

where a_x and a_y are dimensionless parameters that account for the magnitude of the initial longitudinal and transversal deformations respectively. Although the present analysis has been focused to the symmetric case because it is the most common case found in nature, this general approach can be easily extended also to non-symmetrical cases. To the first order in a_x and a_y, the in-

plane displacements at the middle of the plate Δu_0 and Δv_0 compatible with the out-of-plane displacements proposed above are given by,

$$\begin{aligned}\Delta u_0(X,Y) = {} & (\Delta u_{00x}(X) + \Delta u_{02x}(X)Y^2\beta^2)a_x \\ & + \left(\Delta u_{00y}(X) + \Delta u_{02y}(X)Y^2\beta^2\right)a_y\end{aligned} \tag{6.6a}$$

$$\begin{aligned}\Delta v_0(X,Y) = {} & (\Delta v_{01x}(X)Y\beta + \Delta v_{03x}(X)Y^3\beta^3)a_x \\ & + \left(\Delta v_{01y}(X)Y\beta + \Delta v_{03y}(X)Y^3\beta^3\right)a_y\end{aligned} \tag{6.6b}$$

where $\Delta u_{00x}(X)$, $\Delta u_{02x}(X)$, $\Delta u_{00y}(X)$, $\Delta u_{02y}(X)$, $\Delta v_{01x}(X)$, $\Delta v_{03x}(X)$, $\Delta v_{01y}(X)$and $\Delta v_{03y}(X)$ are eight unknown functions that need to be determined. Importantly, the Euler-Bernoulli beam bending relations are recovered when the plate is initially flat ($a_x = 0$, $a_y = 0$).

The strain and stress components calculated in the limit of plane stress ($\sigma_{zz} = 0$) are given by,

$$\epsilon_{xx} = \frac{\partial_X \Delta u}{L} \qquad \epsilon_{yy} = \frac{\partial_Y \Delta v}{\beta L} \qquad \epsilon_{xy} = \frac{1}{2}\left(\frac{\partial_Y \Delta u}{\beta L} + \frac{\partial_X \Delta v}{L}\right)$$

$$\epsilon_{xz} = \frac{1}{2}\left(\partial_z \Delta u + \frac{\partial_X \Delta w}{L}\right) \qquad \epsilon_{yz} = \frac{1}{2}\left(\partial_z \Delta u + \frac{\partial_Y \Delta w}{\beta L}\right) \tag{6.7}$$

$$\sigma_{xx} = \frac{E}{1-\nu^2}\left(\epsilon_{xx} + \nu\epsilon_{yy}\right) \qquad \sigma_{yy} = \frac{E}{1-\nu^2}\left(\epsilon_{yy} + \nu\epsilon_{xx}\right) \qquad \sigma_{xy} = \frac{E}{1+\nu}\epsilon_{xy}$$

$$\sigma_{xz} = \frac{E}{1+\nu}\epsilon_{xz} \qquad \sigma_{yz} = \frac{E}{1+\nu}\epsilon_{yz} \tag{6.8}$$

where E is the Young modulus and ν is the Poisson's ratio; the components ϵ_{zz} and σ_{zz} in Equations (6.7) and (6.8) were omitted because in this case both of them are zero. The potential energy per unit length is defined by

$$U = \frac{1}{2}b \int_{-1/2}^{1/2} dY \int_{w_s(X,Y)-h/2}^{w_s(X,Y)+h/2} \left(\sigma_{xx}\epsilon_{xx} + 2\sigma_{xy}\epsilon_{xy} + 2\sigma_{xz}\epsilon_{xz}\right)dz \tag{6.9}$$

One should take into account that the limits of integration used do not consider the change of the cantilever geometrical dimensions produced by the static deformation $w_s(X,Y)$; these geometrical effects scale at least with h^3 and therefore can be considered negligible for this calculus.

The Euler-Lagrange equations associated to the strain energy U give a system of coupled differential equations for the 8 unknown functions whose solutions for $\beta \lesssim 0.5$ are given by,

$$\Delta u_{00x}{}'(X) \approx \frac{-24\Delta w_x{}'(X)\widetilde{w}_{sx}{}'(X) + \beta^2 \Delta w_y(X)\widetilde{w}_{sx}{}''(X)}{24L} \tag{6.10a}$$

$$\Delta u_{00y}{}'(X) \approx \frac{\beta^2 \Delta w_x{}''(X)\widetilde{w}_{sy}(X)}{24L} \tag{6.10b}$$

$$\Delta u_{02x}(X) \approx -\frac{\Delta w_y(X)\widetilde{w}_{sx}{}'(X)}{2L} \tag{6.10c}$$

$$\Delta u_{02y}(X) \approx -\frac{\Delta w_x{}'(X)\widetilde{w}_{sy}(X)}{2L} \tag{6.10d}$$

$$\Delta v_{01x}(X) \approx -\frac{\nu\beta^2 \Delta w_y(X)\widetilde{w}_{sx}{}''(X)}{24L} \tag{6.10e}$$

$$\Delta v_{01y}(X) \approx -\frac{\nu\beta^2 \Delta w_x{}''(X)\widetilde{w}_{sy}(X)}{24L} \tag{6.10f}$$

$$\Delta v_{03x}(X) \approx \frac{\nu\Delta w_y(X)\widetilde{w}_{sx}{}''(X)}{6L} \tag{6.10g}$$

$$\Delta v_{03y}(X) \approx \frac{\widetilde{w}_{sy}(X)\left(\nu\Delta w_x''(X) - 2\Delta w_y(X)\right)}{6L} \tag{6.10h}$$

The solutions described by Equations (6.10a)-(6.10h) have been found by considering also that the equilibrium of the forces at the cross section is zero, i.e.

$$\int_{w_s(X,Y)-\frac{h}{2}}^{w_s(X,Y)+\frac{h}{2}} \int_{-1/2}^{1/2} \sigma_{xx}\, dY dz = 0 \tag{6.11}$$

Once Equations (6.10) have been substituted into Equations (6.4)-(6.9) it is found that the strain energy can be split into two terms: the bending term U_b and the stretching term U_s given respectively by

$$U = U_b + U_s \tag{6.12a}$$

$$U_b = \frac{EL\beta\eta^3}{24(1-\nu^2)} \int_0^1 \{\Delta w_y(X)^2 + 2\nu \Delta w_y(X) \Delta w_x''(X) + \Delta w_x''(X)^2\} dX \tag{6.12b}$$

$$U_s = \frac{E\beta^5\eta}{1440L} \int_0^1 \left(w_{sx}''(X)\Delta w_y(X) + w_{sy}(X)\Delta w_x''(X)\right)^2 dX \tag{6.12c}$$

where $\eta = \frac{h}{L}$, $w_{sx}(X) = a_x \widetilde{w}_{sx}(X)$ and $w_{sy}(X) = a_y \widetilde{w}_{sy}(X)$. The bending energy described by Eq. (6.12b) is a well-known result in classical plate theory for plates with $\beta \lesssim 0.5$ and it results independent of the static deformation; in fact, in the case of a plate without deformation ($a_x = 0$, $a_y = 0$), the potential energy of the classical plate theory is recovered $U = U_b$, being zero the straining energy U_s.

In contrast, the straining energy U_s depends on the orthogonal coupling between the initial and subsequent deformations. The straining energy is zero when the sheet is only bent in one direction (e.g. $\Delta w_y = w_{sy} = 0$). This is in consistency with the topological constraints described by Equation (6.3), because uniaxial bending is compatible with zero straining of the neutral surface. If the sheet is initially bent in the transversal direction, nonzero stress of the neutral surface emerges when the bent sheet is subjected to longitudinal bending. These stresses are acting as a pulling force against the longitudinal bending, increasing the stiffness of the plate.

The relative change of stiffness $\Delta k/k$ and resonance frequency $\Delta f/f$ can be finally evaluated with the following equation,

$$\frac{\Delta k}{k} = 2\frac{\Delta f}{f} = \frac{U_s}{U_b}$$
$$= \frac{\beta^4(1-\nu^2)}{60\,\eta^2 L^2}\frac{\int_0^1 \left(w_{sx}''(X)\Delta w_y(X) + w_{sy}(X)\Delta w_x''(X)\right)^2 dX}{\int_0^1 \left\{\Delta w_y(X)^2 + 2\nu\Delta w_y(X)\Delta w_x''(X) + \Delta w_x''(X)^2\right\} dX} \tag{6.13}$$

It is remarkable that this theoretical approach is completely equivalent for both static or dynamic additional out-of-plane displacements Δw. In fact, the relative change of the kinetic energy that should be taken into account in the case of a dynamic displacement Δw has a leading term that scales with η^0 and, therefore, it can be considered negligible in this theoretical model.

For the sake of better clarity, it will be considered an initial deformation with constant curvatures κ_x and κ_y, i.e.

$$w_s(X,Y) = \frac{L^2}{2}\left(\kappa_x X^2 + \kappa_y Y^2 \beta^2\right) \tag{6.14}$$

and an additional out-of-plane displacements Δw that is a pure flexural deformation

$$\Delta w_y(X) = -\nu\,\Delta w_x''(X) \tag{6.15}$$

In this case the relative change of stiffness is now independent on the shape of the additional displacement of the plate and reads as,

$$\frac{\Delta k}{k} = \frac{L^2\beta^4}{60\,\eta^2}\left(\kappa_y - \nu\kappa_x\right)^2 \tag{6.16}$$

A glance at Equation (6.16) allows understanding the basic mechanisms of curvature-induced plate stiffening. The increase of the stiffness scales like$\sim\frac{\beta^4}{\eta^2}$. Thus, in the limit of very thin plates $\eta \ll 1$, small out-of-the plane deformations will give rise to very large stiffening. Furthermore, the quartic dependence on the parameter β indicates that this is purely a plate effect, as $\beta \to 0$ (beam limit) the effect quickly vanishes. Since the longitudinal curvature is multiplied by the

Poisson's ratio, the effect of an initial pure longitudinal bending that goes as $\sim\nu^2$ is significantly smaller than the transversal bending.

For instance the spring constant of a A4 paper sheet in the flat state is so small ($k \approx 0.0048\, N/m$), that it hardly sustains gravity force (Figure 6.1b). However, if we provide to the sheet a transversal curvature, the increase of spring constant is $\Delta k \approx 0.43\, {\theta_y}^2 (deg)\, N/m$, where θ_y is the angle described by the sheet in the transversal direction. By just slightly curving the sheet with $\theta_y \approx 2\, deg$, the sheet sustain gravity force with a deflection of 10% of its length.

Transversal curving seems to be the most economical way to stiffen a thin plate structure. This may be the case of plant leaves. It is well-known the leaf-shapes have been optimized during evolution to absorb sufficient light and facilitate gas exchange[72]. From this point of view leaves must be as wide, flat and thin as possible. However, leaf shape must also be optimized from the mechanical point of view; the leaf must support its own weight and external dynamic forces such as the pressure of winds[257]. Leaf curvature is genetically controlled and it can be modified at wish in some species by gene mutation[258]. The large influence of curvature on the stiffness of thin and wide sheets suggests that leaf curvature has been targeted by evolution for optimization of their biological and structural functions.

The effect of bending asymmetry observed with the paper sheet (Figure 6.1b) can be explained by the coupling term in Eq. (6.16), $\sim -\nu\kappa_x\kappa_y$. Bending asymmetry plays a key role in the flight of insects[73]. Detailed numerical simulations of insect wings have shown that chordwise camber of the insect wings induces significant wing stiffening and the coupling between chordwise and spanwise camber is the origin of the dorsal-ventral bending asymmetry. Here, we provide simple analytical equations that enable an intuitive understanding of this behavior.

In order to corroborate the validity of the analytical Equation (6.16), a detailed numerical analysis of free rectangular plates was performed. The numerical simulations were carried out following two sequential steps: *i*) the plate static deformation is calculated by applying anisotropic differential surface stress in order to independently control the longitudinal and transversal curvatures of the plate[256]; *ii*) the statically deformed structure is imported and an eigenfrequency analysis is performed. Notice that the plate deformation in a flexural vibration mode fulfils the relation $\Delta\kappa_y(X) \approx -\nu\Delta\kappa_x(X)$ assumed in the derivation of Equation (6.16). The relation between the resonance frequency shift and the relative stiffness change is given by $\frac{\Delta k}{k} = 2\frac{\Delta f}{f}$. Free plate conditions were obtained by applying *i*) at the plane $Y = 0$, zero displacement along the Y axis ($v = 0$), *ii*) at the clamping plane $X = 0$, zero displacement along the X axis ($u = 0$) and *iii*) at the point ($x = 0\,, y = 0, z = 0$), zero displacement along the Z axis ($w = 0$). These three boundary conditions restrict the translation and rotation of the plate, but enable free deformation without clamping restrictions.

Numerical simulations were performed by sweeping the following parameters: *i*) the curvatures κ_x and κ_y were varied from $-4\frac{h}{L^2}$ to $+4\frac{h}{L^2}$, *ii*) $\eta = h/L$ was varied from 50 to 300, *iii*) $\beta = b/L$ was varied from 0.03 to 0.4 and *iv*) Poisson's ratio ν was varied from 0 to 0.45. The total amount of numerical simulations is $\sim 10^5$. For each simulation a free tetrahedral meshing was applied and a convergence study was performed by refining the mesh element size until the relative error in the plate eigenfrequency is below 10^{-7}. The average number of degrees of freedom in the simulations was $\sim 10^6$.

Figure 6.3 plots the comparison between the analytical theory and the FEM simulations of the dimensionless coefficient $\zeta \equiv \frac{\frac{\Delta f}{f}}{(\kappa L)^2} = \frac{1}{120}\frac{\beta^4}{\eta^2}(1-\nu)^2$ that gives the ratio between the fractional frequency change and the normalized curvature. The comparison is performed for several values of β, η and ν, and for the case $\kappa_x = \kappa_y = \kappa$.

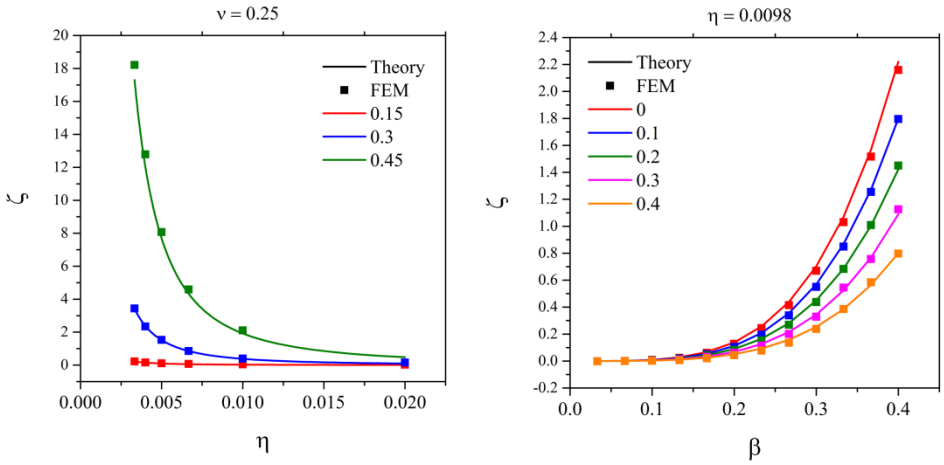

Figure 6.3. Comparison between the theory (lines) and the FEM data (symbols) of the coefficient ζ for a free plate in the case $\kappa_x = \kappa_y = \kappa$. The values of β, η and ν are specified in the graphs.

The comparison between theory and numerical analysis shows that the Equation (6.16) has an average accuracy below 10% for free plates in the range of the swept parameters.

6.2 Numerical Analysis of Clamping Effects

The theoretical framework developed in Section 6.1 was deduced for plates with all the edges free. However, it is common in nature and engineering to find these structures with one of the edges clamped to a substrate. In this case the region near the clamped edge cannot deform because of the reaction force of the clamping. Clamping effects dramatically increase the complexity of the problem, because still today they cannot be treated analytically. For this reason, in order to accurately calculate the stiffness of a singly-clamped plate, a numerical analysis is needed. Moreover, as clamping effects produces stiffness variations that depend on the specific out-of-plane displacement Δw considered, the present analysis will be restricted only to the dynamic study of the fundamental flexural mode.

Preliminary numerical analysis performed on clamped plates revealed that the anchor region modifies the stiffening of a plate through two different mechanisms: *i*) a clamping-induced geometrical effect that restricts the geometrical deformation of the plate at the anchor region, *ii*) clamping-induced residual stress effect that is produced by the accumulation of residual stress at the clamping. Each of these two effects will be discussed in detail in the following numerical analysis.

Clamping-induced geometrical effect was studied by following the same numerical procedure used for free plate (see Section 6.2). Clamping restrictions are set in the numerical analysis by imposing at the plane $X = 0$ a zero-displacement in the three directions ($u = 0, v = 0, w = 0$).

As it is well known that the transversal curvature in clamped plates decays exponentially to zero with a characteristics length of the order of the plate width[259], it was proposed the following correction to Equation (6.16) for taking into account of clamping-induced geometrical effect,

$$\frac{\Delta f}{f} = \frac{1}{2}\frac{\Delta k}{k} = \frac{1}{2}\frac{U_s}{U_b} = \frac{L^2}{120}\frac{\beta^4}{\eta^2} e^{-c\beta}\left(\kappa_y - \nu\kappa_x\right)^2 \qquad (6.17)$$

where the constant c was found numerically. Numerical fittings, performed on about 12k simulations with a coefficient R^2 always higher than 0.999, calculate a constant value of $c = 3.095 \pm 0.010$. A comparison between the theory described by Equation (6.17) and FEM simulations is shown in Figure 6.4, where the dimensionless coefficient ζ previously defined in Section 6.1 is plotted for different values of β, η and ν and for the case $\kappa_x = \kappa_y = \kappa$.

Equation (6.17) shows an average accuracy of about 10% when compared with FEM simulations for clamped plates with $\beta < 0.4$; a higher discrepancy can be observed only for Poisson's ratio higher than 0.4. Clamping-induced geometrical effect attenuates the stiffness tunability observed in free plate by a factor $e^{-c\beta}$, because a clamped plate is not able to deform as a free plate near the anchor region. Importantly, as it will be shown more in detail in

Section 6.3, clamping-induced geometrical effect is the only term to be considered when a free plate is previously deformed and subsequently clamped to a fixed support.

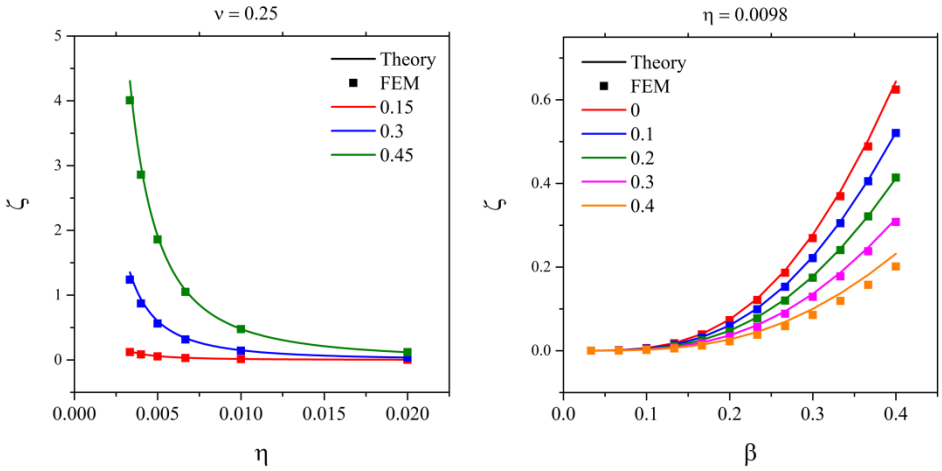

Figure 6.4. Comparison between the theory (lines) and the FEM data (symbols) of the coefficient ζ for a cantilever plate subjected to clamping-induced geometrical effect. The values of β, η and ν are specified in the graphs, while $\kappa_x = \kappa_y = \kappa$.

The second effect referred to as clamping-induced residual stress effect arises from the accumulation of in-plane stress near the clamping. This effect can be intuitively understood by considering a clamped plate subjected to an initial bending deformation; the initial stress cannot fully relieve near the anchor region due to the boundary conditions imposed by the clamping restrictions, and therefore residual stress will be stored inside the mechanical structure.

In order to isolate the residual stress term from the geometrical one, a three-step numerical analysis need to be performed. In the first step, the plate is statically deformed by applying anisotropic differential surface stress, in the analogous way described for the case of the study of the geometrical effect. In the second step, the plate recovers the flat configuration by applying a static deformation with opposite sign given by Stoney's formula. In this way the

cantilever plate does not present any geometrical deformation but at the same time residual stresses are stored near the clamping region. Finally in the third step, an eigenfrequency analysis of the plate subjected only to the residual stress is performed.

Numerical analysis revealed that clamping-induced residual stress gives rise to a significant plate softening, produced by a change of the bending asymmetry term $\sim \nu \kappa_x \kappa_y$. Clamping-induced residual stress effect results well-described by the following equation

$$\frac{\Delta k}{k} = -p(\nu)\frac{L^2}{60}\frac{\beta^4}{\eta^2} e^{-c\beta}\, \kappa_x \kappa_y \tag{6.18}$$

where $p(\nu) = 1.721\nu + 0.684\,\nu^2$ was found numerically by performing a numerical fitting on about 12k simulations with a coefficient R^2 always higher than 0.999. A comparison between the Equation (6.18) and FEM simulations is shown in Figure 6.5, where the dimensionless coefficient ζ is plot for different values of β, η and ν and for the case $\kappa_x = \kappa_y = \kappa$. Equation (6.18) shows an average accuracy of about 8% when compared with FEM simulations for clamped plates with $\beta < 0.4$. Interestingly, clamping-induced residual stress effect always produces a softening of the mechanical structure and it vanishes for zero Poisson's ratio. Moreover, as it will be shown in detail in Section 6.4, clamping-induced residual stress effect could be not present if the plate is deformed before being fixed to the clamping support; in this case in fact, no residual stresses are accumulated at the anchor region.

When both clamping effects are occurring, the stiffness change of a thin plate can be described by the following equation:

$$\frac{\Delta k}{k} = \frac{L^2}{60}\frac{\beta^4}{\eta^2} e^{-c\beta}\left\{\left(\kappa_y - \nu\kappa_x\right)^2 - p(\nu)\kappa_x\kappa_y\right\} \tag{6.19}$$

Equation (6.19) provides an easy way to engineer microcantilevers with reconfigurable stiffness and resonance frequency[245], because both stiffening and softening of a mechanical structure can be obtained.

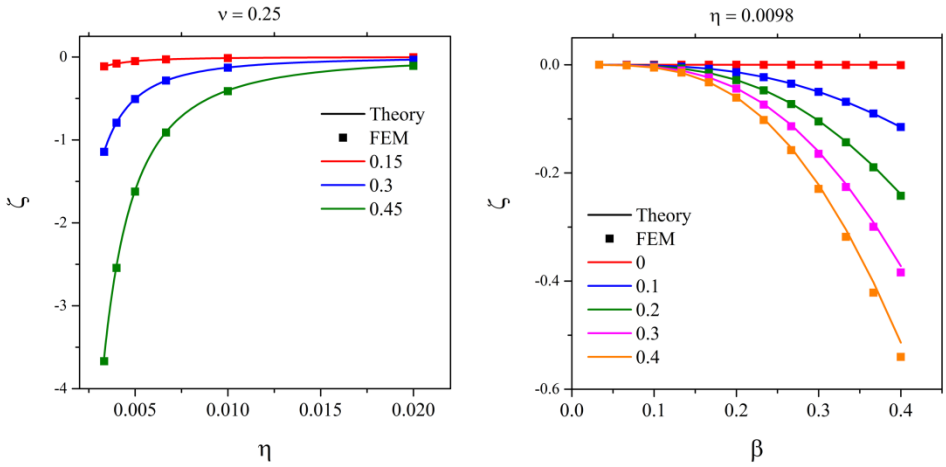

Figure 6.5. Comparison between the theory (lines) and the FEM data (symbols) of the coefficient ζ for a cantilever plate subjected to clamping-induced residual stress effect. The values of β, η and ν are specified in the graphs, while $\kappa_x = \kappa_y = \kappa$.

One of the most known methods used to induce bending in a cantilever is via stress confined in a thin layer on one of the surfaces of the microcantilever. Stress can arise from biochemical reactions[186,187,249], piezoelectric effect[63], bimetallic effect[232,233] or magnetostriction[219,260]. For uniform and isotropic surface stress, $\sigma_{sx} = \sigma_{sy} = \sigma_s$, and Equation (6.19) can be rewritten as,

$$\frac{\Delta k}{k} = \frac{3}{5}\frac{\beta^4}{\eta^6} e^{-c\beta}\{(1-\nu)^2 - p(\nu)\}\left(\frac{\sigma_s(1-\nu)}{EL}\right)^2, \tag{6.20}$$

where the relationship between the surface stress σ_s and the cantilever curvature κ is given by Stoney's formula, i.e. $\kappa = \frac{6(1-\nu)\sigma_s}{Eh^2}$. Examination of Eq. (6.20) reveals that there exists a critical Poisson's ratio, $\nu_c \approx 0.275$, for which the cantilever stiffness is independent of the surface stress. For $\nu > \nu_c$, surface

stress softens the cantilever and for $\nu < \nu_c$ the cantilever stiffens. For instance, the stiffness for a microcantilever 100 μm long, 30 μm wide, 100 nm thick, a Young modulus of 150 GPa and subjected to a surface stress of 1 N/m can be increased more than four times for $\nu = 0.1$ and decrease to the half for $\nu = 0.3$.

The theoretical results described by Equation (6.20) confirm and agree with the experimental results obtained in Chapter 5, where it was observed that ultrathin gold coated silicon nitride cantilevers presents a softening of their mechanical properties. The latter mechanical structures have an effective Poisson's ratio $\bar{\nu} \cong 0.3$ greater than the critical Poisson's ratio ν_c and therefore a softening of the mechanical properties is expected.

Interestingly, the theoretical analysis here described can be extended from nano to macroscopic dimensions without any loss of generality, because bending becomes relevant every time that the planar dimensions of the plate are much larger than its thickness. In the following section, it will be demonstrated that the found phenomenology can be observed also in a macroscopic aluminum plate.

6.3 Experimental Validation of Theory with a Macroscopic Plate

An easy experiment performed onto a home-built macroscopic aluminum plate allows the validation of the theoretical model developed in Sections 6.1 and 6.2. The aluminum macro-plate has planar dimensions $29 \times 10\ cm^2$ and a thickness of $645 \pm 20\ \mu m$. The plate was clamped to a fixed support and its transient vibration was recorded by a smartphone camera (Apple 6S Inc., 240 frames per second). The transient vibration is obtained by manually applying a step force to the cantilever free end (Figure 6.6a), while the analysis of the transient vibration was performed with a custom routine developed with Matlab that tracks the position of the red label adhesive placed at the cantilever free end (Figure 6.6b). The resonance frequency curve is

obtained by calculating the Fast Fourier transform of the transient oscillation and the resonance frequency is determined by fitting the resonance peak to the damped harmonic oscillator equation.

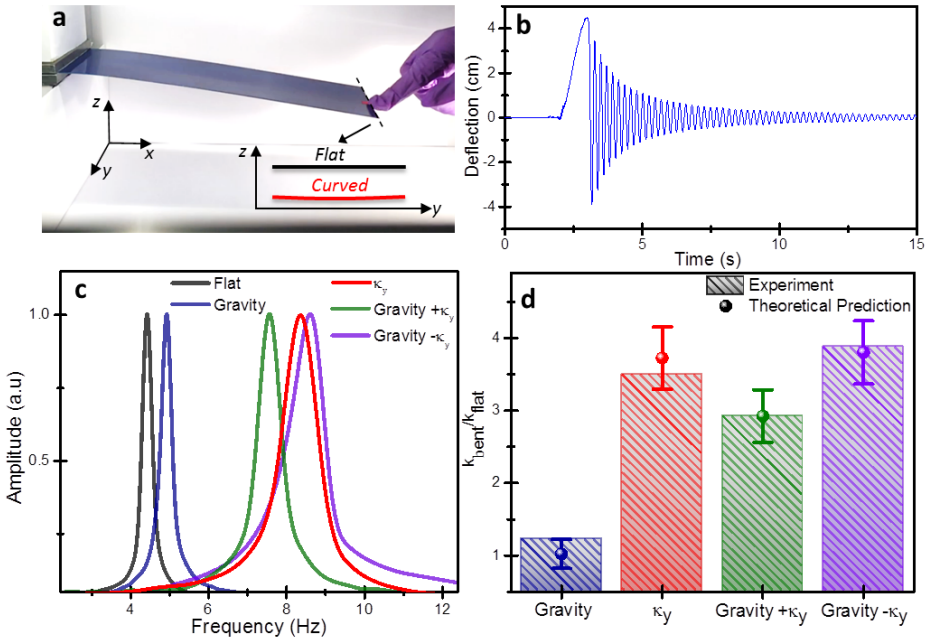

Figure 6 . 6 Experiment with an Aluminum Macro-Plate

Figure 6.6 (**a**) Photograph of the macroscopic cantilever plate. The dimensions of the cantilever are $29 \times 10 \times 0.0645\ cm^3$. The cantilever was set into oscillation by manually applying a step force at the cantilever free end. The inset shows the profile of the free end in *yz* plane in the flat and curved configurations with the same aspect ratio than in the experiments. (**b**) Transient oscillation of the microcantilever plate. (**c**) Frequency response of the cantilever at the different curvature configurations; gravity label stands for a cantilever subjected also to the bending-induced longitudinal curvature κ_x. (**d**) Comparison between theory and experiment of the ratio between the stiffness of the bent cantilever and the flat cantilever at vertical position.

Dynamical characterization of the macro-plate was performed in five different experimental configurations:

i) *flat* configuration: the plate does not present any initial longitudinal and transversal curvatures. This configuration is achieved by orienting the cantilever vertically, i.e. the plate longitudinal axis is parallel to the gravity force.

ii) κ_x configuration: the plate is subjected to an initial longitudinal curvature given by the gravity force. This configuration is obtained by orienting the cantilever plate horizontally, i.e. the plane of the plate is orthogonal to the gravity force. A plate subjected to gravity present a non-constant longitudinal curvature given by $\kappa_x(X) \approx \frac{4w_L}{L^2}(X-1)^2$, where w_L is the deflection of the free end[254]. The deflection w_L in the present configuration was $w_L = (2.0 \pm 0.1)\ cm$.

iii) κ_y configuration: the plate presents only an initial transversal curvature. A permanent transversal curvature was achieved by pressing the plate against a cylindrical metallic piece and subsequently fixing one of the ends to a fixed support. The transversal curvature was determined by a caliper at the free end, obtaining $\kappa_y = 1.15 \pm 0.05\ m^{-1}$. Moreover, the plate is not subjected to initial longitudinal curvature because the plate is vertically oriented.

iv) $\kappa_x + \kappa_y$: the plate is subjected both to initial longitudinal and transversal curvature and the two curvatures have the same sign. This was achieved by orienting the deformed plate horizontally with the transversal curvature inward the gravity. The experimental longitudinal deflection in this experiment was $w_L = (1.4 \pm 0.1)\ cm$.

v) $\kappa_x - \kappa_y$: the plate is subjected both to initial longitudinal and transversal curvature and the two curvatures have opposite sign. This was achieved by orienting the deformed plate horizontally with the transversal curvature outward the gravity. The experimental

longitudinal deflection in this experiment was $w_L = (0.2 \pm 0.1)\ cm$.

Figure 6.6c summarizes the values of the resonance frequency for different curvature configurations. The *flat* configuration shows the lowest resonance frequency of about $4.4\ Hz$, while at the κ_x configuration the resonance frequency slightly increases to $4.9\ Hz$, due to the gravity-induced longitudinal curvature. However, when a small permanent transversal curvature is applied ($\kappa_y = 1.15\ m^{-1}$), a huge increase of the resonance frequency is observed. The plate at κ_y configuration largely increases the frequency up to $8.4\ Hz$, evidencing the fundamental role of the transversal curvature in the stiffness of thin plates. The bending asymmetry effect is clearly evident by making a comparison between $\kappa_x + \kappa_y$ and $\kappa_x - \kappa_y$ configurations; in the first case, the resonance frequency decreases $0.7\ Hz$ with respect to κ_y configuration, whereas, in the second case the resonance frequency increases $0.3\ Hz$.

In order to quantitatively compare these results with the theory, the theoretical model must consider the case in which the static curvatures are not uniform as it is the case of gravity-induced bending. The equation (6.13) then transforms into

$$\frac{\Delta f}{f} = \frac{L^2}{120}\frac{\beta^4}{\eta^2} e^{-c\beta} \frac{\int_0^1 \left(\kappa_y - \nu\kappa_x(X)\right)^2 \psi''(X)^2 dX}{\int_0^1 \psi''(X)^2 dX} \qquad (6.21)$$

where $\psi(X)$ is the eigenmode shape of the fundamental mode obtained by the Euler-Bernoulli beam theory[50], and the exponential term accounts for the clamping restriction; the Poisson's ratio for the aluminum has been set to 0.35. As shown in Figure 6.6d, the comparison between theory and experiment shows a very good agreement.

The two main sources of error of the theoretical predictions in Figure 6.6d arise mainly from the uncertainties in the measurements of the curvature κ_y and the plate thickness h.

6.4 Conclusions

In this work, it was studied the influence of the biaxial bending on the stiffness of a cantilever plate. A rigorous theoretical approach demonstrates how a small amount of a two-dimensional bending in thin plates leads to the development of in-plane stresses that hugely modifies the plate stiffness. For free plates, biaxial bending always induces a plate stiffening. However, when a plate is clamped to a fixed support, the clamped edge cannot deform due to the clamping restrictions. The anchor region modifies the plate stiffness through two different mechanisms: *i*) a clamping-induced geometrical effect that limits the geometrical deformation of the plate at the anchor region and *ii*) a clamping-induced residual stress effect, produced by the accumulation of residual stress at the clamping, that softens the mechanical structure.

Biaxial curving of thin sheets is perhaps the most efficient way to engineer microcantilevers with reconfigurable stiffness and resonance frequency[245]. This ancient mechanism found in nature and in man-made structures has remained unexplained in physics[72-74,257,258]. The theoretical model and simple equations provided in this chapter solve this long-standing problem, shedding light in our understanding of thin sheet mechanics and bringing new and useful ideas to a wide variety of fields such as natural science, mechanical engineering and micro/nanotechnology[69,76,87-89].

7. General Conclusions

To conclude this dissertation, in this doctoral work I faced up some relevant open issues in nanotechnology related to the use of ultrathin nanomechanical resonators. In the following I will briefly summarize all the main achievements presented in the previous chapters.

The first part of my thesis was focused on the development of a new experimental technique, referred to as Spatially Multiplexed Micro-Spectrophotometry, able to perform the fast spectral analysis of large sample areas with sub-micrometrical spatial resolution. The main advantage of the SMMS technique compared to standard micro-spectrophotometry is that for each fixed wavelength, the spectral analysis is multiplexed in the spatial coordinates. This experimental configuration provides at least two orders of magnitude faster spectroscopic analysis than conventional micro-spectrophotometry, because the measurement of large sample areas, ranging from several hundreds of μm^2 up to few mm^2 combined with sub-micrometrical spatial accuracy can be performed in just few minutes. The capability of the SMMS technique was firstly demonstrated in dark-field mode by performing the polarization-resolved spectral analysis of hundreds of single and dimer nanoparticles (Chapter 2). The high signal-to-noise ratio measurements proved by the SMMS technique make now possible to observe the effect of the substrate on the plasmon resonances of individual nanoparticles by observing tiny changes both in the spectral measurements and in the spatial analysis of the

scattered light. In addition, the diameter of hundreds of individual nanoparticles can be rapidly assessed with 1 nm accuracy in just 2.5 minutes.

The SMMS technique was also proved in bright-field mode through the spectral analysis of an array of commercial silicon cantilevers (Chapter 3). This optical characterization was able to obtain thickness maps of an entire cantilever array (area $\simeq$ 0.4 mm^2) in 4 minutes and with 1 nm vertical accuracy and micrometrical spatial resolution. The technique allows the rapid inspection of tiny structural defects over the whole device, making possible to assess the mechanical variability of a device produced during the nanofabrication process.

The second part of my thesis was focused on the study of the displacement transduction mechanism for the detection of ultrathin mechanical structures. I focused on the analysis of two different topics: *i*) the analysis of the main physical parameters that influence an interferometric detection setup and *ii*) the study of light-induced detection back-action effects on ultrathin cantilevers. The first topic was examined by studying both theoretically and experimentally the transduction mechanism of an interferometric setup (Chapter 4). The interferometric sensitivity presents a strong dependence on the physical properties of the detection light source used, such as its wavelength, polarization, angle of incidence and spatial coherence. For this reason, in order to achieve the highest sensitivity, a careful optimization of the interferometric detection setup is required. The proposed methodology made possible the high-sensitivity measurement of thermal vibration modes of suspended ultra-thin silicon-nitride membranes. The second topic was accomplished by measuring the resonant frequency shifts in ultrathin bilayer cantilevers when illuminated by a focused laser beam (Chapter 5). This study outlines that light back-action effect is nonlinear with the optical power applied and that some resonant frequencies can be reduced almost to a half with laser power intensities of 2 mW. These results indicate that in order to achieve the ultimate detection limits with nanomechanical resonator, the uncertainty due to the detection back-action must be considered.

The found phenomenology shed light on a new physical mechanism previously misregarded in literature, that is, the role of the bending curvature on the stiffness of a singly-clamped cantilever within the framework of the linear elasticity theory. The last part of my thesis was focused on the study of this unexplored effect (Chapter 6). A detailed theoretical analysis based on topological arguments, demonstrates how a small amount of two-dimensional bending in thin plates leads to the onset of in-plane stresses that largely modify the plate stiffness. For free plates, biaxial bending always induces plate stiffening. However, when a plate is clamped to a fixed support, the clamped edge cannot deform due to the clamping restrictions and two different mechanism can produce stiffness change: *i*) a clamping-induced geometrical effect that impedes the geometrical deformation of the plate at the anchor region and *ii*) a clamping-induced residual stress effect that softens the mechanical structure. These theoretical results were also validated experimentally with a macro-aluminum plate, providing a solution to this long-standing problem and shedding light to our understanding in a wide variety of fields such as natural science, mechanical engineering and micro/nanotechnology.

Conclusiones

En este trabajo de tesis he estudiado algunos aspectos relevantes relacionados con el uso de resonadores nanomecánicos ultra-delgados. A continuación, se resumen brevemente los principales resultados presentados en los capítulos anteriores.

La primera parte de esta tesis se ha centrado en el desarrollo de una nueva técnica experimental, llamada micro-espectrofotometría multiplexada espacialmente (SMMS), capaz de realizar el análisis espectral de áreas muy extensas de una muestra con una resolución lateral sub-micrométrica. La principal ventaja de esta técnica comparada con la micro-espectrofotometría estándar es que para cada longitud de onda, el análisis espectral de una muestra se realiza simultáneamente en las coordenadas espaciales. Esta configuración experimental proporciona un análisis espectral al menos dos órdenes de magnitud más rápido que la micro-espectrofotometría convencional, debido a que se puede realizar la medición de superficies muy extensas del orden de mm^2 y con resolución lateral sub-micrométrica en sólo algunos minutos. Las principales características de la técnica SMMS se demostraron en primer lugar en campo oscuro, a través del análisis espectral resuelto en polarización de centenares de nanopartículas individuales (Capítulo 2). La elevada relación señal-ruido de la técnica SMMS hace ahora posible observar el efecto del sustrato sobre las resonancias de plasmón a partir del análisis espectral y espacial de la luz dispersada por cada nanoparticula individual. Además, con

esta técnica ha sido posible estimar rápidamente el diámetro de cientos de nanopartículas con una incertidumbre de 1 nm en tan sólo 2,5 minutos.

La técnica SMMS ha demostrado ser eficaz también en campo claro, a través del análisis espectral de un chip de palancas comerciales de silicio (Capítulo 3). Esta caracterización óptica hace posible obtener mapas de espesor con resolución lateral micrométrica de todo un chip de palancas (área $\simeq$ 0,4 mm^2) en solo 4 minutos y con una incertidumbre en el espesor de 1 nm. La técnica SMMS permite la rápida inspección de pequeños defectos estructurales a lo largo de todo el dispositivo y permite evaluar la variabilidad mecánica de un dispositivo debido al proceso de nanofabricación.

La segunda parte de la tesis se ha centrado en el estudio del mecanismo de transducción para la detección de resonadores nanomecánicos ultra-delgados. En particular, he estudiado dos aspectos diferentes: *i*) el análisis de los parámetros físicos más influyentes en la sensibilidad de un sistema de detección interferométrico y *ii*) el estudio de la influencia del proceso de detección en resonadores ultra-delgados. El primer aspecto se logró a partir de un detallado análisis experimental y teórico de la sensibilidad de un sistema óptico interferométrico (Capítulo 4). La sensibilidad interferométrica presenta una fuerte dependencia con las características de la fuente de luz utilizada, como su longitud de onda, polarización, ángulo de incidencia y coherencia espacial. Por esta razón, a fin de maximizar la sensibilidad, se requiere una optimización cuidadosa del sistema de transducción. La metodología propuesta hizo posible la medición ultra-sensible de los modos de vibración térmicos de membranas de nitruro de silicio ultra-delgadas. El segundo aspecto se llevó a cabo midiendo los cambios en las frecuencias de resonancia de palancas ultra-delgadas producido por un haz laser enfocado (Capítulo 5). Este estudio demuestra que el cambio en frecuencia es no lineal con la intensidad óptica aplicada y algunas frecuencias de resonancia llegan hasta la mitad de su valor inicial con intensidades ópticas de 2 mW. Estos resultados indican que para alcanzar los límites de detección en resonadores ultra-delgados, hay que considerar la influencia de la detección misma.

La fenomenología aquí encontrada desvela un nuevo mecanismo físico previamente poco estudiado en la literatura, que es el papel de la curvatura en las propiedades mecánicas de palancas ultra-delgadas. La última parte de la tesis se centra en el estudio de este efecto (Capítulo 6) a través de un detallado análisis teórico basado en argumentos topológicos.

Este estudio demuestra como pequeñas flexiones en palancas ultra-delgadas inducen tensiones que modifican en gran medida la rigidez de una estructura mecánica. Para placas sin anclajes, este efecto siempre aumenta la rigidez de la estructura. Sin embargo, cuando una placa está anclada a un soporte, la palanca no puede deformarse cerca de la región de anclaje y aparecen dos tipos de mecanismos que afectan a la rigidez de una estructura: *i*) un efecto puramente geométrico, que impide la deformación de la palanca cerca del anclaje, y *ii*) un efecto de tensión residual acumulada en el anclaje cuyo efecto es ablandar la estructura. Estos resultados teóricos fueron después corroborados experimentalmente con una macro-placa de aluminio, demostrando como este problema es fundamental en un amplia variedad de disciplinas como las ciencias naturales, la ingeniería mecánica y la micro y nanotecnología.

Acronyms

AFM	Atomic Force Microscopy
CCD	Charge-Coupled Device
DNA	Deoxyribonucleic Acid
FDTD	Finite-Difference Time Domain
FEM	Finite Element Method
LASER	Light Amplification by Stimulated Emission of Radiation
LED	Light Emission Diode
LPCVD	Low Pressure Chemical Vapor Deposition
LSPR	Localized Surface Plasmon Resonance
NA	Numerical Aperture
NEMS	Nanoelectromechanical Systems
NP	Nanoparticle
PC	Personal Computer
PSD	Position Sensitive Detector
RIE	Reactive Ion Etching
RMS	Root Mean Square
SEM	Scanning Electron Microscopy
SERS	Surface-enhanced Raman Spectroscopy
SMMS	Spatially Multiplexed Micro-Spectrophotometry
UV	Ultra Violet
WLI	White Light Interferometry

List of Figures

List of Publications

Publications on International Peer-Reviewed Journals

[1] Pini V., Tiribilli B., Gambi C. M. C. & Vassalli M., Dynamical characterization of vibrating AFM cantilevers forced by photothermal excitation. *Physical Review B* **81**, 054302 (2010).

[2] Vassalli M., Pini V. & Tiribilli B., Role of the driving laser position on atomic force microscopy cantilevers excited by photothermal and radiation pressure effects. *Applied Physics Letters* **97**, 143105 (2010).

[3] Kosaka P. M., Tamayo J., Gil-Santos E., Mertens J., Pini V., Martínez N.F., Ahumada O. & Calleja M., Simultaneous imaging of the topography and dynamic properties of nanomechanical systems by optical beam deflection microscopy *Journal of Applied Physics* **109**, 064315 (2011).

[4] Gil-Santos E., Ramos D., Pini V., Calleja M. & Tamayo J., Exponential tuning of the coupling constant of coupled microcantilevers by modifying their separation. *Applied Physics Letters* **98**, 123108 (2011).

[5] Pini, V., Tamayo, J., Gil-Santos E., Ramos D., Kosaka P., Hien-Duy T., van Rijn C., Calleja, M., Shedding light on axial stress effect on resonance frequencies of nanocantilevers. *Acs Nano* **5**, 4269-4275 (2011).

[6] Pini V., Tiribilli B., Gambi C. M. C. & Vassalli M., Erratum: Dynamical characterization of vibrating AFM cantilevers forced by photothermal excitation [Phys. Rev. B 81, 054302 (2010)]. *Physical Review B* **83**, 179904 (2011).

[7] Paoletti P., Basso M., Pini V., Tiribilli B. & Vassalli M., Self-driven soft imaging in liquid by means of photothermal excitation. *Journal of Applied Physics* **110**, 114315 (2011).

[8] Ramos D., Gil-Santos E., Pini V., Llorens J.M., Fernández-Regúlez M., San Paulo Á., Calleja M. & Tamayo, J., Optomechanics with silicon nanowires by harnessing confined electromagnetic modes. *Nano letters* **12**, 932-937 (2012).

[9] Tamayo J., Pini V., Kosaka P., Martinez N.F., Ahumada O. & Calleja M., Imaging the surface stress and vibration modes of a microcantilever by laser beam deflection microscopy. *Nanotechnology* **23**, 315501 (2012).

[10] Tamayo J., Ruz, J. J., Pini V., Kosaka P. & Calleja M., Quantification of the surface stress in microcantilever biosensors: revisiting Stoney's equation. *Nanotechnology* **23**, 475702 (2012).

[11] Gil-Santos E., Ramos D., Pini V., Llorens J., Fernández-Regúlez M., Calleja M., Tamayo J. & San Paulo Á., Optical back-action in silicon nanowire resonators: bolometric versus radiation pressure effects. *New Journal of Physics* **15**, 035001 (2013).

[12] Malvar O., Gil-Santos E., Ruz, J.J., Ramos D., Pini V., Fernandez-Regulez M., Calleja M., Tamayo J., & San Paulo A., Tapered silicon nanowires for enhanced nanomechanical sensing. *Applied Physics Letters* **103**, 033101 (2013).

[13] Ramos D., Gil-Santos E., Malvar O., Llorens J.M., Pini V., San Paulo A., Calleja M. & Tamayo J., Silicon nanowires: where mechanics and optics meet at the nanoscale. *Scientific reports* **3** 3445 (2013).

[14] Ruz, J., Tamayo, J., Pini, V., Kosaka, P.M. & Calleja, M. Physics of nanomechanical spectrometry of viruses. *Scientific reports* **4** 6051 (2014).

[15] Domínguez C. M., Kosaka P.M., Mokry G., Pini V., Malvar O., del rey M., Ramos D., San Paulo Á., Tamayo J. & Calleja M., Hydration induced stress on DNA monolayers grafted on microcantilevers. *Langmuir* **30**, 10962-10969 (2014).

[16] Cagliani A., Pini V., Tamayo J., Calleja M. & Davis Z. J., Ultrasensitive thermometer for atmospheric pressure operation based on

a micromechanical resonator. *Sensors and Actuators B: Chemical* **202**, 339-345 (2014).

[17] Kosaka, P. M., Pini V., Ruz J.J., da Silva R.A., González M.U., Ramos D., Calleja M., & Tamayo J., Detection of cancer biomarkers in serum using a hybrid mechanical and optoplasmonic nanosensor. *Nature Nanotechnology* **9**, 1047-1053 (2014).

[18] Pini V., Kosaka P. M., Ruz J.J., Malvar O., Encinar M., Tamayo J. & Calleja M., Spatially multiplexed dark-field microspectrophotometry for nanoplasmonics., *Scientific Report* **6**, 22836, doi: 10.1038/srep22836 (2016).

[19] Pini V., Ruz J.J., Kosaka P. M., Malvar O., Calleja M. & Tamayo J., How two-dimensional bending can extraordinarily stiffen thin sheets, *(submitted)*.

[20] Pini V., Kosaka P. M., Ruz J.J., Malvar O., Encinar M., Tamayo J. & Calleja M., Spatially multiplexed Micro-Spectrophotometry in bright-field mode for thin film characterization, *(submitted)*.

[21] Pini V., Ramos D., Malvar O., Ruz J.J., Kosaka P. M., Tamayo J. & Calleja M., Maximizing displacement sensitivity in microdrum optical cavities, *(submitted)*.

Conference Proceedings

[1] Kosaka, P. M., Pini V., Ruz J.J., da Silva R.A., González M.U., Ramos D., Calleja M., & Tamayo J., Detection of cancer biomarkers in serum by merging nanomechanics and optoplasmonics, *Solid-State Sensors, Actuators and Microsystems (TRANSDUCER),419-423* (2015).

Chapter Books

[1] Gil-Santos E., Pini V., San Paulo Á., Calleja M., Tamayo J. & Ramos D., Optical Transduction and Actuation of Subwavelength Nanomechanical Resonators. *Nanocantilever Beams: Modeling, Fabrication, and Applications*, 285 (2016).

Patents

[1] Tamayo J., Pini V., Kosaka, P. M., González S., & Calleja M., Method and system for characterization of nano and micromechanical structures, *US Patent 14/406,007* (2013), licensed to *Mecwins*.

[2] Kosaka P. M., Pini V., Tamayo J., Calleja M., Ruz J. J., Ramos D. & González M. U., A System biosensor and method for biosensing applications, *PCT/ES2015/070434* (2015), licensed to *Mecwins S.L.*

[3] Pini V., Kosaka P. M., Tamayo J., Calleja M., Ramos D., Malvar O., Ruz J. J. & Encinar M., Encinar, High-Resolution Spatially Multiplexed Spectral Analysis of Surfaces, *PCT/ES2015/070732* (2015), licensed to *Mecwins S.L.*

Bibliography

1 Ekinci, K. & Roukes, M. Nanoelectromechanical systems. *Rev. Sci. Instr.* **76**, 061101 (2005).

2 Erbe, A. *et al.* Mechanical mixing in nonlinear nanomechanical resonators. *Appl. Phys. Lett.* **77**, 3102-3104 (2009).

3 van Leeuwen, R., Castellanos-Gomez, A., Steele, G. A., van der Zant, H. S. J. & Venstra, W. J. Time-domain response of atomically thin MoS2 nanomechanical resonators. *Appl. Phys. Lett.* **105**, 041911, (2014).

4 Biswas, T. S. *et al.* Time-Resolved Mass Sensing of a Molecular Adsorbate Nonuniformly Distributed Along a Nanomechnical String. *Phys. Rev. Appl.* **3**, 064002 (2015).

5 Schmid, S., Wu, K., Larsen, P. E., Rindzevicius, T. & Boisen, A. Low-Power Photothermal Probing of Single Plasmonic Nanostructures with Nanomechanical String Resonators. *Nano Lett.* **14**, 2318-2321, (2014).

6 Yamada, S., Schmid, S., Larsen, T., Hansen, O. & Boisen, A. Photothermal Infrared Spectroscopy of Airborne Samples with Mechanical String Resonators. *Anal. Chem.* **85**, 10531-10535, (2013).

7 Larsen, T. *et al.* Ultrasensitive string-based temperature sensors. *Appl. Phys. Lett.* **98**, 121901, (2011).

8 Squires, T. M., Messinger, R. J. & Manalis, S. R. Making it stick: convection, reaction and diffusion in surface-based biosensors. *Nat. Biotechnol.* **26**, 417-426, (2008).

9 Waggoner, P. & Craighead, H. Micro-and nanomechanical sensors for environmental, chemical, and biological detection. *Lab Chip* **7**, 1238-1255 (2007).

10 Rahimi, M., Chae, I., Hawk, J. E., Mitra, S. K. & Thundat, T. Methane sensing at room temperature using photothermal cantilever deflection spectroscopy. *Sens. Actuators B: Chem.* **221**, 564-569, (2015).

11 Bargatin, I. *et al.* Large-Scale Integration of Nanoelectromechanical Systems for Gas Sensing Applications. *Nano Lett.* **12**, 1269-1274, (2012).

12 McCaig, H. C., Myers, E., Lewis, N. S. & Roukes, M. L. Vapor Sensing Characteristics of Nanoelectromechanical Chemical Sensors Functionalized Using Surface-Initiated Polymerization. *Nano Lett.* **14**, 3728-3732, (2014).

13 Naik, A., Hanay, M., Hiebert, W., Feng, X. & Roukes, M. Towards single-molecule nanomechanical mass spectrometry. *Nat. Nanotechnol.* **4**, 445-450 (2009).

14 Burg, T. *et al.* Weighing of biomolecules, single cells and single nanoparticles in fluid. *Nature* **446**, 1066-1069 (2007).

15 Jensen, K., Kim, K. & Zettl, A. An atomic-resolution nanomechanical mass sensor. *Nature Nanotechnol.* **3**, 533-537 (2008).

16 Lassagne, B., Garcia-Sanchez, D., Aguasca, A. & Bachtold, A. Ultrasensitive mass sensing with a nanotube electromechanical resonator. *Nano Lett.* **8**, 3735-3738 (2008).

17 Gil-Santos, E. *et al.* Nanomechanical mass sensing and stiffness spectrometry based on two-dimensional vibrations of resonant nanowires. *Nat. Nanotechnol.* **5**, 641-645 (2010).

18 Dohn, S., Svendsen, W., Boisen, A. & Hansen, O. Mass and position determination of attached particles on cantilever based mass sensors. *Rev. Sci. Instrum.* **78**, 103303 (2007).

19 Braun, T. *et al.* Quantitative time-resolved measurement of membrane protein–ligand interactions using microcantilever array sensors. *Nat. Nanotechnol.* **4**, 179-185 (2009).

20 Arcamone, J. *et al.* Nanomechanical mass sensor for spatially resolved ultrasensitive monitoring of deposition rates in stencil lithography. *Small* **5**, 176-180 (2009).

21 Arlett, J., Myers, E. & Roukes, M. Comparative advantages of mechanical biosensors. *Nature Nanotechnol.* **6**, 203-215 (2011).

22 Steele, G. *et al.* Strong coupling between single-electron tunneling and nanomechanical motion. *Science* **325**, 1103 (2009).

23 Naik, A. *et al.* Cooling a nanomechanical resonator with quantum back-action. *Nature* **443**, 193-196 (2006).

24 Yuan, M., Singh, V., Blanter, Y. M. & Steele, G. A. Large cooperativity and microkelvin cooling with a three-dimensional optomechanical cavity. *Nat. Comm.* **6**, (2015).

25 Wollman, E. E. *et al.* Quantum squeezing of motion in a mechanical resonator. *Science* **349**, 952-955, (2015).

26 Patil, S. B. *et al.* Decoupling competing surface binding kinetics and reconfiguration of receptor footprint for ultrasensitive stress assays. *Nat. Nanotechnol.* **10**, 899-907, (2015).

27 Domínguez, C. M. *et al.* Hydration induced stress on DNA monolayers grafted on microcantilevers. *Langmuir* **30**, 10962-10969 (2014).

28 Gavan, K. B., Drift, E. W. J. M. v. d., Venstra, W. J., Zuiddam, M. R. & Zant, H. S. J. v. d. Effect of undercut on the resonant behaviour of silicon nitride cantilevers. *J. Micromech. Microeng.* **19**, 035003 (2009).

29 Zhang, X. *et al.* Vibrational modes of ultrathin carbon nanomembrane mechanical resonators. *App. Phys. Lett.* **106**, 063107 (2015).

30 Yuan, M., Cohen, M. A. & Steele, G. A. Silicon nitride membrane resonators at millikelvin temperatures with quality factors exceeding 108. *Appl. Phys. Lett.* **107**, 263501, (2015).

31 Chakram, S., Patil, Y. S., Chang, L. & Vengalattore, M. Dissipation in Ultrahigh Quality Factor SiN Membrane Resonators. *Phys. Rev. Lett.* **112**, 127201 (2014).

32 Adiga, V. P. *et al.* Approaching intrinsic performance in ultra-thin silicon nitride drum resonators. *J. Appl. Phys.* **112**, 064323, (2012).

33 Olcum, S., Cermak, N., Wasserman, S. C. & Manalis, S. R. High-speed multiple-mode mass-sensing resolves dynamic nanoscale mass distributions. *Nat. Comm.* **6**, 7070 (2015).

34 Khan, M. F. *et al.* Online measurement of mass density and viscosity of pL fluid samples with suspended microchannel resonator. *Sens. Actuators B: Chem.* **185**, 456-461, (2013).

35 Kim, J. *et al.* Hollow Microtube Resonators via Silicon Self-Assembly toward Subattogram Mass Sensing Applications. *Nano Lett.*, doi:10.1021/acs.nanolett.5b03703 (2016).

36 Moser J., Eichler A., Güttinger J., Dykman, M. I. & Bachtold A. Nanotube mechanical resonators with quality factors of up to 5 million. *Nat. Nanotechnol.* **9**, 1007-1011, (2014).

37 Chaste J. *et al.* A nanomechanical mass sensor with yoctogram resolution. *Nat. Nanotechnol.* **7**, 301-304, (2012).

38 Kosaka, P. M. *et al.* Detection of cancer biomarkers in serum using a hybrid mechanical and optoplasmonic nanosensor. *Nat. Nanotechnol.* **9**, 1047-1053, (2014).

39 de la Rica, R. & Stevens, M. M. Plasmonic ELISA for the ultrasensitive detection of disease biomarkers with the naked eye. *Nat. Nanotechnol.* **7**, 821-824, (2012).

40 Wang, Z. *et al.* Black phosphorus nanoelectromechanical resonators vibrating at very high frequencies. *Nanoscale* **7**, 877-884 (2015).

41 Wang, Z., Lee, J. & Feng, P. X.-L. Spatial mapping of multimode Brownian motions in high-frequency silicon carbide microdisk resonators. *Nature Comm.* **5,** 5158 (2014).

42 Castellanos-Gomez, A., Singh, V., van der Zant, H. S. & Steele, G. A. Mechanics of freely-suspended ultrathin layered materials. *Ann. Phys.* **527**, 27-44 (2015).

43 Davami, K. *et al.* Ultralight shape-recovering plate mechanical metamaterials. *Nat. Comm.* **6**, 10019 (2015).

44 Kanjanaboos, P. *et al.* Self-assembled nanoparticle drumhead resonators. *Nano Lett.* **13**, 2158-2162 (2013).

45 Hermosa, C. *et al.* Mechanical and optical properties of ultralarge flakes of a metal-organic framework with molecular thickness. *Chem. Sci.* **6**, 2553-2558, (2015).

46 Salmon, A. R., Capener, M. J., Baumberg, J. J. & Elliott, S. R. Rapid microcantilever-thickness determination by optical interferometry. *Meas. Sci. Technol.* **25**, 015202 (2014).

47 Ghim, Y.-S., Rhee, H.-G., Yang, H.-S. & Lee, Y.-W. Thin-film thickness profile measurement using a Mirau-type low-coherence interferometer. *Meas. Sci. Technol.* **24**, 075002 (2013).

48 Dong, J. T. & Lu, R. S. Sensitivity analysis of thin-film thickness measurement by vertical scanning white-light interferometry. *Appl. Opt.* **51**, 5668-5675, (2012).

49 Debnath, S. K., Kothiyal, M. P., Schmit, J. & Hariharan, P. Spectrally resolved white-light phase-shifting interference microscopy for thickness-profile measurements of transparent thin film layers on patterned substrates. *Opt. Express* **14**, 4662-4667, (2006).

50 Tamayo, J., Kosaka, P. M., Ruz, J. J., San Paulo, A. & Calleja, M. Biosensors based on nanomechanical systems. *Chem. Soc. Rev.* **42**, 1287-1311, (2013).

51 Germer, T. A., Zwinkels, J. C. & Tsai, B. K. *Spectrophotometry: Accurate Measurement of Optical Properties of Materials*. Vol. 46 (Elsevier, 2014).

52 Martin, P. C. & Eyring, M. B. *Experimental Methods in the Physical Sciences* Vol. 46, 489-517 (Academic Press, 2014).

53 Gil-Santos, E. *et al.* Optical Transduction and Actuation of Subwavelength Nanomechanical Resonators. *Nanocantilever Beams: Modeling, Fabrication, and Applications*, 285 (2016).

54 Ramos, D. *et al.* Silicon nanowires: where mechanics and optics meet at the nanoscale. *Sci. Rep.*, **3** 3445 (2013).

55 Thijssen, R., Kippenberg, T. J., Polman, A. & Verhagen, E. Parallel Transduction of Nanomechanical Motion Using Plasmonic Resonators. *ACS Photonics* **1**, 1181-1188, (2014).

56 Talukdar, A. *et al.* Piezotransistive transduction of femtoscale displacement for photoacoustic spectroscopy. *Nat. Comm.* **6**, 7885 (2015).

57 Sansa, M., Fernández-Regúlez, M., Llobet, J., San Paulo, Á. & Pérez-Murano, F. High-sensitivity linear piezoresistive transduction for nanomechanical beam resonators. *Nat. Comm.* **5** 4313 (2014).

58 Hiebert, W., Vick, D., Sauer, V. & Freeman, M. Optical interferometric displacement calibration and thermomechanical noise detection in bulk focused ion beam-fabricated nanoelectromechanical systems. *J. Micromech. Microeng.* **20**, 115038 (2010).

59 Karabacak, D., Kouh, T. & Ekinci, K. Analysis of optical interferometric displacement detection in nanoelectromechanical systems. *J. Appl. Phys.* **98**, 124309 (2005).

60 Tamayo, J. *et al.* Imaging the surface stress and vibration modes of a microcantilever by laser beam deflection microscopy. *Nanotechnology* **23**, 315501 (2012).

61 Yoshikawa, G. *et al.* Two dimensional array of piezoresistive nanomechanical Membrane-type Surface stress Sensor(MSS) with improved sensitivity. *Sensors* **12**, 15873-15887, (2012).

62 Yoshikawa, G., Akiyama, T., Gautsch, S., Vettiger, P. & Rohrer, H. Nanomechanical membrane-type surface stress sensor. *Nano Lett.* **11**, 1044-1048, (2011).

63 Karabalin, R. B., Villanueva, L. G., Matheny, M. H., Sader, J. E. & Roukes, M. L. Stress-induced variations in the stiffness of micro- and nanocantilever beams. *Phys. Rev. Lett.* **108** 236101 (2012).

64 Clark, M. T., Sader, J. E., Cleveland, J. P. & Paul, M. R. Spectral properties of microcantilevers in viscous fluid. *Phys. Rev. E* **81**, 046306 (2010).

65 Malvar, O. *et al.* Highly sensitive measurement of liquid density in air using suspended microcapillary resonators. *Sensors* **15**, 7650-7657 (2015).

66 Abbott, B. P. *et al.* Observation of Gravitational Waves from a Binary Black Hole Merger. *Phys. Rev. Lett.* **116**, 061102 (2016).

67 Paolino, P., Sandoval, F. A. A. & Bellon, L. Quadrature phase interferometer for high resolution force spectroscopy. *Rev. Sci. Instrum.* **84**, 095001 (2013).

68 Gil-Santos, E. *et al.* Optical back-action in silicon nanowire resonators: bolometric versus radiation pressure effects. *New J. Phys.* **15**, 035001 (2013).

69 Pini, V. *et al.* Shedding light on axial stress effect on resonance frequencies of nanocantilevers. *Acs Nano* **5**, 4269-4275 (2011).

70 Ramos, D. *et al.* Optomechanics with Silicon Nanowires by Harnessing Confined Electromagnetic Modes. *Nano Lett.* **12**, 932-937, (2012).

71 Sandoval, F. A., Geitner, M., Bertin, É. & Bellon, L. Resonance frequency shift of strongly heated micro-cantilevers. *J. Appl. Phys.* **117**, 234503, (2015).

72 Moulia, B. Leaves as shell structures: double curvature, auto-stresses, and minimal mechanical energy constraints on leaf rolling in grasses. *J. Plant Growth Regul.* **19**, 19-30 (2000).

73 Ha, N. S., Truong, Q. T., Goo, N. S. & Park, H. C. Biomechanical Properties of Insect Wings: The Stress Stiffening Effects on the Asymmetric Bending of the Allomyrina dichotoma Beetle's Hind Wing. *PLOS One* **8**, 12 (2013).

74 Park, Y. *et al.* Metabolic remodeling of the human red blood cell membrane. *Proc. Natl. Acad. Sci. USA* **107**, 1289-1294 (2010).

75 Lachut, M. J. & Sader, J. E. Effect of surface stress on the stiffness of thin elastic plates and beams. *Phys. Rev. B* **85,** 085440 (2012).

76 Verbridge, S. S., Shapiro, D. F., Craighead, H. G. & Parpia, J. M. Macroscopic Tuning of Nanomechanics: Substrate Bending for Reversible Control of Frequency and Quality Factor of Nanostring Resonators. *Nano Lett.* **7**, 1728-1735, (2007).

77 Degen, C., Poggio, M., Mamin, H., Rettner, C. & Rugar, D. Nanoscale magnetic resonance imaging. *Proc. Natl. Acad. Sci.* **106**, 1313 (2009).

78 Li, M., Tang, H. & Roukes, M. Ultra-sensitive NEMS-based cantilevers for sensing, scanned probe and very high-frequency applications. *Nat. Nanotechnol.* **2**, 114-120 (2007).

79 Laurent, J., Steinberger, A. & Bellon, L. Functionalized AFM probes for force spectroscopy: eigenmode shapes and stiffness calibration through thermal noise measurements. *Nanotechnology* **24**, 225504 (2013).

80 Ares, P., Jaafar, M., Gil, A., Gómez-Herrero, J. & Asenjo, A. Magnetic Force Microscopy in Liquids. *Small* **11**, 4731-4736, (2015).

81 Chiesa, M. *et al.* Detection of the Early Stage of Recombinational DNA Repair by Silicon Nanowire Transistors. *Nano Lett.* **12**, 1275-1281, (2012).

82 Varshney, M. *et al.* Prion protein detection using nanomechanical resonator arrays and secondary mass labeling. *Anal. Chem* **80**, 2141-2148 (2008).

83 Ahumada, O. *et al.* Sensitive thermal transitions of nanoscale polymer samples using the bimetallic effect: Application to ultra-thin polythiophene. *Rev. Sci. Instrum.* **84**, 053904, (2013).

84 Soccio, M. *et al.* Thermomechanical response of a semicrystalline polymer in the vicinity of the melting by using microcantilever technology. *Appl. Phys. Lett.* **104**, 251904, (2014).

85 Otte, M. A. *et al.* Tailored Height Gradients in Vertical Nanowire Arrays via Mechanical and Electronic Modulation of Metal-Assisted Chemical Etching. *Small* **11**, 4201-4208, (2015).

86 Boisen, A., Dohn, S., Keller, S. S., K., Schmid, S. & Tenje M., Cantilever-like micromechanical sensors. *Rep. Prog. Phys.* **74**, 036101 (2011).

87 Gil-Santos, E., Ramos, D., Pini, V., Calleja, M. & Tamayo, J. Exponential tuning of the coupling constant of coupled microcantilevers by modifying their separation. *Appl. Phys. Lett.* **98**, 123108 (2011).

88 López-Polín, G. *et al.* Increasing the elastic modulus of graphene by controlled defect creation. *Nat. Phys.* **11**, 26-31 (2015).

89 Boscá, A., Pedrós, J., Martínez, J., Palacios, T. & Calle, F. Automatic graphene transfer system for improved material quality and efficiency. *Sci. Rep.* **6**, 21676, (2016).

90 Pavia, D., Lampman, G., Kriz, G. & Vyvyan, J. *Introduction to spectroscopy*. (Cengage Learning, 2008).

91 Hollas, J. M. *Modern spectroscopy*. (John Wiley & Sons, 2004).

92 Hammes, G. G. *Spectroscopy for the biological sciences*. (John Wiley & Sons, 2005).

93 Buencuerpo, J., Llorens, J., Dotor, M. & Ripalda, J. Broadband antireflective nano-cones for tandem solar cells. *Opt. Express* **23** (7), A322-A336 (2015).

94 Ramiro, Í. *et al.* Optically Triggered Infrared Photodetector. *Nano Lett.* **15**, 224-228, (2015).

95 Torres-Costa, V. & Martín-Palma, R. J. Application of nanostructured porous silicon in the field of optics. A review. *J. Mater. Sci.* **45**, 2823-2838, (2010).

96 Lavin, G. I. Simplified Ultraviolet Microscopy. *Rev. Sci. Instrum.* **14**, 375-376, (1943).

97 Chang, W.-S. & Link, S. Enhancing the Sensitivity of Single-Particle Photothermal Imaging with Thermotropic Liquid Crystals. *J. Phys. Chem. Lett.* **3**, 1393-1399, (2012).

98 Massonnet, G. *et al.* Raman spectroscopy and microspectrophotometry of reactive dyes on cotton fibres: Analysis and detection limits. *Forensic Sci. Int.* **222**, 200-207 (2012).

99 Ou, J.-Y., Plum, E., Jiang, L. & Zheludev, N. I. Reconfigurable photonic metamaterials. *Nano Lett.* **11**, 2142-2144 (2011).

100 Stavenga, D., Giraldo, M. & Hoenders, B. Reflectance and transmittance of light scattering scales stacked on the wings of pierid butterflies. *Opt. Express* **14**, 4880-4890 (2006).

101 Wilts, B. D., Leertouwer, H. L. & Stavenga, D. G. Imaging scatterometry and microspectrophotometry of lycaenid butterfly wing scales with perforated multilayers. *J. R. Soc. Interface*, **6,** S185-S192 (2008).

102 Ye, X., Chen, J., Diroll, B. T. & Murray, C. B. Tunable Plasmonic Coupling in Self-Assembled Binary Nanocrystal Superlattices Studied by Correlated Optical Microspectrophotometry and Electron Microscopy. *Nano Lett.* **13**, 1291-1297 (2013).

103 Zięba-Palus, J. Microspectrophotometry in Forensic Science. *Encyclopedia of Analytical Chemistry* (Wiley, 2006).

104 Kindzelskii, A. L., Sitrin, R. G. & Petty, H. R. Cutting edge: optical microspectrophotometry supports the existence of gel phase lipid rafts at the lamellipodium of neutrophils: apparent role in calcium signaling. *J.Immunol.* **172**, 4681-4685 (2004).

105 Schmidt, M. A., Lei, D. Y., Wondraczek, L., Nazabal, V. & Maier, S. A. Hybrid nanoparticle–microcavity-based plasmonic nanosensors with improved detection resolution and extended remote-sensing ability. *Nat. Comm.* **3**, 1108 (2012).

106 Olson, J. *et al.* Optical characterization of single plasmonic nanoparticles. *Chem. Soc. Rev.* **44**, 40-57, (2015).

107 Nicoletti, O. *et al.* Three-dimensional imaging of localized surface plasmon resonances of metal nanoparticles. *Nature* **502**, 80-84 (2013).

108 Nehl, C. L. *et al.* Scattering spectra of single gold nanoshells. *Nano Lett.* **4**, 2355-2359 (2004).

109 Mercatelli, R. *et al.* Quantitative readout of optically encoded gold nanorods using an ordinary dark-field microscope. *Nanoscale* **5**, 9645-9650 (2013).

110 Hu, M. *et al.* Gold nanostructures: engineering their plasmonic properties for biomedical applications. *Chem. Soc. Rev.* **35**, 1084-1094, (2006).

111 Fan, J. A. *et al.* Self-assembled plasmonic nanoparticle clusters. *Science* **328**, 1135-1138 (2010).

112 Deotare, P. B., McCutcheon, M. W., Frank, I. W., Khan, M. & Lončar, M. High quality factor photonic crystal nanobeam cavities. *Appl. Phys. Lett.* **94**, 121106 (2009).

113 de Angelis, M. *et al.* Plasmon resonance of gold nanorods for all-optical drawing of liquid droplets. *Appl. Phys. Lett.* **103**, 163112 (2013).

114 Mayer, K. M. & Hafner, J. H. Localized Surface Plasmon Resonance Sensors. *Chem. Rev.* **111**, 3828-3857, (2011).

115 Ringe, E., Sharma, B., Henry, A.-I., Marks, L. D. & Van Duyne, R. P. Single nanoparticle plasmonics. *Phys. Chem. Chem. Phys.* **15**, 4110-4129, (2013).

116 Eustis, S. & El-Sayed, M. A. Why gold nanoparticles are more precious than pretty gold: Noble metal surface plasmon resonance and its enhancement of the radiative and nonradiative properties of nanocrystals of different shapes. *Chem. Soc. Rev.* **35**, 209-217, (2006).

117 Vitrey, A., Aigouy, L., Prieto, P., García-Martín, J. M. & González, M. U. Parallel Collective Resonances in Arrays of Gold Nanorods. *Nano Lett.* **14**, 2079-2085, (2014).

118 Mock, J. J., Barbic, M., Smith, D. R., Schultz, D. A. & Schultz, S. Shape effects in plasmon resonance of individual colloidal silver nanoparticles. *J. Chem. Phys.* **116**, 6755-6759, (2002).

119 Weitz, E. A., Lewandowski, C., Smolensky, E. D., Marjańska, M. & Pierre, V. C. A Magnetoplasmonic Imaging Agent for Copper(I) with Dual Response by MRI and Dark Field Microscopy. *ACS Nano* **7**, 5842-5849, (2013).

120 Zijlstra, P., Paulo, P. M. R. & Orrit, M. Optical detection of single non-absorbing molecules using the surface plasmon resonance of a gold nanorod. *Nat. Nanotechnol.* **7**, 379-382 (2012).

121 Ament, I., Prasad, J., Henkel, A., Schmachtel, S. & Sönnichsen, C. Single Unlabeled Protein Detection on Individual Plasmonic Nanoparticles. *Nano Lett.* **12**, 1092-1095, (2012).

122 Chen, S., Svedendahl, M., Duyne, R. P. V. & Käll, M. Plasmon-Enhanced Colorimetric ELISA with Single Molecule Sensitivity. *Nano Lett.* **11**, 1826-1830 (2011).

123 Sannomiya, T. & Vörös, J. Single plasmonic nanoparticles for biosensing. *Trends Biotechnol.* **29**, 343-351 (2011).

124 Zhang, X., Chen, Y.L., Liu, R.S. & Tsai, D. P., Plasmonic photocatalysis. *Rep. Prog. Phys.* **76**, 046401 (2013).

125 Mock, J. J. *et al.* Distance-Dependent Plasmon Resonant Coupling between a Gold Nanoparticle and Gold Film. *Nano Lett.* **8**, 2245-2252, (2008).

126 Vesseur, E. J. R. & Polman, A. Plasmonic Whispering Gallery Cavities As Optical Nanoantennas. *Nano Lett.* **11**, 5524-5530, (2011).

127 Thijssen, R., Kippenberg, T. J., Polman, A. & Verhagen, E. Plasmomechanical resonators based on dimer nanoantennas. *Nano Lett.* **15,** 6, 3971-3976 (2015).

128 Knight, M. W. *et al.* Aluminum Plasmonic Nanoantennas. *Nano Lett.* **12**, 6000-6004, (2012).

129 Coenen, T., Vesseur, E. J. R., Polman, A. & Koenderink, A. F. Directional Emission from Plasmonic Yagi–Uda Antennas Probed by Angle-Resolved Cathodoluminescence Spectroscopy. *Nano Lett.* **11**, 3779-3784, (2011).

130 Lal, S. *et al.* Tailoring plasmonic substrates for surface enhanced spectroscopies. *Chem. Soc. Rev.* **37**, 898-911, (2008).

131 Zuloaga, J., Prodan, E. & Nordlander, P. Quantum Plasmonics: Optical Properties and Tunability of Metallic Nanorods. *ACS Nano* **4**, 5269-5276, (2010).

132 Novo, C., Funston, A. M., Pastoriza-Santos, I., Liz-Marzán, L. M. & Mulvaney, P. Spectroscopy and High-Resolution Microscopy of Single Nanocrystals by a Focused Ion Beam Registration Method. *Angew. Chem. Int. Ed.* **119**, 3587-3590, (2007).

133 Song, Y. *et al.* Identification of single nanoparticles. *Nanoscale* **3**, 31-44, (2011).

134 Juvé, V. *et al.* Size-Dependent Surface Plasmon Resonance Broadening in Nonspherical Nanoparticles: Single Gold Nanorods. *Nano Lett.* **13**, 2234-2240, (2013).

135 Hoggard, A. *et al.* Using the Plasmon Linewidth To Calculate the Time and Efficiency of Electron Transfer between Gold Nanorods and Graphene. *ACS Nano* **7**, 11209-11217, (2013).

136 Chen, H. *et al.* Observation of the Fano Resonance in Gold Nanorods Supported on High-Dielectric-Constant Substrates. *ACS Nano* **5**, 6754-6763, (2011).

137 Liu, Y. & Huang, C. Z. Real-Time Dark-Field Scattering Microscopic Monitoring of the in Situ Growth of Single Ag@Hg Nanoalloys. *ACS Nano* **7**, 11026-11034, (2013).

138 Berciaud, S., Cognet, L., Blab, G. A. & Lounis, B. Photothermal Heterodyne Imaging of Individual Nonfluorescent Nanoclusters and Nanocrystals. *Phys. Rev. Lett.* **93**, 257402 (2004).

139 Selmke, M., Braun, M. & Cichos, F. Photothermal Single-Particle Microscopy: Detection of a Nanolens. *ACS Nano* **6**, 2741-2749, (2012).

140 Arbouet, A. *et al.* Direct Measurement of the Single-Metal-Cluster Optical Absorption. *Phys. Rev. Lett.* **93**, 127401 (2004).

141 Baida, H. *et al.* Quantitative Determination of the Size Dependence of Surface Plasmon Resonance Damping in Single Ag@SiO2 Nanoparticles. *Nano Lett.* **9**, 3463-3469, (2009).

142 Wang, G., Sun, W., Luo, Y. & Fang, N. Resolving Rotational Motions of Nano-objects in Engineered Environments and Live Cells with Gold Nanorods and Differential Interference Contrast Microscopy. *J. Am. Chem. Soc.* **132**, 16417-16422, (2010).

143 Knight, M. W., Wu, Y., Lassiter, J. B., Nordlander, P. & Halas, N. J. Substrates Matter: Influence of an Adjacent Dielectric on an Individual Plasmonic Nanoparticle. *Nano Lett.* **9**, 2188-2192, (2009).

144 Lee, B. *et al.* Fano Resonance and Spectrally Modified Photoluminescence Enhancement in Monolayer MoS2 Integrated with Plasmonic Nanoantenna Array. *Nano Lett.* **15**, 3646-3653, (2015).

145 Liu, H.-W. *et al.* Single-Crystalline Aluminum Nanostructures on a Semiconducting GaAs Substrate for Ultraviolet to Near-Infrared Plasmonics. *ACS Nano* **9**, 3875-3886, (2015).

146 Fan, J. A. *et al.* Near-Normal Incidence Dark-Field Microscopy: Applications to Nanoplasmonic Spectroscopy. *Nano Lett.* **12**, 2817-2821, (2012).

147 Wu, Y. & Nordlander, P. Finite-Difference Time-Domain Modeling of the Optical Properties of Nanoparticles near Dielectric Substrates. *J. Phys. Chem. C* **114**, 7302-7307, (2010).

148 Knight, M. W., Fan, J., Capasso, F. & Halas, N. J. Influence of excitation and collection geometry on the dark field spectra of individual plasmonic nanostructures. *Opt. Express* **18**, 2579-2587 (2010).

149 Marhaba, S. *et al.* Surface Plasmon Resonance of Single Gold Nanodimers near the Conductive Contact Limit. *J. Phys. Chem. C* **113**, 4349-4356 (2009).

150 Nordlander, P., Oubre, C., Prodan, E., Li, K. & Stockman, M. Plasmon hybridization in nanoparticle dimers. *Nano Lett.* **4**, 899-903 (2004).

151 Bohren, C. F. & Huffman, D. R. *Absorption and scattering of light by small particles*. (John Wiley & Sons, 2008).

152 Johnson, P. B. & Christy, R. W. Optical Constants of the Noble Metals. *Phys. Rev. B* **6**, 4370-4379 (1972).

153 Vuye, G. *et al.* Temperature dependence of the dielectric function of silicon using in situ spectroscopic ellipsometry. *Thin Solid Films* **233**, 166-170 (1993).

154 García de Abajo, F. J. Multiple scattering of radiation in clusters of dielectrics. *Phys. Rev. B* **60**, 6086-6102 (1999).

155 Chen, H. *et al.* Effect of the Dielectric Properties of Substrates on the Scattering Patterns of Gold Nanorods. *ACS Nano* **5**, 4865-4877, (2011).

156 Cottat, M. *et al.* High Sensitivity, High Selectivity SERS Detection of MnSOD Using Optical Nanoantennas Functionalized with Aptamers. *J. Phys. Chem. C* **119**, 15532-15540, (2015).

157 Douglas, P., Stokes, R. J., Graham, D. & Smith, W. E. Immunoassay for P38 MAPK using surface enhanced resonance Raman spectroscopy (SERRS). *Analyst* **133**, 791-796, (2008).

158 Grubisha, D. S., Lipert, R. J., Park, H.-Y., Driskell, J. & Porter, M. D. Femtomolar Detection of Prostate-Specific Antigen: An Immunoassay Based on Surface-Enhanced Raman Scattering and Immunogold Labels. *Anal. Chem.* **75**, 5936-5943, (2003).

159 Cowan, G. *Statistical data analysis*. (Oxford University Press, 1998).

160 Myroshnychenko, V. *et al.* Modelling the optical response of gold nanoparticles. *Chem. Soc. Rev.* **37**, 1792-1805, (2008).

161 Van Zant, P. & Chapman. *Microchip fabrication: a practical guide to semiconductor processing*. (McGraw-Hill New York, 2000).

162 Heavens, O. S. *Optical properties of thin solid films*. (Courier Corporation, 1991).

163 Bates, J., Dudney, N., Neudecker, B., Ueda, A. & Evans, C. Thin-film lithium and lithium-ion batteries. *Solid State Ion.* **135**, 33-45 (2000).

164 Aberle, A. G. Thin-film solar cells. *Thin Solid Films* **517**, 4706-4710 (2009).

165 Azzam, R. M. A. & Bashara, N. M. *Ellipsometry and Polarized Light* (Elsevier, 1977).

166 Hauge, P. S. Recent developments in instrumentation in ellipsometry. *Surf. Sci.* **96**, 108-140, (1980).

167 Erman, M. & Theeten, J. B. Spatially resolved ellipsometry. *J. Appl. Phys.* **60**, 859-873, (1986).

168 Ghim, Y.-S. & Kim, S.-W. Spectrally resolved white-light interferometry for 3D inspection of a thin-film layer structure. *Appl. Opt.* **48**, 799-803 (2009).

169 Wu, K., Lee, C.-C., Brock, N. J. & Kimbrough, B. Multilayer thin-film inspection through measurements of reflection coefficients. *Opt. Lett.* **36**, 3269-3271 (2011).

170 Kim, S. W. & Kim, G. H. Thickness-profile measurement of transparent thin-film layers by white-light scanning interferometry. *Appl. Opt.* **38**, 5968-5973 (1999).

171 Kim, D., Kim, S., Kong, H. J. & Lee, Y. Measurement of the thickness profile of a transparent thin film deposited upon a pattern structure with an acousto-optic tunable filter. *Opt. Lett.* **27**, 1893-1895 (2002).

172 Ghim, Y. S. & Kim, S. W. Thin-film thickness profile and its refractive index measurements by dispersive white-light interferometry. *Opt. Express* **14**, 11885-11891, (2006).

173 Scholz, T., Debski, T., Barth, W., Römer, F. & Hillmer, H. A high-resolution optical study of cantilever heterostructure layer geometries. *J.Micromech. Microeng.* **16**, 2765-2770, (2006).

174 Ghim, Y.-S. & Kim, S.-W. Fast, precise, tomographic measurements of thin films. *Appl. Phys. Lett.* **91**, 091903 (2007).

175 Hlubina, P., Luňáček, J., Ciprian, D. & Chlebus, R. Spectral interferometry and reflectometry used to measure thin films. *Appl. Phys. B* **92**, 203-207, (2008).

176 Hirth, F., Buck, T. C., Grassi, A. P. & Koch, A. W. Depth-sensitive thin film reflectometer. *Meas. Sci. Technol.* **21**, 12, 125301 (2010).

177 Reed, J., Wilkinson, P., Schmit, J., Klug, W. & Gimzewski, J. K. Observation of nanoscale dynamics in cantilever sensor arrays. *Nanotechnology* **17**, 3873-3879, (2006).

178 Clifford, C. A. & Seah, M. P. Improved methods and uncertainty analysis in the calibration of the spring constant of an atomic force microscope cantilever using static experimental methods. *Meas. Sci. Technol.* **20**, 125501 (2009).

179 Webber, G. B., Stevens, G. W., Grieser, F., Dagastine, R. R. & Chan, D. Y. C. Variations in properties of atomic force microscope cantilevers fashioned from the same wafer. *Nanotechnology* **19**, 105709 (2008).

180 Wilkinson, P. R. & Gimzewski, J. K. Thin film interference in the optomechanical response of micromechanical silicon cantilevers. *Appl. Phys. Lett.* **89**, 241916, (2006).

181 Gomez-Martinez, R. *et al.* Silicon chips detect intracellular pressure changes in living cells. *Nat. Nanotechnol.* **8**, 517-521, (2013).

182 Born, M. & Wolf, E. *Principles of optics: electromagnetic theory of propagation, interference and diffraction of light*. (Cambridge University Press, 1999).

183 McKendry, R. *et al.* Multiple label-free biodetection and quantitative DNA-binding assays on a nanomechanical cantilever array. *Proc. Natl. Acad. Sci. USA* **99**, 9783-9788, (2002).

184 Lang, H. P., Hegner, M. & Gerber, C. Cantilever array sensors. *Mater. Today* **8**, 30-36, (2005).

185 Lang, H. P. *et al.* Sequential position readout from arrays of micromechanical cantilever sensors. *Appl. Phys. Lett.* **72**, 383-385 (1998).

186 Martínez, N. *et al.* High throughput optical readout of dense arrays of nanomechanical systems for sensing applications. *Rev. Sci. Instrum.* **81**, 125109 (2010).

187 Kosaka, P. M. *et al.* Tackling reproducibility in microcantilever biosensors: a statistical approach for sensitive and specific end-point detection of immunoreactions. *Analyst* **138**, 863-872 (2013).

188 Kosaka, P. M. *et al.*,Detection of cancer biomarkers in serum by merging nanomechanics and optoplasmonics, *Conference on Solid-State Sensors, Actuators and Microsystems (TRANSDUCERS)*, 419-423, doi:10.1109/TRANSDUCERS.2015.7180950 (2015).

189 Leondes, C. T. *Mems/Nems:(1) Handbook Techniques and Applications Design Methods,(2) Fabrication Techniques,(3) Manufacturing Methods,(4) Sensors and Actuators,(5) Medical Applications and MOEMS*. (Springer Science & Business Media, 2007).

190 Khanna, V. K. *Nanosensors: physical, chemical, and biological*. (CRC Press, 2011).

191 Kosaka, P. M. *et al.* Simultaneous imaging of the topography and dynamic properties of nanomechanical systems by optical beam deflection microscopy. *J. Appl. Phys.* **109**, 064315 (2011).

192 Hariharan, P. *Optical interferometry*. (Academic Press, 2003).

193 Paolino, P., Tiribilli, B. & Bellon, L. Direct measurement of spatial modes of a microcantilever from thermal noise. *J. Appl. Phys.* **106**, 094313 (2009).

194 Paolino, P. & Bellon, L. Frequency dependence of viscous and viscoelastic dissipation in coated micro-cantilevers from noise measurement. *Nanotechnology* **20**, 405705 (2009).

195 Patil, S. *et al.* A highly sensitive atomic force microscope for linear measurements of molecular forces in liquids. *Rev. Sci. Instrum.* **76**, 103705 (2005).

196 Waters, R. L. & Aklufi, M. E. Micromachined Fabry–Perot interferometer for motion detection. *Appl. Phys. Lett.* **81**, 3320-3322 (2002).

197 Mamin, H. & Rugar, D. Sub-attonewton force detection at millikelvin temperatures. *Appl. Phys. Lett.* **79**, 3358-3360 (2001).

198 Teufel, J. D., DonnerT, Castellanos-Beltran, M. A., Harlow, J. W. & Lehnert, K. W. Nanomechanical motion measured with an imprecision below that at the standard quantum limit. *Nat. Nanotechnol.* **4**, 820-823, (2009).

199 Onomitsu, K., Mitsuhara, M., Yamamoto, H. & Yamaguchi H. Ultrahigh- Q Micromechanical Resonators by Using Epitaxially Induced Tensile Strain in GaNAs. *Appl. Phys. Express* **6**, 111201 (2013).

200 Lee, J., Wang, Z., He, K., Shan, J. & Feng, P. X.-L. High frequency MoS2 nanomechanical resonators. *ACS nano* **7**, 6086-6091 (2013).

201 Stroke, G. W. *Coherent optics and holography*. (Academic Press Inc., New York, 1966).

202 Sarrazin, M., Herman, A. & Deparis, O. First-principle calculation of solar cell efficiency under incoherent illumination. *Opt. Express* **21**, A616-A630 (2013).

203 Philipp, H. R. Optical properties of silicon nitride. *J. Electrochem. Soc.* **120**, 295-300 (1973).

204 Gao, L., Lemarchand, F. & Lequime, M. Refractive index determination of SiO2 layer in the UV/Vis/NIR range: spectrophotometric reverse engineering on single and bi-layer designs. *J. Eur. Opt. Soc.* **8** 13010 (2013).

205 Burek, M. J., Ramos, D., Patel, P., Frank, I. W. & Lončar, M. Nanomechanical resonant structures in single-crystal diamond. *Appl. Phys. Lett.* **103**, 131904 (2013).

206 Zwickl, B. M. *et al.* High quality mechanical and optical properties of commercial silicon nitride membranes. *Appl. Phys. Lett.* **92**, 103125, (2008).

207 Villanueva, L. G. & Schmid, S. Evidence of Surface Loss as Ubiquitous Limiting Damping Mechanism in SiN Micro- and Nanomechanical Resonators. *Phys. Rev. Lett.* **113**, 227201 (2014).

208 Schmid, S., Jensen, K. D., Nielsen, K. H. & Boisen, A. Damping mechanisms in high-Q micro and nanomechanical string resonators. *Phys. Rev. B* **84**, 165307 (2011).

209 Kermany, A. R. *et al.* Microresonators with Q-factors over a million from highly stressed epitaxial silicon carbide on silicon. *Appl. Phys. Lett.* **104**, 081901, (2014).

210 Thijssen, R., Verhagen, E., Kippenberg, T. J. & Polman, A. Plasmon Nanomechanical Coupling for Nanoscale Transduction. *Nano Lett.* **13**, 3293-3297, (2013).

211 Schmid, S. & Hierold, C. Damping mechanisms of single-clamped and prestressed double-clamped resonant polymer microbeams. *J. Appl. Phys.* **104**, 093516, (2008).

212 Cole, G. D. *et al.* Tensile-strained $In_xGa_{1-x}P$ membranes for cavity optomechanics. *Appl. Phys. Lett.* **104**, 201908, (2014).

213 Biswas, T. S. *et al.* Remote Sensing in Hybridized Arrays of Nanostrings. *Nano Lett.* **14**, 2541-2545, (2014).

214 Graff, K. F. *Wave motion in elastic solids*. (Courier Corporation, 2012).

215 Wang, Z., Lee, J., He, K., Shan, J. & Feng, P. X.-L. Embracing structural nonidealities and asymmetries in two-dimensional nanomechanical resonators. *Sci. Rep.* **4,** 3919 (2014).

216 Gil-Santos, E. *et al.* High-frequency nano-optomechanical disk resonators in liquids. *Nat. Nanotechnol.* **10**, 810-816 (2015).

217 Sage, E. *et al.* Neutral particle mass spectrometry with nanomechanical systems. *Nat. Comm.* **6**, 6482 (2015).

218 Hanay, M. S. *et al.* Single-protein nanomechanical mass spectrometry in real time. *Nat. Nanotechnol.* **7**, 602-608, (2012).

219 Penedo, M. *et al.* Enhanced efficiency in the excitation of higher modes for atomic force microscopy and mechanical sensors operated in liquids. *Appl. Phys. Lett.* **105**, 173102, (2014).

220 Villanueva, L. G. *et al.* Surpassing Fundamental Limits of Oscillators Using Nonlinear Resonators. *Phys. Rev. Lett.* **110**, 177208 (2013).

221 Matheny, M. H. *et al.* Phase Synchronization of Two Anharmonic Nanomechanical Oscillators. *Phys. Rev. Lett.* **112**, 014101 (2014).

222 Prakash, G., Raman, A., Rhoads, J. & Reifenberger, R. G. Parametric noise squeezing and parametric resonance of microcantilevers in air and liquid environments. *Rev. Sci. Instrum.* **83**, 065109, (2012).

223 Villanueva, L. G. *et al.* A Nanoscale Parametric Feedback Oscillator. *Nano Lett.* **11**, 5054-5059, (2011).

224 Paoletti, P., Basso, M., Pini, V., Tiribilli, B. & Vassalli, M. Self-driven soft imaging in liquid by means of photothermal excitation. *J. Appl. Phys.* **110**, 114315 (2011).

225 Barton, R. A. *et al.* Photothermal Self-Oscillation and Laser Cooling of Graphene Optomechanical Systems. *Nano Lett.* **12**, 4681-4686, (2012).

226 Lachut, M. & Sader, J. Effect of Surface Stress on the Stiffness of Cantilever Plates. *Phys. Rev. Lett.* **99**, 206102 (2007).

227 Ramos, D. *et al.* Arrays of Dual Nanomechanical Resonators for Selective Biological Detection. *Anal. Chem.* **81**, 2274-2279 (2009).

228 Fukuma, T. Wideband low-noise optical beam deflection sensor with photothermal excitation for liquid-environment atomic force microscopy. *Rev. Sci. Instrum.* **80**, 023707 (2009).

229 Enning, R. *et al.* A high frequency sensor for optical beam deflection atomic force microscopy. *Rev. Sci. Instrum.* **82**, 043705 (2011).

230 Schlesinger, I., Kuchuk, K. & Sivan, U. An ultra-low noise optical head for liquid environment atomic force microscopy. *Rev. Sci. Instrum.* **86**, 083705 (2015).

231 Carslaw, H. S. & Jaeger, J. C. *Conduction of heat in solids.* (*Oxford: Clarendon Press, 1959*).

232 Kiracofe, D., Kobayashi, K., Labuda, A., Raman, A. & Yamada, H. High efficiency laser photothermal excitation of microcantilever vibrations in air and liquids. *Rev. Sci. Instrum.* **82**, 013702, (2011).

233 Pini, V., Tiribilli, B., Gambi, C. M. C. & Vassalli, M. Dynamical characterization of vibrating AFM cantilevers forced by photothermal excitation. *Phys. Rev. B* **81**, 054302 (2010).

234 Prashanthi, K., Phani, A. & Thundat, T. Photothermal Electrical Resonance Spectroscopy of Physisorbed Molecules on a Nanowire Resonator. *Nano Lett.* **15**, 5658-5663, (2015).

235 Vassalli, M., Pini, V. & Tiribilli, B. Role of the driving laser position on atomic force microscopy cantilevers excited by photothermal and radiation pressure effects. *Appl. Phys. Lett.* **97**, 143105 (2010).

236 Song, X. *et al.* Stamp Transferred Suspended Graphene Mechanical Resonators for Radio Frequency Electrical Readout. *Nano Lett.* **12**, 198-202 (2012).

237 Adiga, V. P. *et al.* Simultaneous electrical and optical readout of graphene-coated high Q silicon nitride resonators. *Appl. Phys. Lett.* **103**, 143103, (2013).

238 Cagliani, A., Pini, V., Tamayo, J., Calleja, M. & Davis, Z. J. Ultrasensitive thermometer for atmospheric pressure operation based on a micromechanical resonator. *Sens. Actuator B-Chem.* **202**, 339-345 (2014).

239 Lachut, M. J. & Sader, J. E. Buckling of a cantilever plate uniformly loaded in its plane with applications to surface stress and thermal loads. *J. Appl. Phys.* **113,** 024501 (2013).

240 Mertens, J. *et al.* Effects of temperature and pressure on microcantilever resonance response. *Ultramicroscopy* **97**, 119-126 (2003).

241 Hsueh, C.-H. Modeling of elastic deformation of multilayers due to residual stresses and external bending. *J. Appl. Phys.* **91**, 9652-9656 (2002).

242 Lagowski, J., Gatos, H. C. & Sproles, E. S. Surface stress and the normal mode of vibration of thin crystals :GaAs. *Appl. Phys. Lett.* **26**, 493, (1975).

243 Gurtin, M. E., Markenscoff, X. & Thurston, R. N. Effect of surface stress on the natural frequency of thin crystals. *Appl. Phys. Lett.* **29**, 529, (1976).

244 Lachut, M. J. & Sader, J. E. Effect of surface stress on the stiffness of cantilever plates: Influence of cantilever geometry. *Appl. Phys. Lett.* **95,** 193505 (2009).

245 Mercatelli, R. *et al.* Quantitative measurement of scattering and extinction spectra of nanoparticles by darkfield microscopy. *Appl. Phys. Lett.* **99**, 131113, (2011).

246 Abazari, A. M., Safavi, S. M., Rezazadeh, G. & Villanueva, L. G. Modelling the Size Effects on the Mechanical Properties of Micro/Nano Structures. *Sensors* **15**, 28543-28562 (2015).

247 Castellanos-Gomez, A. *et al.* Single-Layer MoS2 Mechanical Resonators. *Adv. Mater.* **25**, 6719-6723 (2013).

248 Ruz, J., Tamayo, J., Pini, V., Kosaka, P. & Calleja, M. Physics of nanomechanical spectrometry of viruses. *Sci. Rep.* **4**, 6051 (2014).

249 Ndieyira, J. W. *et al.* Surface-stress sensors for rapid and ultrasensitive detection of active free drugs in human serum. *Nat. Nanotechnol.* **9**, 225-232, (2014).

250 Marder, M., Deegan, R. D. & Sharon, E. Crumpling, buckling, and cracking: elasticity of thin sheets. *Phys.Today* **60**, 33 (2007).

251 Li, B., Cao, Y.-P., Feng, X.-Q. & Gao, H. Mechanics of morphological instabilities and surface wrinkling in soft materials: a review. *Soft Matter* **8**, 5728-5745 (2012).

252 Starostin, E. & Van Der Heijden, G. The shape of a Möbius strip. *Nat. Mater.* **6**, 563-567 (2007).

253 Vliegenthart, G. & Gompper, G. Forced crumpling of self-avoiding elastic sheets. *Nat. Mater.* **5**, 216-221 (2006).

254 Landau, L. D. & Lifshitz, E. *Theory of Elasticity*, (Elsevier, 1986).

255 Haiss, W. Surface stress of clean and adsorbate-covered solids. *Rep. Prog. Phys.* **64**, 591 (2001).

256 Sader, J. E. Surface stress induced deflections of cantilever plates with applications to the atomic force microscope: Rectangular plates. *J. Appl. Phys.* **89**, 2911-2921 (2001).

257 Niklas, K. J. A mechanical perspective on foliage leaf form and function. *New Phytol.* **143**, 19-31 (1999).

258 Rolland-Lagan, A.-G., Remmler, L. & Girard-Bock, C. Quantifying shape changes and tissue deformation in leaf development. *Plant Physiol.* **165**, 496-505 (2014).

259 Tamayo, J., Ruz, J. J., Pini, V., Kosaka, P. & Calleja, M. Quantification of the surface stress in microcantilever biosensors: revisiting Stoney's equation. *Nanotechnology* **23**, 475702 (2012).

260 Penedo, M., Fernández-Martínez, I., Costa-Krämer, J. L., Luna, M. & Briones, F. Magnetostriction-driven cantilevers for dynamic atomic force microscopy. *Appl. Phys. Lett.* **95**, 143505, (2009).